



**Max-Planck-Institut für Festkörperforschung
Stuttgart**

First-Principles Calculations of LaMnO₃ Surface Reactivity

Yuri Mastrikov

Dissertation
an der
Universität Stuttgart

August 2008

**First-Principles Calculations
of LaMnO₃ Surface Reactivity**

Von der Fakultät Chemie der Universität Stuttgart
zur Erlangung der Würde
eines Doktors der Naturwissenschaften (Dr. rer. nat.)
genehmigte Abhandlung

Vorgelegt von

Yuri Mastrikov

aus Medweschjegorsk, Russland

Hauptberichter:

Prof. Dr. Joachim Maier

Mitberichter:

Prof. Dr. Hermann Stoll

Mitprüfer und Prüfungsvorsitzender:

Prof. Dr. Emil Roduner

Tag der mündlichen Prüfung:

08.04.2008

Max-Planck-Institut für Festkörperforschung, Stuttgart

Universität Stuttgart

2008

Contents

Zusammenfassung	2
1 Introduction	7
2 Theoretical Background	14
2.1 VASP Computational procedure.....	14
2.2 Exchange-correlation functionals	18
3 Computational Details	23
3.1 Treatment of the core electrons.....	23
3.2 Setting the k-point mesh	24
4 Perfect LaMnO₃ Crystal	25
4.1 Magnetic properties.....	26
4.2 Orthorhombic phase.....	29
4.2.1 Structure optimization	29
4.2.2 The electronic structure	33
4.3 Cubic Phase.....	36
5 Surface Calculations	37
5.1 The (001) surface	38
5.2 The (110) surface	48
6 Oxygen Adsorption on the LaMnO₃ (001) MnO₂-terminated Surface and Oxygen Vacancy	52
6.1 Oxygen adsorption	52
6.1.1 Atomic O adsorption	53
6.1.2 Molecular O adsorption.....	57
6.2 Oxygen vacancies in the bulk and on the the MnO ₂ -terminated surface	61
6.2.1 Surface vacancy.....	61
6.2.2 Bulk O vacancy	63
7 Conclusions	65
References	68
Acknowledgements	73
Curriculum Vitae	74
List of publications relevant to this study	75

Zusammenfassung

Das Hauptziel der vorliegenden Dissertation ist die Modellierung der elementaren *Prozesse* an der Kathode der Festoxidbrennstoffzelle - auf atomarem Niveau. Zu diesem Zweck wählten wir die Generalised Gradient Approximation (GGA)-Methode innerhalb der Dichte-Funktional-Theorie (DFT), wie sie im *VASP* Rechnercode implementiert ist. Als Modellkathodenmaterial wurde LaMnO_3 eingesetzt. Einer der Hauptgründe, diesen Code zu benutzen ist, sein sehr leistungsfähiger Strukturoptimierungsalgorithmus. Wie in dieser Arbeit gezeigt wird, liefert er trotz einiger Mängel der DFT Methode sehr vernünftige Struktur- und Energieparameter für eine derart stark korrelierte Materie wie LaMnO_3 . Wir berechneten die atomare und elektronische Struktur des perfekten LaMnO_3 sowie der reinen Oberflächen. Des Weiteren modellierten wir adsorbierten Sauerstoff auf der MnO_2 -terminierten Oberfläche sowie Sauerstoffleerstellen im Festkörper und auf der (001) Oberfläche. Zusammen mit den elektrostatischen Eigenschaften berechneten wir ebenfalls die Migrationsenergien für adsorbierten Sauerstoff und Sauerstoffleerstellen, die LaMnO_3 -Kohäsionsenergie und Oberflächenbildungsenergie. Die Elektronendichteverteilung wurde anhand der Elektronendifferenzabbildungen und den effektiven Atomladungen analysiert, die mit Hilfe von topologischen (Bader) Analysen berechnet wurden. Besondere Aufmerksamkeit wurde der Energetik und der Ladungsumverteilung bei der Adsorption von Sauerstoffatomen und molekülen an der LaMnO_3 (001) Oberfläche gewidmet.

Die Grundprinzipienmodellierung wurde an großen Superzellen (bis zu 270 Atomen) durchgeführt, die sehr zeitaufwendige Parallelkalkulationen an einem LINUX Computercluster (aufgebaut in unserer Abteilung) benötigten. Zu jedem Zeitpunkt der Studie verglichen wir die erhaltenen Ergebnisse mit experimentellen Daten (soweit erhältlich) und (anderen) theoretischen Berechnungen.

Kapitel I und II sind den Grundlagen der DFT Theorie sowie der Auswahl der Austauschkorrelationsfunktionale und Potentiale gewidmet. Des Weiteren wurde die Zuverlässigkeit der Rechenmethode überprüft. Eine Reihe von Berechnungen wurde an LaMnO_3 (*Volumen*) unter Gebrauch von Projector Augmented Wave (PAW) Perdew-Wang 91 und Perdew-Burke-Ernzerhof GGA Potentialen durchgeführt, sowohl für die orthorhombische als auch die kubische Phase. Die Standardabweichung (RMSD) der optimierten *Gitterkonstanten* in Bezug auf die experimentellen Daten ist nicht größer als 0.08 Å, solange nicht das „harte“ Sauerstoffpotential verwendet wird. Wird es verwendet, ist die Abweichung etwas größer (0.11-0.14 Å). Im Gegensatz zu den gerade erwähnten (PAW)

Potentialen, geben die Ultra-Soft Vanderbilt (US) Ceperley-Alder Pseudopotentiale die Gitterkonstanten weniger genau wieder (RMSD = 0.23-0.44 Å).

Im Kapitel III untersuchten wir beide LaMnO_3 -Phasen: die orthorhombische Niedrigtemperatur- (4 Formeleinheiten pro Zelle) und die kubische Hochtemperaturphase ($T > 750$ K). Wir analysierten sorgfältig die Abhängigkeit der berechneten *Kohäsionsenergie* und der Gitterparameter von der *magnetischen Anordnung* - ferromagnetische (FM), drei antiferromagnetische (A-, C-, GAF) und nicht-spinpolarisierte (NM) Konfiguration. FM entspricht dem vollständig ferromagnetischen Material, in welchem alle Spins des Mn parallel ausgerichtet sind. AAF bedeutet, dass die ferromagnetische Kupplung in der Basisfläche ab (xy) mit der Kupplung in die z -Richtung kombiniert ist (in der Pbnm Einstellung). In der CAF Zelle sind die Spins in der Basisfläche antiferromagnetisch gekoppelt und ferromagnetisch zwischen den Flächen (entlang der c -Achse) und in GAF sind alle Spins antiferromagnetisch zu dem jeweils nächsten Nachbaratom gekoppelt. Es stellte sich heraus, dass für beide Eigenschaften die Vernachlässigung der Spinpolarisation zu großen Abweichungen im Vergleich mit den experimentellen Daten führt. Wird eine experimentelle orthorhombische Geometrie verwendet, wird die AAF-Konfiguration zu der energetisch bevorzugten in Übereinstimmung mit experimentellen Ergebnissen. Eine weitere Optimierung der Struktur favorisiert jedoch den um 0.03 eV (0.1%) stabileren FM Zustand, was allerdings am Limit der Genauigkeit der Methode liegt.

Die berechnete *Kohäsionsenergie* von 31.0 eV liegt nahe des experimentellen Wertes von 30.3 eV. In der Tat beträgt die Differenz zwischen den Kohäsionsenergien der meist (FM) und der am wenigsten (GAF) bevorzugten magnetischen Konfiguration nur ungefähr 0.1 eV (0.3%), wobei für die nicht-spinpolarisierte Berechnung die Energie deutlich höher ist (~ 1 eV). Wie erwartet liegen für die LMO in der kubischen Phase die Kohäsionsenergien der entsprechenden magnetischen Zustände um etwa 1% höher als für die in der orthorhombischen Phase. Die berechneten effektiven Atomladungen (2.07 e (La), 1.67 e (Mn), -1.24 e (O)) weisen auf eine beträchtliche *Kovalenz* der Mn-O-Bindung hin. Unsere Berechnungen der *magnetischen Kopplungskonstanten* liefern Werte ähnlich den experimentellen Daten und reproduzieren ebenfalls die bekannte *Orbitalanordnung* des LaMnO_3 (abwechselnde C-Typ Besetzung der $3x^2-r^2$ - und $3y^2-r^2$ - Orbitale des nächstliegenden Mn-Ions in der Basisebene). Der größte Nachteil unserer Rechenmethode ist die Unterschätzung der Bandlücke, die für die DFT - Methode typisch ist.

Es gibt zwei unterschiedliche Arten von Verzerrungen in der *orthorhombischen* Struktur, die sie vom kubischen Perowskit LMO unterscheidet: die *Jahn-Teller- Verzerrung* der sechs

O-Ionen um die Mn-Ionen sowie die gegenseitige *Neigung* und *Verdrehung* der benachbarten MnO_6 -Oktaeder. In vielen Fällen, wenn die untersuchten Effekte mit Energien größer als einige Zehntel eV einhergehen, können die feinen magnetischen Eigenschaften und Verzerrungen der Struktur vernachlässigt werden. Speziell in solchen Fällen ist die spezifische magnetische Anordnung nicht mehr so wichtig wie die Bedeutung der Spinpolarisation selbst. Obwohl es möglich ist die Berechnungen auf Basis der kubischen Struktur durchzuführen (wie es für die reine Oberfläche geschehen ist), ist es besser, die Neigung und Rotation der Oktaeder beizubehalten, da diese Art der Verzerrung eine effizientere Raumauffüllung erleichtert. So kann beispielsweise ein Punktdefekt auf der Oberfläche einer aus kubischen Elementarzellen aufgebauten Schicht die komplette Rekonstruktion dieses Aufbaus auslösen, mit der Konsequenz, dass die Bildungsenergie des Defekts nahezu bedeutungslos werden kann.

In Kapitel IV werden zwei unterschiedlich orientierte reine *Oberflächen* von LaMnO_3 betrachtet: (001) und (110), beide sind polar. Da die ehemalige (LaO- oder MnO_2 -terminierte) Oberfläche eine formale Flächenladung von $\pm 1 e$ hat, ist ihre elektrostatische Stabilität durch eine Ladungsumverteilung innerhalb der Schicht gewährleistet. Um eine alternative, deutlich polarere (110) Oberfläche zu stabilisieren, die abwechselnd LaMnO- und O_2 -geladene Schichten ($\pm 4 e$) enthält, muss die Hälfte der Sauerstoffatome aus der O_2 -terminierten Schicht entfernt werden.

Die atomaren/elektronischen Eigenschaften der (001) Oberfläche zeigen eine schwache Abhängigkeit von der magnetischen Anordnung. Die *Oberflächenbildungsenergie* ist für 7-, 8-Ebenen Schichten bei $0.8 eV/a_0^2$ (a_0 ist die Gitterkonstante) abgesättigt – ähnlich wie in SrTiO_3 (001). Es wurde jedoch eine ausgeprägte Differenz zwischen den *Oberflächenenergien* orthorhombischer und kubischer Schichten beobachtet. Da die Spannung in der kubischen Struktur aufgrund der weniger effizienten Raumaussnutzung größer ist, weist die kubische Schicht eine höhere *Relaxationsenergie* auf. Aufgrund von Schichtannäherungstests wurden die symmetrische nichtstöchiometrische 7-Ebenen und die asymmetrische stöchiometrische 8-Ebenen Schichten für weitere, detailliertere Berechnungen ausgewählt. Auf der MnO_2 -terminierten Oberfläche der orthorhombischen Schicht sind die Mn-Ionen der letzten Ebene um 0.07 \AA über die nächste Sauerstoffebene verschoben, während die beiden O-Subebenen dieser Schicht einen Abstand von 0.17 \AA aufweisen. Obwohl in den kubischen Schichtebenen die Zerlegung anders ist, begrenzt die Mn-Subebene die Oberfläche auch in diesem Fall. Im Gegensatz zur MnO_2 -Endschicht sind im Falle der LaO-Endschicht die La-Ionen *unter* die Sauerstoffoberflächenebene verschoben.

Die Elektronendichteanalyse zeigte, dass die *Ladungsumverteilung* auf der Oberflächen- und der Suboberflächenebene hauptsächlich durch die spezifische (MnO_2 - oder LaO -) Termination bestimmt ist und nicht durch die *Stöchiometrie* der Schicht (7- oder 8-Ebenen). Eine typische Differenz zwischen den Ladungen der Oberflächenionen in stöchiometrischer und nichtstöchiometrischer Schicht liegt bei 0.05 eV . Diese Tatsache erlaubt uns die nichtstöchiometrische 7-Ebenen Schicht, die ein Nulldipolmoment entlang der $[001]$ Richtung senkrecht zur Oberfläche zeigt, für die Modellierung der Adsorptionsprozesse auf der (001) Oberfläche ohne defektinduzierte Ladungskompensation (z. B. Einführung von Leerstellen) einzusetzen.

Wird die (110) Oberfläche, wie oben beschrieben, durch Oberflächensauerstoffleerstellen stabilisiert, ergeben sich ähnliche Oberflächenenergien ($\sim 1 \text{ eV}/a_0^2$) wie für die (001) Oberfläche. Unsere Vorhersage zur *atomaren Oberflächenrekonstruktion* könnte durch LEED Experimente überprüft werden.

In Kapitel V wurden sowohl die molekulare als auch die *dissoziative Sauerstoffadsorption* und *-diffusion* auf der MnO_2 -terminierten Oberfläche im Detail modelliert. Die am meisten bevorzugte Adsorptionsstellen für *atomaren* Sauerstoff befinden sich oberhalb des Mn sowie neben den Oberflächensauerstoffatomen. Die Adsorptionsenergien betragen 4 bzw. 2.4 eV und die entsprechenden effektiven Ladungen der adsorbierten O-Atome $0.6 e$ und $0.5 e$. In beiden Fällen konnten wir *Chemisorption* beobachten (im Gegensatz zur schwachen physikalischen Adsorption von O_2 auf der SrTiO_3 -Oberfläche). Wir vermuten, dass das adsorbierte O-Atom entlang der (110) Richtung von einem Mn-Atom zum anderen mit einer vergleichsweise hohen Aktivierungsenergie ($> 1.6 \text{ eV}$) wandern kann.

Für *molekularen Sauerstoff* wurden zwei energetisch stabile Orientierungen oberhalb des Mn-Ions gefunden: eine mit einer um $\sim 60^\circ$ senkrecht zur Oberfläche geneigten Molekülbindung und eine weitere mit der Bindung parallel zur Oberfläche. Die jeweiligen Adsorptionsenergien betragen 1.1 und 0.9 eV . Für beide Konfigurationen wurde wiederum eine *starke Chemisorption* beobachtet. Des Weiteren gibt es eine stabile Konfiguration für ein horizontal ausgerichtetes Molekül mit einer Adsorptionsenergie von 0.3 eV – über dem Oberflächensauerstoffatom. Aufgrund dessen gehen wir davon aus, dass die adsorbierten O_2 -Moleküle auch als Ganzes über die (001) Oberfläche mit einer Aktivierungsenergie von $> 0.6 \text{ eV}$ wandern könnten.

Durch die starke Bindung zwischen dem Adsorbat und dem Adsorbent kann das *Eindringen* des adsorbierten Sauerstoffs in die Oberfläche der Kathode vorwiegend durch den Zusammenstoß des Sauerstoffs mit mobilen Oberflächensauerstoffleerstellen erfolgen.

Folglich wurden die Bildungs- und die Diffusionsenergien für die O-Leerstellen auf der Oberfläche sowie im Festkörper berechnet. Die geringere Bildungsenergie auf der Oberfläche (6.23 eV vs. 7.64 eV im Festkörper) sollte die *O-Leerstellensegregation* stimulieren und könnte zu *Raumladungseffekten* führen. Auf der Oberfläche sind zwei Paare der nächstliegenden Mn- und La-Ionen um ca. 0.2 Å von der Leerstelle abgerückt, wobei die zwei O-Ionen stärker in Richtung Leerstelle verschoben sind (0.32 Å). Im Festkörper betragen die atomaren Verschiebungen um die Leerstelle maximal 0.12 Å. Die *Leerstellendiffusionsenergie* ist auf der Oberfläche (0.67 eV) kleiner als im Festkörper (0.95 eV), wobei letzterer Wert typisch für die ABO₃-Perowskite ist. Die geringere Energie für die Oberfläche stimmt auch mit dem Trend unserer Berechnungen für die Sauerstoffleerstellen in SrTiO₃ überein. Demzufolge erwarten wir, dass die *Oberflächenmobilität* der *Sauerstoffleerstellen* viel höher ist als die der adsorbierten O-Atome und somit die Leerstellenwanderung entlang der Kathodenoberfläche den schnellen O-Transport zum Elektrolyten ermöglicht.

Als Ergebnis der Untersuchungen der SOFC-Kathode konnten wir demonstrieren, dass der Standard-DFT-GGA-Ansatz die Reproduzierung der grundlegenden Eigenschaften von LaMnO₃ erlaubt, zum Vorschlag neuer Experimente führt und neues Licht auf das Problem der Oberflächenaktivität wirft.

Von sehr großem Interesse sind weitere Untersuchungen in Bezug auf:

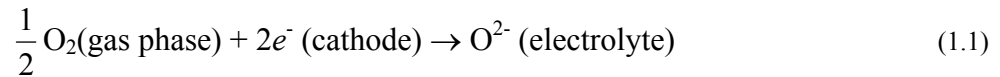
- LaO-terminierten Oberflächen,
- die Schwelle für den Sprung des adsorbierten O Atoms in die nächstliegende O-Leerstelle,
- Vorgänge an der Dreiphasengrenze,
- Sr-dotiertem LMO und LaCoO₃, (La,Sr)(Mn,Co)O₃, wie sie in herkömmlichen Brennstoffzellen eingesetzt werden
- Untersuchungen bei hohen Temperaturen, die für SOFC-Betriebsbedingungen typisch sind, z.B. Quantenmolekulardynamik.

Die kommende Version des *VASP*-Rechnercodes mit *Hybridaustauschkorrelationsfunktionalen* verspricht mehr Genauigkeit bei der Berechnung elektronischer Eigenschaften.

1 Introduction

Solid oxide fuel cells (SOFCs) are promising power generation devices due to their high electrical efficiency, multi-fuel capability, potential role in carbon sequestration, and possibilities for coupling with a gas turbine. In this type of fuel cells the electrolyte is a solid, nonporous metal oxide, usually Y₂O₃-stabilized ZrO₂, which at higher temperatures provides an efficient conduction of oxygen ions toward the anode (see Figure 1.1).

The anode is typically a Ni-ZrO₂ or Co-ZrO₂ cermet, and the cathode, Sr-doped LaMnO₃(LMO), hereafter called LSM. The main function of the cathode is to provide reaction sites for the electrochemical reduction of the oxidant (usually air or pure oxygen). Although various other cathodes have been studied, such as La(Pr)CoO₃, La_{1-x}Sr_xFe_{1-y}Co_yO_{3-δ} [1], LSM has been mostly investigated and is considered as the most appropriate cathode to be used with zirconia electrolyte fuel cells due to its electrical properties, catalytic activity thermal compatibility, and chemical stability [2]. Comparing the various processes, which occur under working conditions, the reaction at both electrodes is assumed to determine the cell performance [3]. At the cathode, that I will focus on in my thesis, two major pathways for the multi-step oxygen reduction reaction,



are expected [4]. In this regard detailed experimental studies of LMO cathode properties were performed in the department of Physical Chemistry of Max Planck Institute for Solid State Research [2, 5, 6].

The first path (**bulk path**) is sketched in Figure 1.2 (top). In this case, oxygen penetrates the surface and then “travels” through the LSM cathode and onwards into the electrolyte (through the contact surface between cathode element and electrolyte). Within the second path (**surface path**, Figure 1.2(bottom)) for the incorporation reaction oxygen also adsorbs on the cathode, but then diffuses along the surface of LSM grain to the electrolyte. Here, the oxygen is not completely ionized immediately, but instead firstly “travels” along the surface toward the *three-phase boundary* (TPB), where electrolyte, LSM cathode, and oxygen gas phase are in contact. The role of the TPB is to enable transfer into the electrolyte as well as to provide electrons. However, under operation conditions, especially taking into account realistic LSM surfaces (*e.g.* nanosize, presence of non-equilibrium, defects, etc.), other reaction mechanisms are possible. The proposed study focuses on LMO surface and its interaction with oxygen.

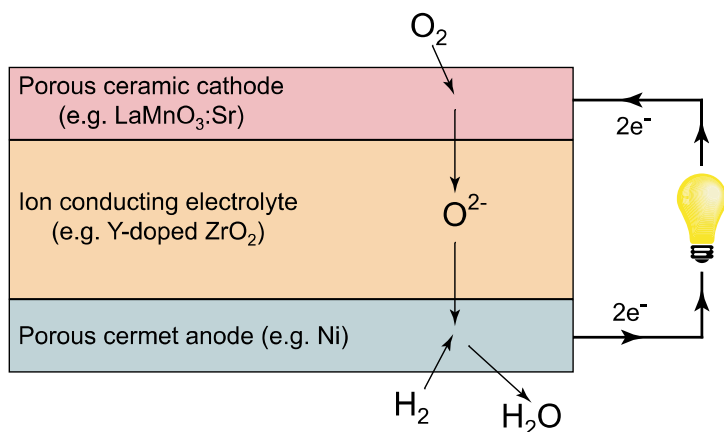


Figure 1.1. Operation principle of SOFC.

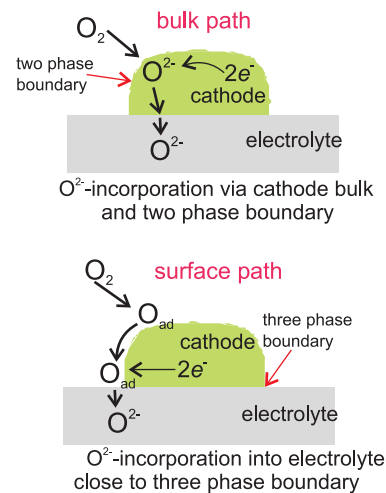


Figure 1.2. Some of the possible reaction paths of the oxygen reduction, and incorporation reaction. From Ref. [4].

In the SOFC, the process of oxygen incorporation into the cathode may occur with a significantly slower specific rate than the ion transport in the electrolyte and the process of water formation at the anode and thus may determine the total rate of the electrochemical process [4]. Therefore, to fabricate a more efficient SOFC, possible cathode materials and structures of the cathode/electrolyte interface have to be thoroughly investigated, improved, and optimized. Although there are several studies of the oxygen reduction kinetics and the nature of active sites [7-9], significant uncertainty concerning the reaction mechanism remains. This is partly because the active sites for oxygen reduction have not been fully identified yet. A combination of experimental methods (e.g. impedance spectroscopy) and atomistic computer simulations should be able to shed further light on the reaction steps and the mechanisms proceeding at cathodes during fuel cell operation. In addition to existing distinctive knowledge obtained purely from experiment [10-18], comprehensive *theoretical* investigations of the reaction steps taking place on the surface of the LSM electrode at atomistic level are of key importance for improving cathode parameters and optimizing the SOFC performance.

Previous theoretical studies of ionic migration processes in LSM and LaMnO₃, the parent compound of LSM, so far are very preliminary and generally based on semi-empirical, shell model calculations [19-21]. The *shell model* is able to give semi-quantitative information on the migration energies (which are found to be much smaller for oxygen than for metal cations), but not on the charge state of migrating species and mechanisms of O₂ dissociation on perovskite surfaces. Almost nothing is known on the migration energies of oxygen atoms on oxide surfaces.

The first careful DFT-GGA modelling of oxygen adsorption on a simple highly ionic oxide viz. on MgO (001) surface, was performed 10 years ago [22]. The adsorbate energetics on a flat surface with structure optimization, charge and spin density analysis, as well as *density of states* (DOS) and electronic density distribution were calculated. The main configurations studied refer to the O atom position above surface Mg ion and O ion (Figure 1.3).

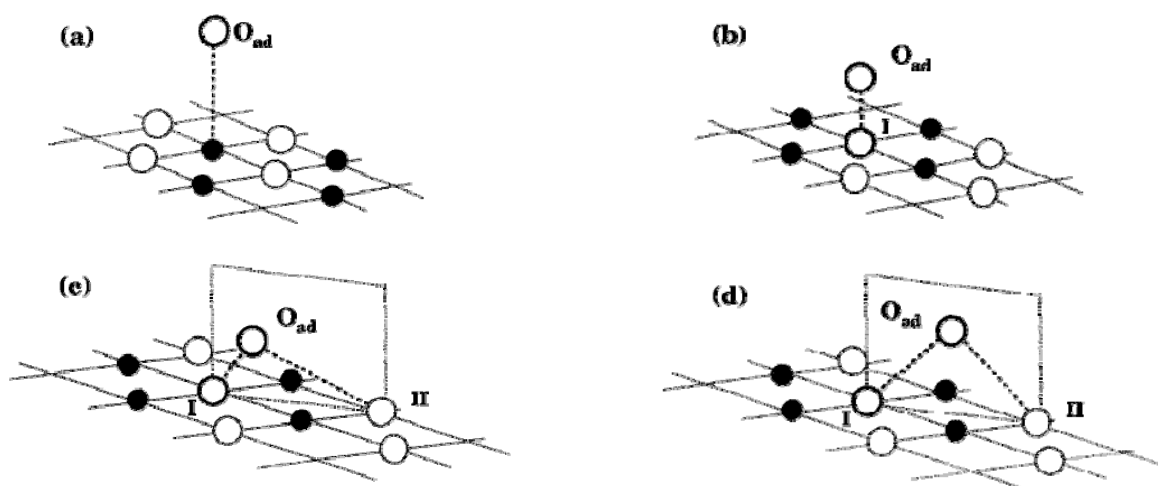


Figure 1.3. Geometries used in the calculations of oxygen adsorption on the flat MgO (001) terrace. O_{ad} is the oxygen adatom, Mg and O atoms are indicated by grey and white circles, respectively. Panels show the oxygen atom positioned (a) above a surface Mg ion, (b) above a surface O ion, (c) in the plane perpendicular to the surface and passing through the two oxygen ions I and II, and (d) the same as (c) but with the O atom positioned above the mid-point between two nearest lattice oxygens. Taken from Ref. [22].

Table 1.1. Calculated energies (in eV) and equilibrium distances (in Å) for atomic oxygen adsorption on the flat MgO (001) surface calculated using two- and four-layer slabs at the four sites shown in Figure 1.3; results were obtained with the GGA except for those in parentheses which were obtained with the LDA [23]. Taken from Ref [22].

Site	Spin	Layers	E_{ad}	Equilibrium distance		
				O_{ad} -Mg	O_{ad} - O_I	O_{ad} - O_{II}
a	0	2	-0.28	1.96		
		2	(0.08)	(1.92)		
		4	-0.32	1.95		
	1	2	0.85	2.01		
		4	0.84	2.00		
b	0	2	1.72		1.55	
		2	(2.41)		(1.52)	
		4	1.74		1.55	
	1	2	0.64		2.16	
		4	0.64		2.15	
c	0	2	2.03		1.55	2.72
		4	2.04		1.55	2.75
d	0	2	0.96		2.24	2.24
		4	1.05		2.27	2.27
		4	1.43		2.26	2.26
	1	2	1.43		2.25	2.25
		4	1.43		2.26	2.26

The average distance between periodically distributed O atoms was about 6 Å, sufficient to neglect adsorbate-adsorbate interaction. The adsorbed O_{ad} atom was calculated in both possible spin states: singlet ($S_z=0$) and triplet ($S_z=1$). It was found (Table 1.1) that MgO slabs containing even two planes give already reasonable results, due to a small surface relaxation and highly ionic nature of a material.

The calculations show that O adsorption atop Mg ions is much stronger in the triplet state than in the singlet. The adsorption energy of 0.85 eV corresponds to the equilibrium distance of 2 Å, close to the Mg-O distance in MgO crystal (2.1 Å). Unlike Mg ion, O adsorption is more stable in the triplet state (like in a free O atom). The relevant binding energy of 1.74 eV is twice as large as for the Mg ion. The bond length is also much shorter, 1.55 Å. This points towards formation of the O_2^{2-} peroxide ion. In this case, two electrons are shared between the surface O^{2-} ion and the adsorbed O atom. However, the energetically most favourable configuration is the antisymmetrically tilted one along the (110) (Figure 1.3c) with a binding energy of 2.03 eV, typical for chemisorption. Unlike O atoms, *molecular* oxygen O_2 undergoes only weak physisorption with an adsorption energy about 0.1 eV.

Along with O adsorption on ion surfaces, a series of calculations was performed for O adsorption on reduced surfaces rutile TiO_2 (110) and SnO_2 (110) [24-28]. In the rutile structure the (110) surface is the most stable one. Most of the calculations were performed using the DFT-GGA method and the periodic supercell model.

First- principles DFT calculations for O adsorption on $RuO_2(110)$ surface were performed by M. Scheffler et. al. ([29] and references therein).

They studied carefully several possible adsorption sites on the surface and O atom diffusion along the surface. These static (zero K) calculations were used to develop *ab initio* thermodynamics via calculation of the Gibbs free energy for slabs with adsorbed O atoms. It was demonstrated that the traditionally assumed stoichiometric termination of RuO_2 (110) is energetically favorable only at low chemical potentials, i.e. low gas pressure and/or high temperature. Contrary, at realistic oxygen pressure, the surface is predicted to contain additional terminal O atoms.

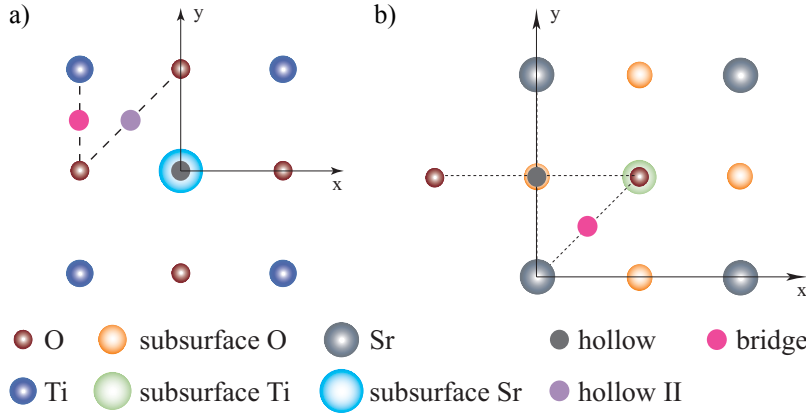


Figure 1.4. Top views of the possible positions for oxygen adsorption on fragments of both (a) TiO_2 - and (b) SrO -terminated (001) substrate. Taken from Ref. [30].

Recently [30], a first principles study was performed for O adsorption on SrTiO_3 (STO) isostructural to LMO. Unlike most of previous studies based on the *VASP 4.6.19* code, the *CRYSTAL 2003* computer code was used here, with the B3PW

hybrid exchange-correlation functional and the basis set of atomic orbitals.

Table 1.2. Calculated energies (in eV), equilibrium distances (in \AA), and Mulliken charges in e for the energetically favorable configurations of atomic oxygen adsorption at $\text{SrTiO}_3(001)$ substrate as shown in Figure 1.4. Mulliken charges at the clean surface layer (in e): SrO -termination – Sr 1.84, O -1.52; TiO_2 -termination – Ti 2.31, O -1.32. Seventh column shows the average distance between the surface and O_{ads} along the z -axis. Taken from Ref. [30].

Site	Spin	$E_{(\text{at})\text{ads}}$	E_{ads}	Distances, O_{ads} -			Charges		
				O_{surf}	$\text{Ti}(\text{Sr})_{\text{surf}}$	surface	O_{ads}	O_{surf}	$\text{Ti}(\text{Sr})_{\text{surf}}$
TiO₂-terminated SrTiO₃(001)									
O	0	1.76	-0.93	1.46	2.76	1.14	-0.62	-0.77	2.29
bridge	0	2.03	-0.66	1.47	1.91	1.34	-0.52*	-0.79	2.28
hollow II	1	0.93	-1.75	2.24	2	1.71	-0.29	-1.16	2.29
SrO-terminated SrTiO₃(001)									
O	0	1.54	-1.14	1.47	3.24	1.58	-0.71	-0.9	1.86
bridge	0	2.43	-0.26	1.50	2.45	1.19	-0.84	-0.88	1.85
hollow	1	1.08	-1.26	2.48	2.53	1.55	-0.52	-1.32	1.86

*electron population of $\text{O}_{\text{ads}}\text{-Ti}$ bond in this case is 0.13 e .

Table 1.2 shows three energetically favorable atomic adsorption configurations on both substrate terminations: (i) atop O_{surf} ions and (ii) bridge positions (if O_{ads} is considered in the closed-shells singlet state), as well as (iii) hollow sites (if O_{ads} is in the triplet state). The most favored optimized configurations have been found to be above bridge positions: on both substrate terminations the adatom is shifted substantially towards the nearest surface oxygen ion (Figure 1.5). Moreover, both configurations for the oxygen adsorption atop O_{surf} ions could be considered as particular cases of the corresponding bridge configurations since horizontal coordinates of O_{ads} during geometry optimization of (i) have been fixed. Mulliken analysis presented in Table 1.2 shows that 0.6-0.8 e are transferred to O_{ads} from the surface oxygen ion in (i) and (ii) configurations (note that bond population of O_{ads} localized at a bridge site on the TiO_2 -terminated substrate with the nearest Ti ion is 0.13 e), and 0.3-0.5 e in

hollow configurations. The bond lengths and values of electronic charge transfers (Table 1.2) as well as the distributions of electron density isolines (Figure 1.5) clearly indicate the formation of pseudomolecular species ($O_{\text{ads}}-O_{\text{surf}}$) in both (i) and (ii) configurations. In the bulk and at the (001) surface of SrTiO_3 O sites are occupied by oxygen ions (due to a partial covalency of O-Ti bonds, their effective charge is $-1.55 e$ [31]) whereas the oxygen adatom approaching to the surface is neutral. Thus, O_{ads} can be described as O^{2-} ion occupied by two holes, which will tend to delocalize by jumping to other ions and give rise to binding. On the more ionic SrO-terminated substrate, O_{ads} atom is bound by 0.4 eV more strongly than on the more covalent substrate with TiO_2 termination (in the case of the energetically favorable bridge configurations).

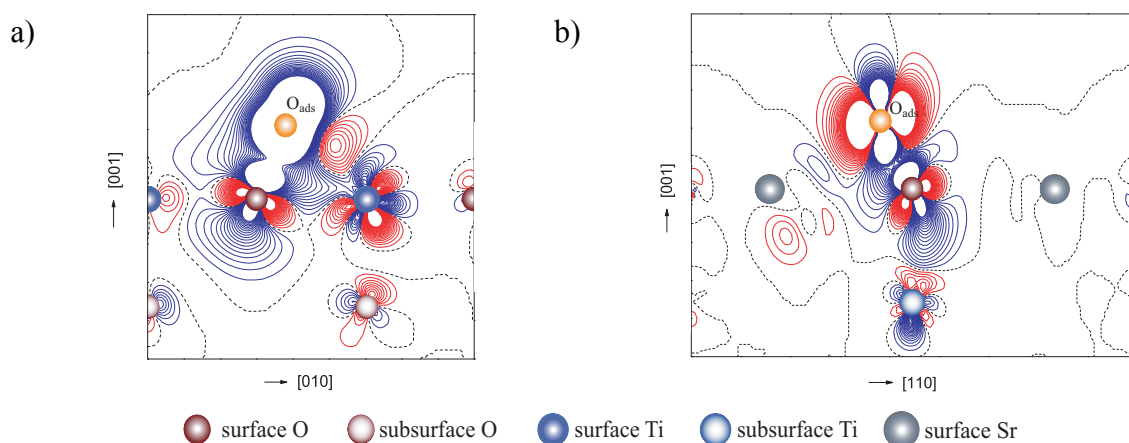


Figure 1.5. 2D differential electron density maps for O_{ads} over bridge site on (a) TiO_2 -terminated and (b) SrO-terminated $\text{SrTiO}_3(001)$ surfaces. At the electron density map, solid (red), dash (blue) and dash-dot (black) lines describe positive, negative and zero values of the induced electron density, respectively.

These calculations show considerable differences between O adsorption on the ionic MgO surface and the partly covalent SrTiO_3 (STO). Indeed, in STO the most favourable position is the bridge (centre of the Ti-O distance) on both termination for the singlet atom and hollow positions in the triplet state. We will compare in Section 6 these findings with our results for the LMO.

In addition, only two first-principles studies on perfect $\text{LaMnO}_3(001)$ [35] and $\text{LaMnO}_3(110)$ [36] surfaces had been performed at the moment when the present investigation was started. In these studies the surface cleavage energies of $\text{LaMnO}_3(001)$ surfaces have been found to be smaller than those of $\text{LaMnO}_3(110)$ surfaces [37]. This indicates that the $\text{LaMnO}_3(001)$ surface possibly plays a major role in the oxygen-related processes in fuel cells and other applications. Therefore in the proposed study I will compare properties of the LMO (001) and (110) surfaces. When the Thesis was close to completion, a paper [37] was

published in which DFT calculations were performed for oxygen adsorption on the LMO(110) surface. This paper will be discussed in Chapter 6. We only comment here that due to 100% coverage of the surface by oxygen a strange result was obtained: O₂ molecules are predicted to easily dissociate, giving O²⁻ ions without any energy barrier, what contradicts experimental data [38, 39].

2 Theoretical Background

2.1 VASP Computational procedure

In this Thesis all calculations were performed using the *VASP* Plane-wave code based on the DFT formalism. The computational procedure of the *VASP* code [32, 33] includes an iterative solution of the Kohn–Sham equations based on residuum-minimization and optimized charge-density mixing routines [34]. This includes the calculations of the Hellmann–Feynman forces acting on the atoms and of the stresses on the unit cell [33]. The total energy is optimized with respect to the positions of the atoms within unit cell or supercell. The Kohn-Sham method employing a plane-wave basis set and the *pseudopotential* (PP) approximation are currently among the most successful techniques in computational material science [40]. However, its formal simplicity demands a price: first-row elements, transition metals, and rare-earth elements were found to be computationally too time-consuming to be treated with standard norm-conserving PPs [41]. Various attempts were made to generate softer PPs: one of the most advanced approaches is the concept of *ultrasoft* PPs (US-PP) introduced by Vanderbilt [42]. But its success is partly hampered by the difficult construction of the PPs, *i.e.*, too many parameters (several cutoff-radii) must be chosen and therefore extensive tests are required to obtain an accurate and highly transferable US-PP. Further development of this concept has been made by Blöchl [43] by combining ideas from pseudopotential and Linearized Augmented-Plane-Wave (LAPW) methods in a framework, called the Projector Augmented-Wave Method (PAW). Recently, the formalism of PAW method has been successfully implemented into the *VASP* code [32, 44], which allows users to combine it with the earlier implemented US-PP approach.

The main idea of the PAW method is to transform the physically relevant full all-electron (AE) Kohn-Sham wave functions Ψ_n into computationally convenient pseudo-wave soft (PS) variational functions $\tilde{\Psi}_n$ [45]. The AE function may be derived from the PS function by means of a linear transformation:

$$|\Psi_n\rangle = |\tilde{\Psi}_n\rangle + \sum_i (|\varphi_i\rangle - |\tilde{\varphi}_i\rangle) \langle \tilde{p}_i | \tilde{\Psi}_n \rangle, \quad (2.1)$$

where the AE partial waves φ_i are obtained for a reference atom whereas the PS partial waves $\tilde{\varphi}_i$ are equivalent to the AE partial waves outside a core radius r_c^l and match continuously the $\tilde{\varphi}_i$ inside the core radius (the augmentation region, similar to the linearised muffin-tin LMTO formalism); the index i denote the atomic site \mathbf{R}_i , the angular momentum numbers $M = l, m$, and an additional index k referring to the one-electron reference energy ε_{kl} . The core radius is

usually chosen approximately around half the nearest-neighbour distance [44]. The projector functions \tilde{p}_i are dual to the PS partial waves:

$$\langle \tilde{p}_i | \tilde{\varphi}_j \rangle = \delta_{ij}. \quad (2.2)$$

In the PAW method, the all-electron charge density is given by [42]:

$$n(\mathbf{r}) = \tilde{n}(\mathbf{r}) + n^1(\mathbf{r}) - \tilde{n}^1(\mathbf{r}), \quad (2.3)$$

where $\tilde{n}(\mathbf{r})$ is the soft pseudo-charge-density calculated directly from the pseudo-wave-functions on a plane-wave grid *via* the occupations f_n of the states n :

$$\tilde{n}(\mathbf{r}) = \sum_n f_n \langle \tilde{\Psi}_n | \mathbf{r} \rangle \langle \mathbf{r} | \tilde{\Psi}_n \rangle. \quad (2.4)$$

The onsite charge densities n^1 and \tilde{n}^1 are treated on a radial support grid, that extends up to r_{rad} around each ion. They are defined as:

$$n^1(\mathbf{r}) = \sum_n \rho_{ij} \langle \varphi_i | \mathbf{r} \rangle \langle \mathbf{r} | \varphi_j \rangle, \quad (2.5)$$

$$\tilde{n}^1(\mathbf{r}) = \sum_n \rho_{ij} \langle \tilde{\varphi}_i | \mathbf{r} \rangle \langle \mathbf{r} | \tilde{\varphi}_j \rangle, \quad (2.6)$$

where ρ_{ij} are the occupancies of each augmentation channel (i, j) and are calculated from the pseudo-wave-functions applying the projector functions:

$$\rho_{ij} = \sum_n f_n \langle \tilde{\Psi}_n | \tilde{p}_i \rangle \langle \tilde{p}_j | \tilde{\Psi}_n \rangle. \quad (2.7)$$

The total charge density n_T is also decomposed into three terms [44], analogously to $n(\mathbf{r})$ in Eq. (2.3):

$$n_T = n + n_{Zc} = \tilde{n}_T + n_T^1 - \tilde{n}_T^1 = (\tilde{n} + \hat{n} + \tilde{n}_{Zc}) + (n^1 + n_{Zc}) - (\tilde{n}^1 + \hat{n} + \tilde{n}_{Zc}), \quad (2.8)$$

where n_{Zc} is the point charge density of the nuclei n_Z plus the frozen core AE charge density n_c , \hat{n} is a compensation charge which is added to the soft charge densities $(\tilde{n} + \tilde{n}_{Zc})$ and $(\tilde{n}^1 + \tilde{n}_{Zc}^1)$ in order to reproduce the correct multipole moments of the AE charge density $(n^1 + n_{Zc})$ that is located in each augmentation region. Because n_{Zc} and \tilde{n}_{Zc} have exactly the same monopole ($-Z_{\text{ion}}$) and vanishing multipoles, the compensation charge \hat{n} must be chosen such that $(\tilde{n}^1 + \hat{n})$ has the same moments as the AE valence charge density n^1 within each sphere [44]. For this purpose, compensation functions $g_l(|\mathbf{r}-\mathbf{R}|)$ are constructed for which the moment l is equal 1.

To obtain the Hamilton operator for the modified PAW total energy functional, the total energy must be varied with respect to the pseudo-density operator $\rho = \sum_n f_n |\tilde{\Psi}_n\rangle\langle\tilde{\Psi}_n|$ [44]:

$$H[\rho, \{\mathbf{R}\}] = \frac{dE}{d\rho} = \frac{d\tilde{E}}{d\rho} + \frac{dE^1}{d\rho} - \frac{d\tilde{E}^1}{d\rho} = -\frac{1}{2}\Delta + \tilde{v}_{\text{eff}} + \sum_{(i,j)} |\tilde{p}_i\rangle \left(\frac{\partial \tilde{E}}{\partial \rho_{ij}} + \frac{\partial E^1}{\partial \rho_{ij}} - \frac{\partial \tilde{E}^1}{\partial \rho_{ij}} \right) \langle \tilde{p}_j |, \quad (2.9)$$

where the first two terms (kinetic-energy operator $-\frac{1}{2}\Delta$ and effective one-electron potential \tilde{v}_{eff}) are presented in any Kohn-Sham Hamiltonian, as written in Eq.(2.10):

$$\hat{H}^{KS} = \hat{T}(\mathbf{r}; \mathbf{k}) + \hat{V}(\mathbf{r}; \mathbf{k}) + \hat{J}[\rho(\mathbf{r}); \mathbf{k}] + \hat{v}_{xc}[\rho(\mathbf{r}); \mathbf{k}] \quad (2.10)$$

potential \tilde{v}_{eff} includes both Hartree and exchange-correlation parts:

$$\tilde{v}_{eff} = v_H[\tilde{n} + \hat{n} + \tilde{n}_{Zc}] + v_{xc}[\tilde{n} + \hat{n} + \tilde{n}_c]. \quad (2.11)$$

The last terms of Hamiltonian in Eq. (2.9) are expressed via $-\frac{1}{2}\Delta$, \tilde{v}_{eff} and $\hat{Q}_{ij}^M(\mathbf{r})$ the operator of the charge density differences between the partial waves $Q_{ij}(\mathbf{r}) = \varphi_i^*(\mathbf{r})\varphi_j(\mathbf{r}) - \tilde{\varphi}_i^*(\mathbf{r})\tilde{\varphi}_j(\mathbf{r})$ and their moments q_{ij}^M :

$$q_{ij}^M = \int_{\Omega_r} Q_{ij}(\mathbf{r}) |\mathbf{r} - \mathbf{R}|^l Y_M^*(\overline{\mathbf{r} - \mathbf{R}}) d\mathbf{r}, \quad (2.12)$$

$$\hat{Q}_{ij}^M(\mathbf{r}) = q_{ij}^M g_l(|\mathbf{r} - \mathbf{R}|) Y_M^*(\overline{\mathbf{r} - \mathbf{R}}), \quad (2.13)$$

where \int_{Ω_r} stands for the integration over the radial support grid, M is short for (l, m) quantum numbers whereas Y_M denotes the angular part of wave function. Thus, last terms of PAW Hamiltonian are [44]:

$$\frac{\partial \tilde{E}}{\partial \rho_{ij}} = \sum_M \int \tilde{v}_{eff}(\mathbf{r}) \hat{Q}_{ij}^M(\mathbf{r}) d\mathbf{r} \quad (2.14)$$

$$\frac{\partial E^1}{\partial \rho_{ij}} = \left\langle \varphi_i \left| -\frac{1}{2}\Delta + v_H[n^1 + n_{Zc}] + v_{xc}[n^1 + n_c] \right| \varphi_j \right\rangle \quad (2.15)$$

$$\frac{\partial \tilde{E}^1}{\partial \rho_{ij}} = \left\langle \tilde{\varphi}_i \left| -\frac{1}{2}\Delta + \tilde{v}_{eff} \right| \tilde{\varphi}_j \right\rangle + \int_{\Omega_r} \tilde{v}_{eff}(\mathbf{r}) \hat{Q}_{ij}^M(\mathbf{r}) d\mathbf{r} \quad (2.16)$$

To define the PAW data set, the following quantities are required: (i) the AE and PS partial waves φ_i and $\tilde{\varphi}_i$; (ii) the projector functions \tilde{p}_i ; (iii) the core-charge density n_c , the pseudised core-charge density \tilde{n}_{Zc} and the partial electronic core-charge density \tilde{n}_c ; (iv) the compensation functions $g_l(|\mathbf{r} - \mathbf{R}|)$ [32, 44].

In general, the computational scheme of the code (Figure 2.1) consists of two loops - an outer and an inner, in which the charge density and wavefunctions are optimized, respectively.

The advantage of *VASP* plane wave calculations [32] is that the complete optimization of lattice relaxation upon vacancy creation, even for large supercells, can be performed much faster than for *CRYSTAL* calculations based on the localized basis sets [47]. Geometry optimizations have been carried out with an accuracy 10^{-3} eV in the total energy.

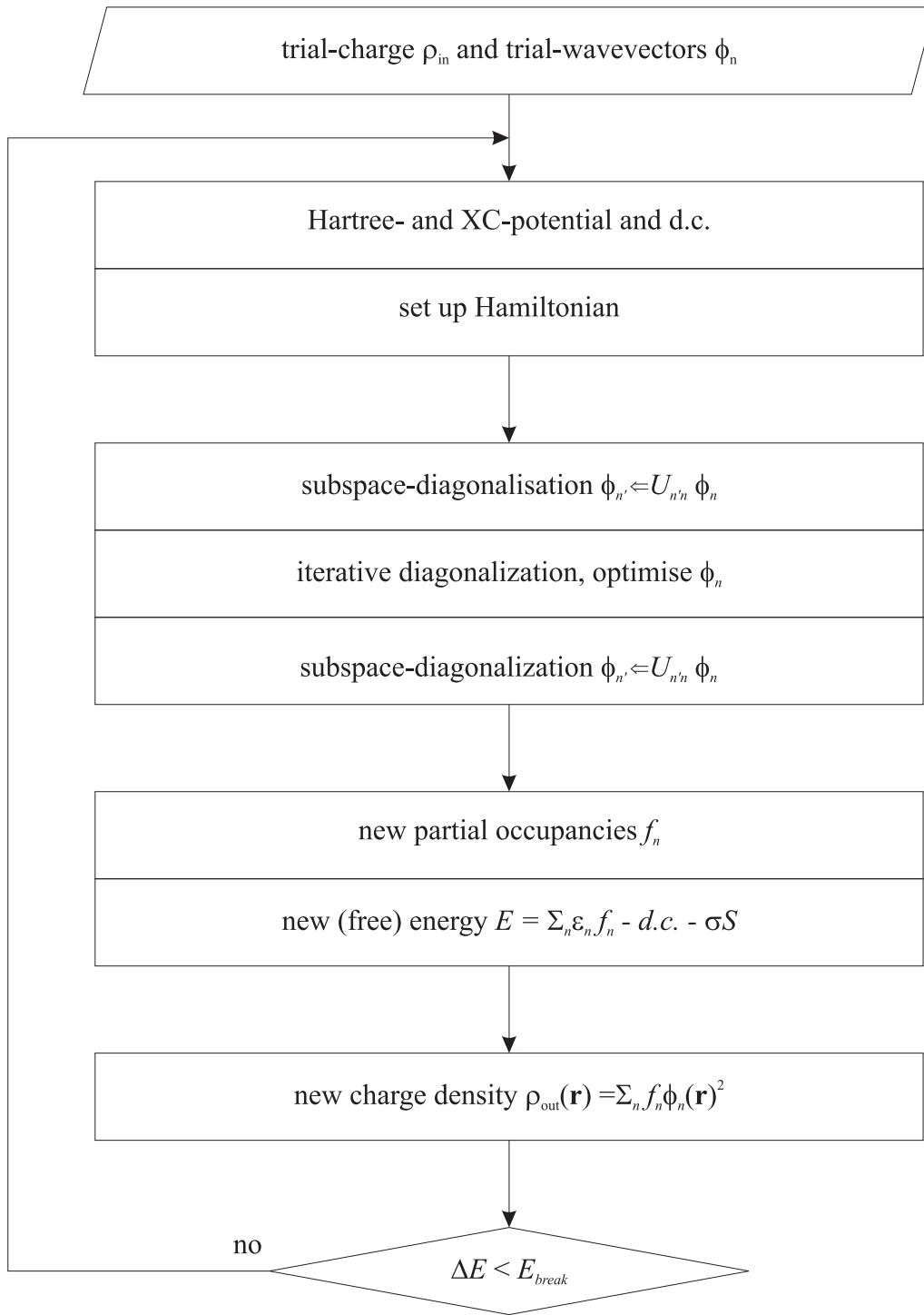


Figure 2.1. Calculation of Kohn-Sham ground state (*d.c.* stays for double counting terms).

2.2 Exchange-correlation functionals

One of the main problems in the DFT calculations is a proper choice of the *exchange-correlation functional* in the Kohn-Sham equation. This topic is discussed in the literature in detail [48, 49], and we will summarise here, following [48], several being points important for the present study.

In their classical paper [50], Kohn and Sham pointed out that solids can be considered as close to the limit of the *homogeneous electron gas*. In that limit, it is known that the effects of exchange and correlation are local in character, and they proposed making a *local density approximation* (LDA) (or more generally, a local spin density approximation (LSDA)), in which the exchange-correlation energy is simply an integral over the entire space with the exchange-correlation energy density at each point being assumed to be the same as in a homogeneous electron gas with that density,

$$\begin{aligned} E_{xc}^{LSDA}[n^\uparrow, n^\downarrow] &= \int d^3r n(\mathbf{r}) \epsilon_{xc}^{\text{hom}}(n^\uparrow(\mathbf{r}), n^\downarrow(\mathbf{r})) = \\ &= \int d^3r n(\mathbf{r}) [\epsilon_x^{\text{hom}}(n^\uparrow(\mathbf{r}), n^\downarrow(\mathbf{r})) + \epsilon_c^{\text{hom}}(n^\uparrow(\mathbf{r}), n^\downarrow(\mathbf{r}))]. \end{aligned} \quad (2.17)$$

(Here the axis of quantization of the spin is assumed to be the same at all points in space.) The LSDA can be formulated in terms of either two *spin densities* $n^\uparrow(\mathbf{r})$ and $n^\downarrow(\mathbf{r})$, or the total density $n(\mathbf{r})$ and the fractional spin polarization $\zeta(\mathbf{r})$,

$$\zeta(\mathbf{r}) = \frac{n^\uparrow(\mathbf{r}) - n^\downarrow(\mathbf{r})}{n(\mathbf{r})}. \quad (2.18)$$

The LSDA is the most general local approximation. For unpolarized systems the LDA is found simply by setting $n^\uparrow(\mathbf{r}) = n^\downarrow(\mathbf{r}) = n(\mathbf{r})/2$. In the spin-polarized calculations Kohn-Sham equations are solved independently for electrons with different spin orientation.

Once one has made the local *ansatz* of the L(S)DA, then all the rest follows. Since the functional $E_{xc}[n^\uparrow, n^\downarrow]$ is universal, it follows that it is exactly the same as for the homogeneous gas. The only information needed is the exchange-correlation energy of the homogeneous gas as a function of density; the exchange energy of the homogeneous gas is given by a simple analytic form and the correlation energy has been calculated to great accuracy with Monte Carlo methods [51]. In this study, we used E_{xc} suggested by Ceperley and Alder. As long as there are no further approximation in the calculations, the results of LDA and LSDA calculations can be considered as tests of the local approximation itself; the local

approximation lives or dies depending upon how the calculations agree with experiment (or with many-body calculations that can be considered essentially exact).

The rationale for the local approximation is that for the densities typical of those found in solids, the range of the effects of exchange and correlation is rather short, as discussed for the “exchange-correlation hole”. However, this is not justified by a formal expansion in some small parameter, and one must test the extent to which it works by actual applications. One expects it will be best for solids close to homogeneous gas (like a nearly-free-electron metal) and worst for very inhomogeneous cases like atoms where the density must go continuously to zero outside the atom.

Among the most obvious flaws is the spurious *self-interaction term*. In the Hartree-Fock approximation the unphysical self-term in the Hartree interaction is exactly cancelled by the non-local exchange interaction. However, in the local approximation to exchange, the cancellation is only approximate and there remain spurious self-interaction terms that are negligible in the homogeneous gas but large in confined systems such as atoms. Nevertheless, even in very inhomogeneous cases the LSDA works remarkably well.

The degree to which the LSDA is successful has made it useful in its own right, and has stimulated ideas for constructing improved functionals (such as the GGAs).

The success of the LSDA has led to the development of various *generalised-gradient approximations* (GGAs) with a marked improvement over LSDA for many cases. Widely used GGAs can now provide the accuracy required for density functional theory to be widely adopted by the chemistry community. Here we briefly describe some of the physical ideas that are the foundation for construction of GGAs.

The first step beyond the local approximation is a functional of the magnitude of the gradient of the density $|\nabla n^\sigma|$ as well as the value n at each point. Such a “gradient expansion approximation” (GEA) was suggested in the original paper of Kohn and Sham, and carried out by Herman et. al. [52]. The low-order expansion of the exchange and correlation energies is known [53]; however, the GGA does not lead to consistent improvement over the LSDA. The basic problem is that gradients in real materials are so large that the expansion breaks down.

The term *generalised-gradient expansion* denotes a variety of ways proposed for functions that modify the behaviour at large gradients in such a way as to preserve desired properties. It is convenient to define the functional as a generalised form of Eq. (2.17),

$$\begin{aligned} E_{xc}^{\text{GGA}}[n^\uparrow, n^\downarrow] &= \int d^3r n(\mathbf{r}) \epsilon_{xc}(n^\uparrow, n^\downarrow, |\nabla n^\uparrow|, |\nabla n^\downarrow|, \dots) \\ &\equiv \int d^3r n(\mathbf{r}) \epsilon_x^{\text{hom}}(n) F_{xc}(n^\uparrow, n^\downarrow, |\nabla n^\uparrow|, |\nabla n^\downarrow|, \dots), \end{aligned} \quad (2.19)$$

where F_{xc} is dimensionless and $\epsilon_x^{\text{hom}}(n)$ is the exchange energy of the unpolarized gas.

For exchange, it is straightforward to show that there is a “spin-scaling relation”,

$$E_x[n^\uparrow, n^\downarrow] = \frac{1}{2}[E_x[2n^\uparrow] + E_x[2n^\downarrow]], \quad (2.20)$$

where $E_x[n]$ is the exchange energy for an unpolarized system of density $n(\mathbf{r})$. Thus for exchange we need to consider only the spin-unpolarized $F_x(n, |\nabla n|)$. It is natural to work in terms of dimensionless reduced density gradients of m th order that can be defined by

$$s_m \equiv \frac{|\nabla^m n|}{(2k_F)^m n} = \frac{|\nabla^m n|}{2^m (3\pi^2)^{m/3} (n)^{(1+m/3)}}. \quad (2.21)$$

Since $k_F = 3(2\pi/3)^{1/3} r_s^{-1}$, s_m is proportional to the m th-order fractional variation in density normalized to the average distance between electrons r_s . The explicit expression for the first gradient can be written

$$s_1 \equiv s = \frac{|\nabla n|}{(2k_F)n} = \frac{|\nabla r_s|}{(2(2\pi/3)^{1/3} r_s)}. \quad (2.22)$$

The lowest order terms in the expansion of F_x have been calculated analytically [53, 54]

$$F_x = 1 + \frac{10}{81} s_1^2 + \frac{146}{2025} s_2^2 + \dots \quad (2.23)$$

Numerous forms of $F_x(n, s)$, where $s = s_1$, have been proposed; including Becke (B88) [55], Perdew and Wang (PW91) [56], and Perdew, Burke, and Ernzerhof (PBE) [57] used in this study.

The main problem with the Kohn-Sham approach is that no systematic way has been developed to improve the functionals for exchange and correlation. The problems are most severe in materials in which the electrons tend to be localized and strongly interacting, such as transition metal oxides or rare earth elements and their compounds. These systems exhibit phenomena associated with correlation such as metal-insulator transitions, heavy fermion behaviour, and high-temperature superconductivity. Various methods have been developed to extend the functional approach to incorporate effects that are expected to be important on physical grounds. Two of these are SIC and LDA+ U .

“SIC” denotes methods that use approximate functionals and add “*self-interaction corrections*” to attempt to correct for the unphysical self-interaction in many functionals for exchange and correlations E_{xc} . The self-interaction of an electron with itself in the Hartree

interaction cancels out - as already mentioned - in exact treatments of exchange, e.g. in the Hartree-Fock (HF) method. However, this is not the case for approximations to E_{xc} , and the errors can be significant since these terms involve large Coulomb interactions. There is a long history to such approaches, the first by Hartree himself [58] in his calculations on atoms. Hartree defined a different potential for each occupied state by subtracting a self-term due to the charge density of that state. In finite systems, implementing such corrections is straightforward; however, for an extended state in a solid, the correction vanishes since the interaction scales inversely with the size of the region in which the state is localized. Thus, in extended systems there is some arbitrariness in the definition of SIC.

An approach to extended systems has been developed in which a functional is defined with self-terms subtracted; minimization of the functional in an unrestricted manner allows the system of electrons to minimize the total energy by delocalizing the states (in a crystal, this is the usual Kohn-Sham solution with vanishing correction) or by localizing some or all states to produce a different solution. This approach has an intuitive appeal in that it leads to atomic-like states in systems such as transition metal oxides and rare earth systems where the electrons are strongly interacting. This is often considered to be a better starting point for understanding such materials than the *mean-field* Kohn-Sham solution. For example, studies using the SIC-LSDA have led to an improved description of the magnetic state and magnetic order in transition metal oxides [59], high T_c materials [60], and $4f$ occupation in rare earth compounds [61].

The acronym “LDA+ U ” stands for methods that involve LDA- or GGA-type calculations coupled with an additional orbital-dependent interaction [62, 63]. The additional interaction is usually considered only for highly localized atomic-like orbitals on the same site, i.e. of the same form as the “ U ” interaction in Hubbard models. The effect of the added term is to shift the localized orbitals relative to the other orbitals, which attempts to correct errors known to be large in the usual LDA or GGA calculations.

The GGA+ U approach (available in the *VASP* code) is important for reproduction of tiny magnetic effects in complex transition oxides, but less useful for surface defect properties under our study. Another disadvantage of this approach is that the U -parameter usually is not known and must be (directly or indirectly) fitted to some observed material characteristics (band gap, etc.). Of more promise is the use of the so-called *hybrid* functionals where non-local Hartree-Fock exchange energy is combined with LDA or GGA functionals [64]. In recent years, hybrid DFT-HF Hamiltonians combined with the LCAO basis set attracted considerable attention due to their ability to reproduce very well the electronic and magnetic

structure and, in particular, the optical gap of the ABO_3 perovskites [65]. The DFT approach overestimates delocalization of the electron density due to non-exact cancellation of the electron self-interaction. This effect is important for well-localized Mn atom electrons in $LaMnO_3$ and is partly taken into account in SIC-LDA approach. As an alternative, the hybrid functionals were used, which take into account an explicit orbital dependence of the energy through non-local part of the exchange (see more in a review article [66]). This approach is widely used in computer codes with local (atomic) basis sets, e.g. *CRYSTAL* and is expected to be incorporated into an upcoming version of the *VASP* code.

3 Computational Details

3.1 Treatment of the core electrons

The strong Coulomb potential of the nucleus and the influence of the core electrons on the valence electrons could be simulated as an effective ionic potential, the so called *pseudopotential* (PP). Since the core states remain almost unchanged, once generated in an atomic calculation, PP could be used to compute properties of valence electrons in various molecules and solids. Beside ultra-soft Vanderbilt PPs (USPP) *VASP* package additionally provides projector-augmented wave (PAW) method (Ch. 2.1). For both methods two types of approximation are available: local density approximation (LDA) and generalised gradient approximation (GGA). There is still more than one type of *Potential* for each chemical element for a particular method and approximation. Depending on the cutoff energy and the content of the core, Potentials come in the following versions: soft (*_s), standard (*), hard (*_h), with *d*- (*_d) or *p*-states (*_pv) treated as valence. Which type of Potential for particular combination of ion-electron interaction and approximation should be chosen depends on the character of bonding between the ions in the system [32].

Potentials for all three elements of the LaMnO_3 compound are available in PAW version only: two GGA and one LDA set. Their main properties are shown in Table 3.1.

Table 3.1. PAW potentials supplied with the *VASP* package.

element	Potential	valence electrons		Perdew-Wang 91	Perdew-Burke- Ernzerhof	Ceperley-Alder parameterized by Perdew and Zunger
		number	configuration	$E_{\text{cut}}, \text{eV}$	$E_{\text{cut}}, \text{eV}$	$E_{\text{cut}}, \text{eV}$
La	standard	11	$5s^2 6s^2 5p^6 5d^1$	219.271	219.313	219.044
	soft	9	$6s^2 5p^6 5d^1$	136.553	136.552	136.594
Mn	standard	7	$3d^6 4s^1$	269.887	269.865	269.944
	<i>p</i> semi core	13	$3p^6 3d^6 4s^1$	269.887	269.865	269.944
O	standard	6	$2s^2 p^4$	400	400	400
	soft	6	$2s^2 p^4$	250	282.841	282.604
	hard	6	$2s^2 p^4$	700	700	765.442

Potentials for the compound could be obtained as a combination of the Potentials of different type within one exchange correlation functional. Thus for LaMnO_3 twelve possible sets are available for each type of functional.

Lattice constant optimization has been performed for all of these sets. Optimized lattice constants and their root mean square deviation (RMSD) with respect to the experimental values $a_0 = 5.5367 \text{ \AA}$, $b_0 = 5.7473 \text{ \AA}$, $c_0 = 7.6929 \text{ \AA}$ (orthorhombic phase) [67] are given in Table 3.2.

Table 3.2. Optimized lattice constants and the root mean square deviation (in Å) for different sets of potentials.

combination of the elements			PW91				PBE				CA			
			a	b	c	RMSD	a	b	c	RMSD	a	b	c	RMSD
La	Mn	O_s	5.55	5.71	7.65	0.06	5.55	5.73	7.67	0.03	5.47	5.58	7.49	0.27
La_s	Mn	O_s	5.57	5.73	7.67	0.05	5.57	5.74	7.68	0.04	5.49	5.61	7.51	0.23
La_s	Mn_pv	O_s	5.56	5.72	7.66	0.05	5.57	5.74	7.68	0.04	5.49	5.61	7.51	0.24
La	Mn_pv	O_s	5.55	5.70	7.64	0.07	5.56	5.72	7.66	0.05	5.46	5.57	7.46	0.30
La_s	Mn	O	5.55	5.73	7.66	0.05	5.57	5.73	7.66	0.05	5.48	5.61	7.50	0.25
La_s	Mn_pv	O	5.56	5.72	7.65	0.05	5.57	5.73	7.66	0.05	5.48	5.61	7.50	0.25
La	Mn_pv	O	5.55	5.71	7.63	0.08	5.54	5.72	7.65	0.05	5.42	5.38	7.48	0.44
La	Mn	O	5.54	5.71	7.63	0.07	5.55	5.71	7.64	0.06	5.45	5.56	7.45	0.32
La_s	Mn_pv	O_h	5.53	5.68	7.61	0.11	5.53	5.69	7.62	0.10	5.49	5.61	7.50	0.25
La_s	Mn	O_h	5.52	5.68	7.61	0.11	5.53	5.68	7.61	0.10	5.48	5.61	7.50	0.25
La	Mn_pv	O_h	5.51	5.66	7.59	0.14	5.52	5.67	7.60	0.13	5.45	5.56	7.45	0.32
La	Mn	O_h	5.51	5.66	7.59	0.14	5.51	5.67	7.60	0.13	5.46	5.45	7.46	0.38

All sets of the GGA Potentials give much smaller deviation than those of the LDA. The deviations for both GGA sets are comparable and are in the range of 0.03-0.14 Å. The oxygen Potential is supposed to be the main factor as to affect the optimized values of the lattice constants. Choosing *soft* or *standard* versions of the Potential helps to keep RMSD smaller than 0.08 Å (1.5% of a_0). For PBE the *soft* version of the Potential gives slightly better results.

3.2 Setting the k-point mesh

At every cycle of the self-consistent procedure an approximate electron density matrix is evaluated by integration over the Brillouin zone (BZ). In real calculations integration is always performed in a finite mesh. There are several procedures for generating such a mesh. One of the most popular of them is the *Monkhorst-Pack* (MP) scheme [68].

$$N_i = \max(1, l * |\vec{b}_i| + 1/2), \quad (3.1)$$

where $i = 1..3$, \vec{b}_i - the reciprocal lattice vector, and $|\vec{b}_i|$ - its norm.

The MP \mathbf{k} -points mesh is defined by equally spaced points with coordinates:

$$\vec{k} = \sum_{i=1}^3 \vec{b}_i \frac{n_i}{N_i}, n_i = 0, \dots, N_i - 1 \quad (3.2)$$

Generated by this method, the grid could be shifted with respect to the Γ -point, when needed:

$$\vec{k} = \sum_{i=1}^3 \vec{b}_i \frac{n_i + 1/2}{N_i}. \quad (3.3)$$

There is a modified version of the MP method, which allows one to achieve faster convergence, with a smaller number of \mathbf{k} -points by shifting the mesh [69].

4 Perfect LaMnO₃ Crystal

Ab initio calculations of the perfect bulk LMO electronic structure were performed earlier in the HF LCAO approximation [70, 71], the LDA PW method [72], and the relativistic full-potential-GGA LAPW [73]. Two LMO phases were considered: the low- and the high-temperature modifications shown in Figure 4.1. The low-temperature LMO structure is orthorhombic (comprising four formula units, space group Pbnm-Figure 4.1a) with the experimental values of the lattice parameters being: $a_0 = 5.5367 \text{ \AA}$, $b_0 = 5.7473 \text{ \AA}$, $c_0 = 7.6929 \text{ \AA}$ [67]. There are several effects characteristic for this structure: the *Jahn-Teller distortion* [74] (to be discussed below), as well as mutual *tilting* and *rotation* of MnO₆ octahedra (Figure 4.4). Neglect of these effects transforms the orthorhombic structure into the tetragonal one (Figure 4.1b) also used in some calculations. At high temperatures (above 750 K) LMO transforms into the ideal perovskite structure (space group $Pm\bar{3}m$) with five atoms (one formula unit) per primitive *cubic* unit cell (Figure 4.2), with the experimental lattice constant $a_0 = 3.947 \text{ \AA}$ [67].

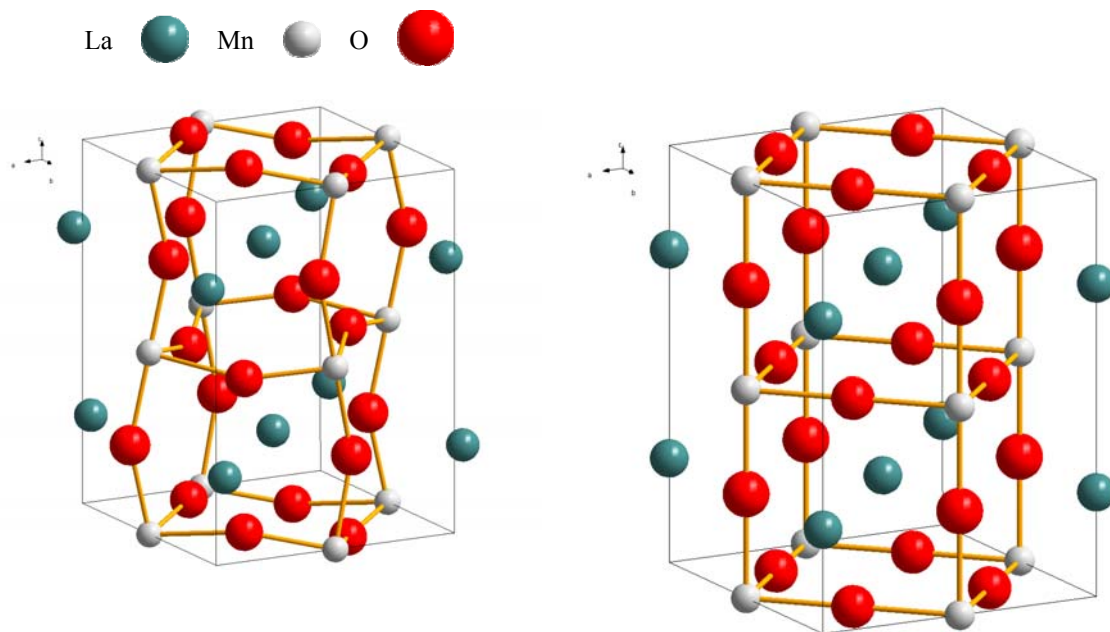


Figure 4.1.

a) Orthorhombic GdFeO₃-type crystal structure of LMO.

b) Tetragonal LMO with $a_0 = b_0 = \sqrt{2}c_0$.

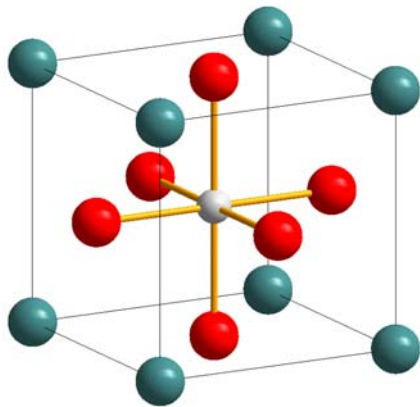


Figure 4.2. Cubic LMO.

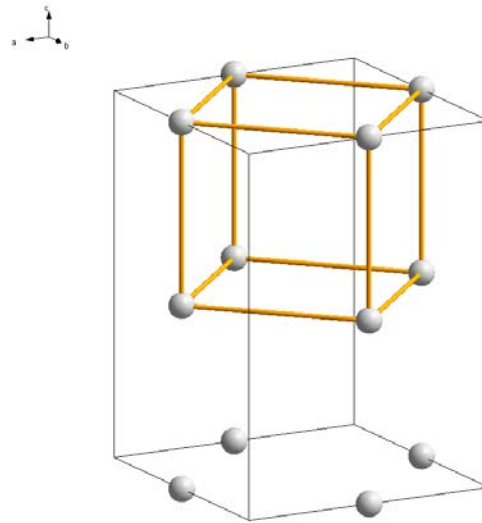


Figure 4.3. Mn ion sublattice of a cubic LMO.

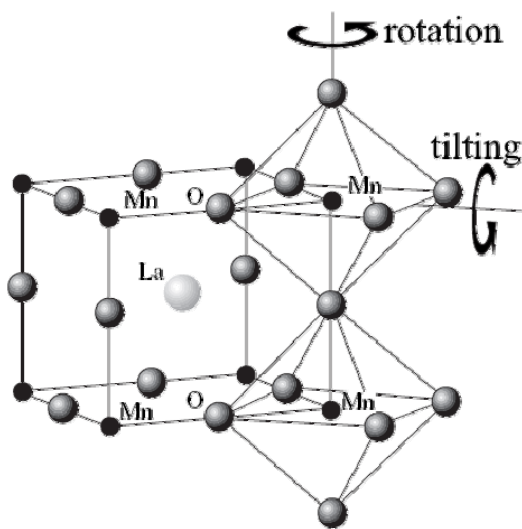


Figure 4.4. MnO_6 octahedra in the LMO structure. Taken from [21].

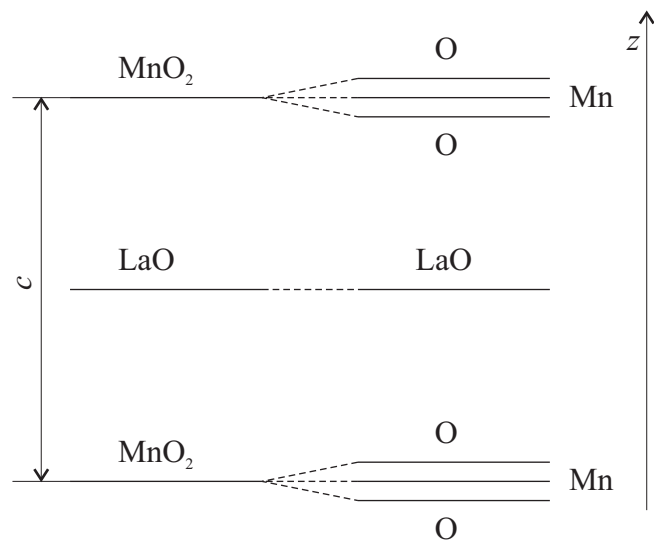


Figure 4.5. Splitting the (001) planes caused by MnO_6 octahedra tilting.

4.1 Magnetic properties

Depending on the four Mn spin orientations in the orthorhombic unit cells of 20 atoms (Figure 4.1a), there are four possible *magnetic* arrangements.

Ferromagnetically coupled Mn spins give rise to 3-, 2-, 1- and 0-dimensional infinite domains (Figure 4.6) in the respective ferromagnetic (FM), and antiferromagnetic (AFM): A-, C- and G-AF orderings. Mn spins from any two nearest domains are antiferromagnetically coupled.

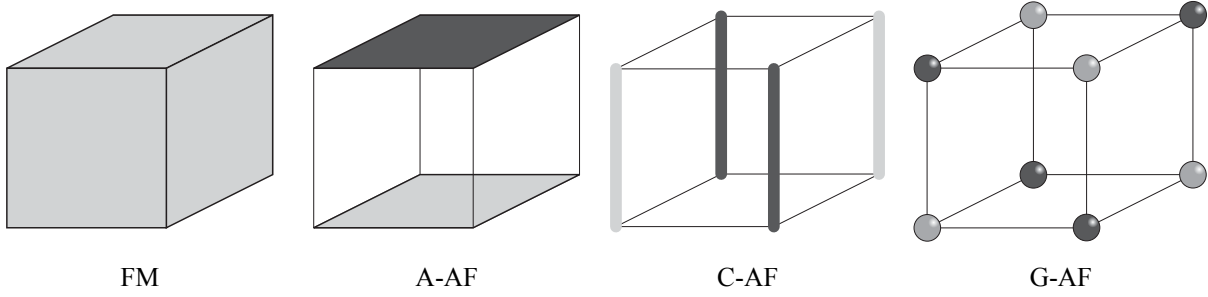


Figure 4.6. High symmetry magnetic orders in the base centred orthorhombic cell of the Mn sublattice (Figure 4.3). Black and gray colours indicate Mn ions with opposite spin orientations, respectively.

The fifth option of the ferromagnetic ordering, where the spin of one of the four Mn atoms in the cell is antiparallel to those of the other three, was neglected in this study. Neglect of spins on the Mn atoms corresponds to the non-magnetic (NM) state.

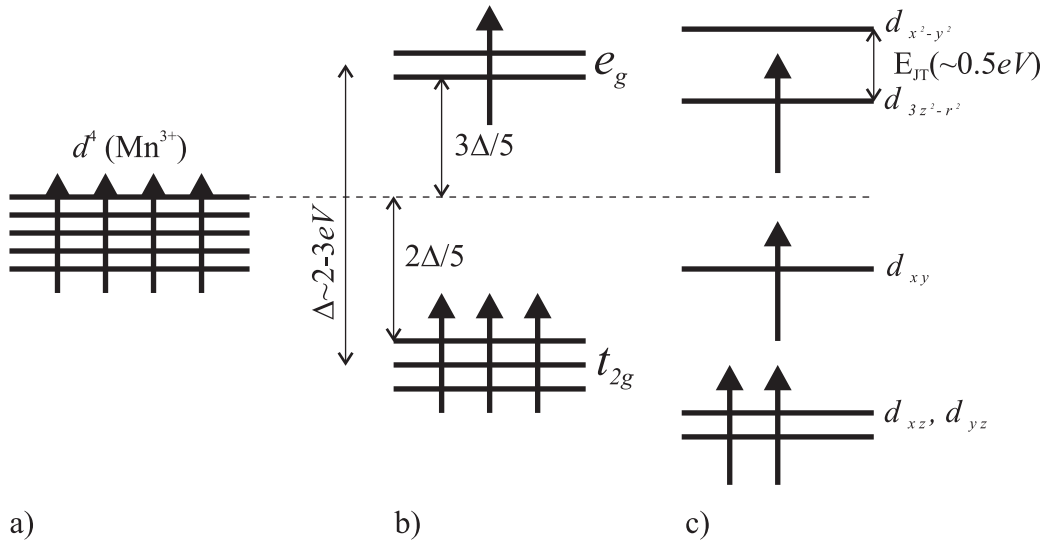


Figure 4.7. The orbital degeneracy of 3d-transition metal, (a) atomic orbitals in free ions, crystal-field splitting in a cubic (b) and tetragonal (c) environment.

The ground state electronic configuration of a single Mn^{3+} ion is $t_{2g}^3 e_g^1$ (all four electrons have the same spin projection, i.e. a high spin state). Comparison with HF LCAO calculations, presented in Ref. [79], shows that for Mn^{3+} ion in a crystal *Hund's rule* holds and the lowest energy corresponds to the maximal spin projection, $S_z = 2$, irrespective of the method used (Table 4.1).

Table 4.1. The relative energies (in eV) per one formula unit for the different spin projections on the Mn ion. For zero energy is taken that for the $S_z = 0$, with optimized for a spin projection $S_z = 2$ lattice constant.

x-c. functional \ S_z	2	1
PBE	-1.10	-0.60
PW91	-0.87	-0.53

In Table 4.1 we compare the total energies for the cubic primitive unit cell of 5 atoms obtained in non- and spin-polarized calculations with different magnetic ordering of four d -electrons on Mn^{3+} ion: total spin projection $S_z = 2$ (four α electrons, all with spins up, occupy t_{2g} and e_g levels), $S_z = 1$ (three α electrons and one β electron occupy t_{2g} level) and $S_z = 0$ (two α electrons and two β (spin down) electrons occupy t_{2g} level).

The *atomic charges* calculated (Table 4.2) show a weak dependence on the magnetic ordering, but indicate a considerable dependence on the functional used. At any rate, La and Mn charges are close to $+2 e$, whereas those for O are close to $-1.3 e$. Such a considerable deviation from formal charges ($+3$, $+3$ and -2 , respectively) arises due to essential covalence of the chemical bonding.

Table 4.2. Bader atomic charges [75, 76] (in e) for the different spin projections on the Mn ion.

ion x-c. functional \ S_z	La			Mn			O		
	2	1	0	2	1	0	2	1	0
PBE	1.92	1.91	1.92	1.97	1.90	1.80	-1.31	-1.28	-1.25
PW91	2.24	2.13	2.10	1.86	1.77	1.75	-1.38	-1.31	-1.30

Essential for the magnetic structure are the *magnetic coupling constants*. These are defined using Ising Model Hamiltonians:

$$H = -J_{ab} \sum_{ij} S_{zi} S_{zj} - J_c \sum_{kl} S_{zk} S_{zl}, \quad (4.1)$$

where J_{ab} and J_c are exchange integrals (*magnetic coupling constants*) between nearest neighbors in the basal plane (xy) and between nearest neighbors along the c axis, respectively, S_{zi} stands for the z component of the total spin referring to the magnetic center numbered i , and (ij) and (kl) indicate summation over intraplane and interplane nearest magnetic centers, respectively. We stress that Eq. (4.1) gives - due to possible choice of the Ising Hamiltonian presentation - positive values for J_{ab} and negative ones for J_c , and contains double summation over each pair of centers. The latter must be taken into account in a comparison with the experimental data. In particular, experimental J_{ab} and J_c values [77] have to be multiplied by a factor of 2.

By performing summation in Eq. (4.1) for the ABO_3 crystalline structure (Figure 4.2), the magnetic coupling constants could be calculated based on the following equations [79]:

$$E_{FM} - E_{AAF} = -32 J_c \quad (4.2)$$

$$E_{FM} - E_{CAF} = -64 J_{ab}, \quad (4.3)$$

Table 4.3. Magnetic coupling constants J_c and J_{ab} (in meV).

x-c. functional	J_c	J_{ab}
Expt. [80]	-1.2	1.6
PBE	-0.81	3.77
PW91	-1.73	2.99

where E is the total energy in different magnetic configurations (per 20-atom unit cell). As follows from Table 4.3, *VASP* results are in a qualitative agreement with the experimental data. However, as effective charges, these results strongly depend on the functional used. A comparison of these results with those obtained by means of the HF LCAO method [79] shows a similar order of magnitude agreement for both approaches.

4.2 Orthorhombic phase

4.2.1 Structure optimization

The crystallographic structure optimized by any theoretical method based on approximations differs from the experimental one. This difference could be expressed in terms of *rescaling* real system lattice constants in the artificial computational space. Since atoms are located within and with respect to the periodically repeated unit cell, their positions are affected to a lower degree than the lattice parameters. Taking this fact into account, the crystalline structure has to be rescaled first, whereas the atoms could be allowed to optimize their positions later. Performing atomic optimization prior to the rescaling could cause uncontrolled transitions in the system. For example, as observed in Ref. [72], during internal coordinate optimization using the determined experimentally lattice constant, the Jahn-Teller distortion rapidly reduces and the magnetic ordering switches from A-AF to FM. It happens because the experimental lattice constants the system in the “computational real space” and there are no more forces to keep the internal distortion; as a consequence, the system switches to the FM state. At the same time, the interdependence between the lattice parameters and the atomic coordinates should not be neglected. When the lattice is rescaled and the atomic positions are optimized within the optimized cell, the largest part of the stress is eliminated. But there is a small residual lattice-atomic stress which still persists. At this point, the system could be allowed to relax according to all its parameters without a high risk of an unwanted transition.

The LMO bulk structure optimization in the present study has been performed in four steps. As a first step, the lattice constants and the internal atomic coordinates were fixed according to the experimental data [67]. As a second step, the lattice constants were allowed to vary independently, when the atomic coordinates retained the experimental values. As a third step, atomic coordinates were optimized along with the lattice constants, obtained from

the previous calculation, which now were kept fixed. As a last step, the total geometry optimization has been made.

During the structure optimization, three key parameters were monitored: the total energy, the lattice distortion, and the MnO_6 octahedra distortion. The geometry distortion was expressed in terms of the standard statistical deviation:

$$\sigma = \sqrt{\frac{1}{N} * \sum_{n=1}^N \left(\frac{x - x_u}{x_u} \right)^2}, \quad (4.4)$$

where x stands for the parameter of a distorted system, and x_u is the parameter of the undistorted structure of the same volume, N - number of independent parameters.

The experimental LMO structure (Figure 4.1a) can be viewed as a highly distorted cubic perovskite (Figure 4.1b) with a quadrupled unit cell $(a_p\sqrt{2}, a_p\sqrt{2}, 2a_p)$. For the lattice distortion a , b and c were taken as parameters, normalised to $\sqrt[3]{a \cdot b \cdot c} = a_p\sqrt{2}$. For the MnO_6 octahedra distortion – we consider three (Mn-O) distances along the orthogonal axis: $(\text{Mn-O})_s$, $(\text{Mn-O})_m$ and $(\text{Mn-O})_l$, normalised by the (Mn-O) distance of a regular octahedron of the same volume: $\sqrt[3]{(\text{Mn-O})_s \cdot (\text{Mn-O})_m \cdot (\text{Mn-O})_l}$.

Table 4.4. Consecutive optimization.

property	optimization step			
	#1	#2	#3	#4
lattice constants	expt.	optimized	fixed from #2	optimized
atomic coordinates	expt.	fixed from #1	optimized	optimized

Table 4.5. The calculated cohesive energies (in eV). The experimental estimate of the cohesive energy is 30.3 eV [78].

step	#1	#2	#3	#4
FM	-30.91	-30.92	-30.98	-30.99
AAF	-30.92	-30.93	-30.95	-30.96
CAF	-30.86	-30.87	-30.88	-30.88
GAF	-30.85	-30.86	-30.88	-30.89
NM	-29.76			

The calculated cohesive energies of the four magnetic configurations, FM, A-, C- and G-AF, could be conditionally divided into two groups (Figure 4.8): FM/AAF and CAF/GAF. The difference within these groups does not exceed 0.035 eV, while the difference between the two energy groups is about twice as large viz. 0.065 eV. The difference between the groups remains constant throughout the optimization process. Notice that the NM state was excluded from the further structure optimization since its cohesive energy greatly exceeds those for the magnetic states.

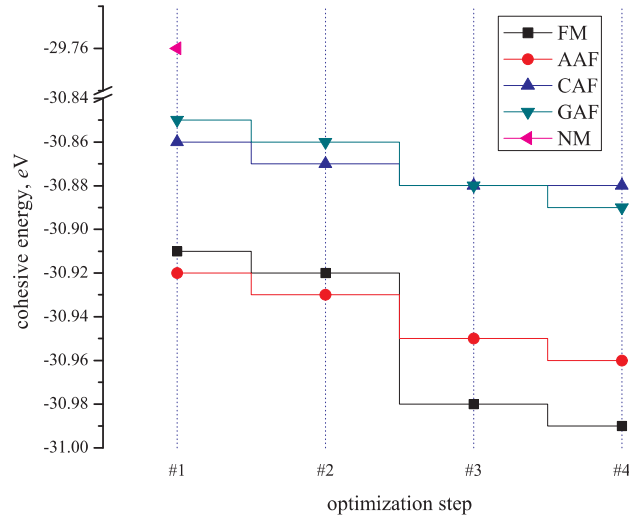


Figure 4.8. The cohesive energy of the orthorhombic LMO cell per one formula unit (in eV) (Table 4.5).

The sequence of cohesive energies for the different magnetic configurations (see Table 4.4) does not change for the first two steps, when the atomic coordinates were fixed. Lattice constant rescaling (step #2) lowered the total energy by ~ 0.01 eV/f.u. for each magnetic state. In full agreement with the experiment, the lowest energy corresponds to the AAF structure. Recent LDA PW calculations [72] also suggest the same energetic AAF/FM ranging for the experimental geometry. Since the unit cell in the AAF state expanded symmetrically at the second step, its shape practically does not change (Table 4.6). Simultaneously, the FM and CAF cells tend to reduce a lattice distortion (Figure 4.9). In contrast, a cell in the GAF state shows a continuous growth of both lattice and octahedral distortion in the course of the structure optimization.

The order of energies at the third step changes within the FM/AAF and CAF/GAF groups. The CAF/GAF energies coincide, whereas the FM energy becomes much lower than that for the AAF. This results from a considerable octahedra distortion reduction for the FM state. The MnO_6 octahedra for the AAF state become less disturbed among all AFM states (Figure 4.10).

Lastly, at the stage #4, all magnetic states, except the C-AF, lowered their energies by ~ 0.01 eV/f.u. The CAF energy did not change. This is also true for both CAF distortions (Figure 4.9 and Figure 4.10). The lattice constant distortions were equally reduced for the AAF and FM states. The MnO_6 octahedra distortion for these states was also reduced, however retaining the sequence of the magnetic states (the largest effect is observed for the AAF).

In contradiction to the experimental data, the optimization shows that the FM state is slightly more stable than A-AF. However, the energies of these two states are very close and

change order during full structure optimization. The same conclusions were drawn in Ref. [72].

Table 4.6. Optimized LMO lattice constants (in Å).

magnetic ordering	optimization step								
	#1			#2 and #3			#4		
	a	b	c	a	b	c	a	b	c
FM				5.59	5.72	7.78	5.56	5.61	7.87
AAF	5.5367	5.7473	7.6929	5.59	5.77	7.69	5.57	5.66	7.78
CAF				5.56	5.74	7.76	5.52	5.76	7.80
GAF				5.57	5.81	7.66	5.53	5.99	7.62

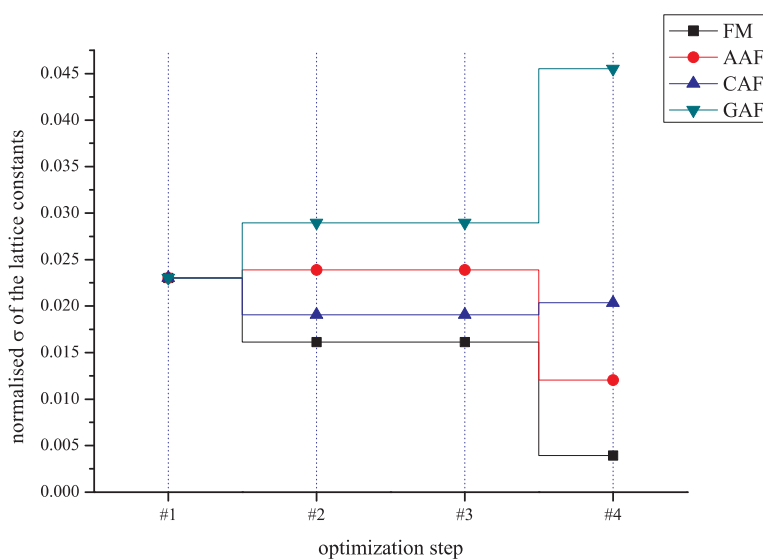


Figure 4.9. Normalised standard deviation (σ) of the lattice constants.

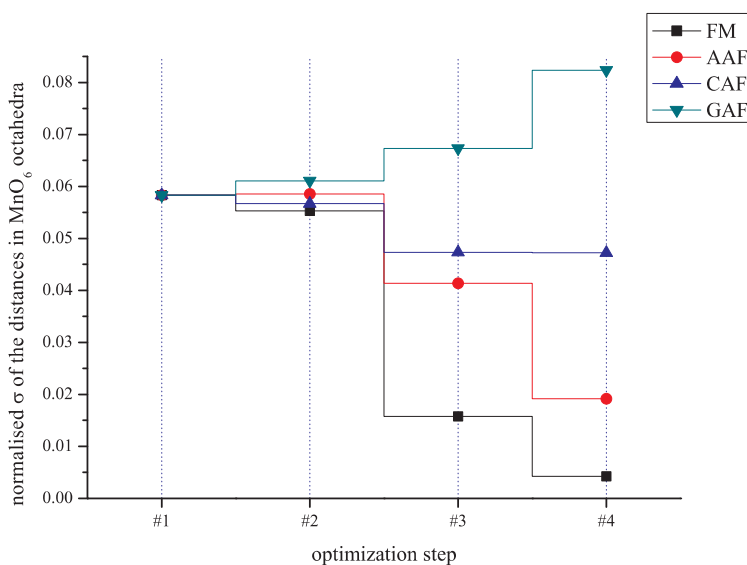


Figure 4.10. Normalised standard deviation (σ) of the MnO_6 octahedra.

Table 4.7. Geometrical parameters characterizing the crystal structure of the LMO during optimization. Short, medium, long and normalising constant distance - $\langle \text{Mn-O} \rangle$, Jahn-Teller distortion normal modes: orthorhombic $Q_2=2(l-s)/\sqrt{2}$ and tetragonal $Q_3=2(2m-l-s)/\sqrt{6}$ in Å. Normalised standard deviation σ of the MnO_6 octahedra.

magnetic ordering		#1	#2	#3	#4
FM	Mn-O(1) s		1.915	1.994	2.010
	Mn-O(2) m		1.990	2.022	2.013
	Mn-O(2) l		2.181	2.072	2.029
	$\langle \text{Mn-O} \rangle$		2.026	2.029	2.018
	Q_2		0.376	0.109	0.028
	Q_3		-0.095	-0.017	-0.010
	σ		0.055	0.016	0.004
AAF	Mn-O(1) s	1.906	1.920	1.968	1.988
	Mn-O(2) m	1.968	1.969	1.976	1.994
	Mn-O(2) l	2.180	2.192	2.150	2.073
	$\langle \text{Mn-O} \rangle$	2.015	2.024	2.029	2.018
	Q_2	0.388	0.385	0.257	0.120
	Q_3	-0.122	-0.142	-0.135	-0.060
	σ	0.058	0.059	0.041	0.019
CAF	Mn-O(1) s		1.910	1.942	1.938
	Mn-O(2) m		1.986	1.990	1.997
	Mn-O(2) l		2.182	2.165	2.164
	$\langle \text{Mn-O} \rangle$		2.023	2.030	2.031
	Q_2		0.385	0.316	0.320
	Q_3		-0.098	-0.104	-0.088
	σ		0.057	0.047	0.047
GAF	Mn-O(1) s		1.919	1.916	1.918
	Mn-O(2) m		1.960	1.968	1.959
	Mn-O(2) l		2.199	2.229	2.295
	$\langle \text{Mn-O} \rangle$		2.022	2.033	2.051
	Q_2		0.396	0.442	0.532
	Q_3		-0.161	-0.171	-0.241
	σ		0.061	0.067	0.082

4.2.2 The electronic structure

To characterise the electronic density distribution, the topological (Bader) *atomic charges* were calculated [75, 76] during optimization for different magnetic states (Table 4.8). The conclusion could be drawn that these charges remain almost constant, being insensitive to relatively small structure variations. *Magnetic moments* on Mn ions also remain almost unchanged (Table 4.9). Depending on the magnetic configuration, the absolute values of moments correlates with the dimensionality of the ferromagnetic domains (from FM to G-AF state (Ch. 4.1)). Spin polarisation for the FM state significantly differs from that for antiferromagnetic states.

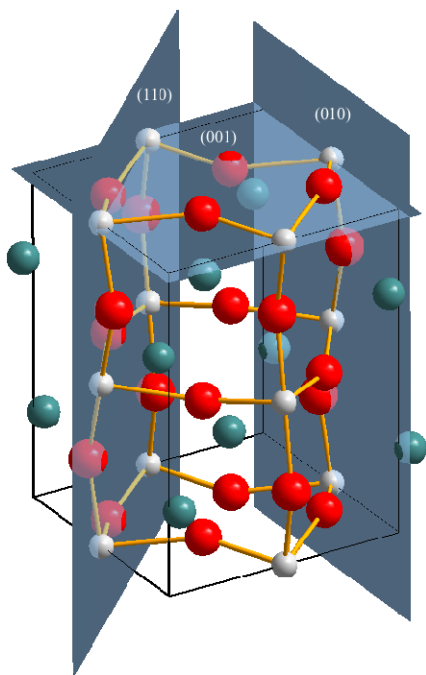
To get a deeper insight, the total and difference *electronic density maps* were plotted (Figure 4.12), for different crystal cross-sections shown in Figure 4.11.

Table 4.8. Bader atomic charges (in e).

		optimization step			
magnetic ordering	atom	#1	#2	#3	#4
FM	La	2.069	2.071	2.074	2.071
	Mn	1.682	1.672	1.683	1.676
	O	-1.241	-1.243	-1.250	-1.254
AAF	La	2.071	2.072	2.074	2.073
	Mn	1.680	1.671	1.676	1.676
	O	-1.241	-1.236	-1.238	-1.245
CAF	La	2.070	2.071	2.073	2.070
	Mn	1.673	1.668	1.666	1.666
	O	-1.238	-1.240	-1.241	-1.245
GAF	La	2.074	2.073	2.072	2.071
	Mn	1.666	1.654	1.636	1.635
	O	-1.234	-1.229	-1.223	-1.220

Table 4.9. Magnetic moments on Mn atom (in μ_B).

step	#1	#2	#3	#4
FM	3.98	3.99	3.98	3.96
AAF	3.50	3.51	3.52	3.49
CAF	3.42	3.42	3.42	3.42
GAF	3.32	3.34	3.36	3.40

Figure 4.11. Crystallographic planes of the LaMnO_3 used for the electron density maps plotting (Figure 4.12).

The total density (Figure 4.12) clearly demonstrates the MnO_6 octahedra tilting and rotation as discussed above (Figure 4.4). The La ion is well defined and its electronic density does not overlap with that of other ions. In contrast, there is a visible asymmetrical covalent chemical bonding between Mn and O ions. On the other hand, the *difference electron density* shows the Mn ion *orbital ordering* that is well observed experimentally in LMO [81]. This means an alternative occupation of $(3x^2-r^2)$ and $(3y^2-r^2)$ orbitals on nearest Mn ions in the ab plane and the same type of orbital occupation along the c axis, what is known as C-type antiferro-orbital arrangement [82].

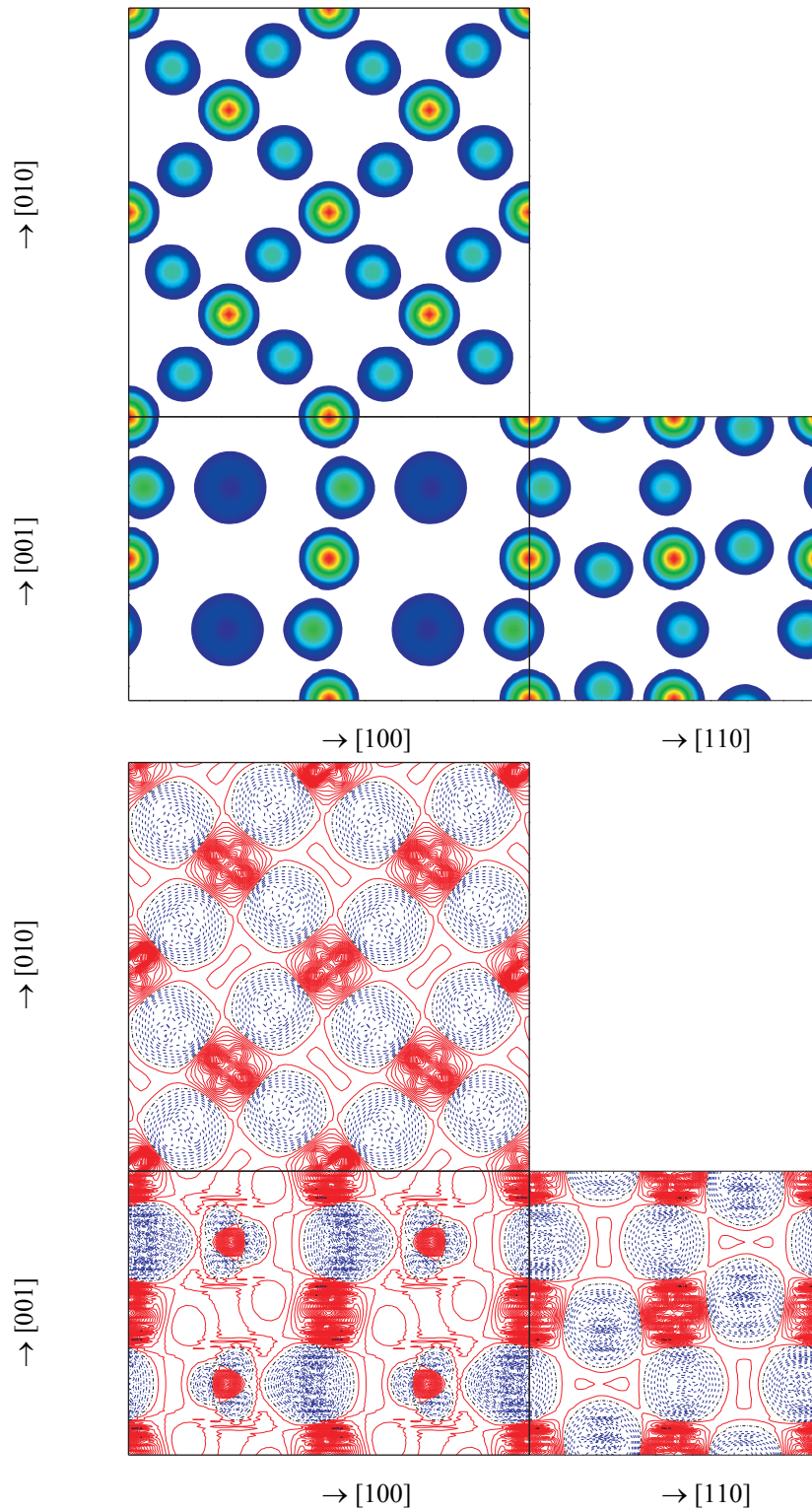


Figure 4.12. Total and difference electron density of the LMO bulk. The cross-sections are shown in the following order (from the top to the bottom): (001); (010), (110) (see Figure 4.11 for the planes layout). Total density contains the valence electrons only. Mn ions have a red spot at the center on the total density map. La ions are seen as dark blue circles. Difference density represents the self consistent total density minus a superposition of the atomic densities. Solid (red in colour) and dashed (blue in colour) lines correspond to the deficiency and excess in electronic density, respectively. Density increment $0.02 e/\text{\AA}^3$. The dash-dot black line is the zero level.

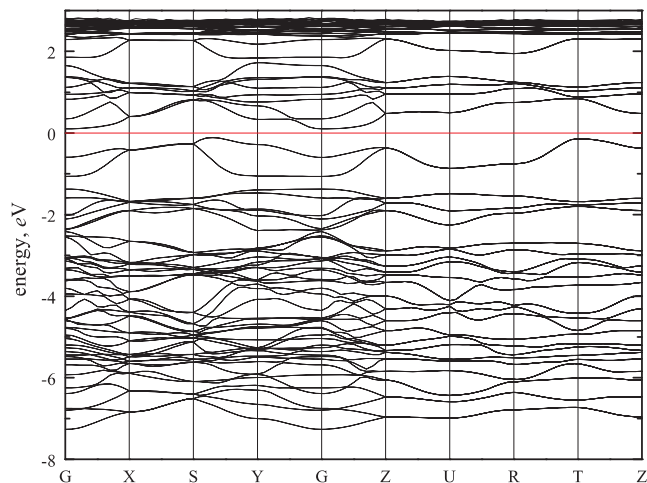


Figure 4.13. Band structure of orthorhombic LMO in the AAF phase (for experimental geometry). The energy is normalised to the Fermi level (red line).

Figure 4.13 shows the calculated *band structure* with the valence band top at the *S*-point of the Brillouin zone and the direct gap of ~ 0.6 eV. This is considerably smaller than the experimental value of 2 eV [21], a typical underestimate as known for the DFT calculations.

4.3 Cubic Phase

Our calculations on the cubic LMO structure (stable above 750 K) show the necessity of the spin-polarised approach which was debated in the literature. Indeed, the optimized lattice constant for the NM state indeed strongly deviates from those for four magnetic states, similar to the case of the orthorhombic cell. A critical comparison of the effective charges in the cubic (Table 4.10) and the orthorhombic (Table 4.8) unit cells shows a larger covalency of the Mn-O chemical bonding in the latter case.

Table 4.10. The optimized lattice constant (in Å), cohesive energy (in eV), excess of energy with respect to the optimized orthorhombic cell and atomic charges (in e) for LMO crystal in the tetragonal modification. Cohesive energy is given per one formula unit.

magnetic ordering	a_0	cohesive energy	ΔE	atomic charge		
				La	Mn	O
FM	3.90	-30.73	0.26	2.129	1.847	-1.291
AAF	3.90	-30.67	0.28	2.129	1.846	-1.294
CAF	3.91	-30.59	0.29	2.131	1.845	-1.289
GAF	3.91	-30.43	0.47	2.129	1.847	-1.291
NM	3.83	-29.95		2.112	1.742	-1.250
Expt.[78]	3.88	30.3				

The cohesive energy calculated for all magnetic states is in a good agreement with the experimental value. The neglect of geometry distortion in the orthorhombic cell increases the cohesive energy by at least $\frac{1}{4}$ of eV (per one formula unit) for all magnetic states. In the GAF case ΔE is significantly higher.

5 Surface Calculations

Understanding and control of surface properties of pure and doped LaMnO_3 is important for applications in fuel cells [2], magnetoresistive devices, and spintronics. However, manganite surface properties are studied very poorly, especially theoretically. We are familiar only with two reports of LSDA calculations on CaMnO_3 and $\text{La}_{0.5}\text{Ca}_{0.5}\text{MnO}_3$ (001) surfaces [84] and two SIC-LSD calculations on solid solution $\text{La}_{1-x}\text{Sr}_x\text{MnO}_3$ (001) surfaces [83]. These DFT studies focused mainly on low-temperature magnetic properties and neglected surface relaxation as well as surface energy calculations, let alone, defect or adsorbate properties.

Experimental studies in our department stimulated LaMnO_3 calculations with a focus on the (110) surface (using both classical shell model [85-87] and HF [35, 36]), and the (001) surface [35, 88] (HF and DFT-plane wave calculations). In these studies surface energy calculations were performed for stoichiometric and non-stoichiometric slabs with different terminations, and the electronic density redistribution near the surface was analyzed. However, surface relaxation was taken into account only in the shell model (110) calculations [85, 86, 87] and our recent *VASP* calculations for the (001) surface [88] to be discussed below. In this thesis the detailed calculations were performed for the slabs built both of orthorhombic and cubic unit cells in different magnetic states.

The *surface energy* quantifies the energy loss for disruption of chemical bonds that occur when a crystal is cleaved and a surface is created. It is calculated per unit area of a surface as the difference between the energy of the system terminated by the surfaces (slab) and the system of the same number of unit cells within the bulk. Slabs used in *ab initio* calculations have finite thickness, which has to be chosen large enough, so that the surface energy reaches its convergence level.

In this Chapter, we start with the calculations for the (001) surface, which has $\text{MnO}_2/\text{LaO}/\text{MnO}_2/\dots$ sequence of the oppositely charged planes ($\pm 1 e$, assuming formal ionic charges: Mn^{3+} , La^{3+} , O^{2-}). Table 5.1 schematically shows two types of slabs. The *stoichiometric* 8-plane (even number-plane, in general) slab (a) consists of a four LMO formula units (each pair of neighbouring planes gives a formula unit per unit area of surface). Its potential shortcoming is that this slab has a dipole moment normal to the surface, due to summation of the electrostatic fields all

Table 5.1. Plane sequence for the (001) 8-plane (a) and 7-plane MnO_2 (b) and LaO (c) terminated slabs.

a) LaMnO_3	b) $\text{La}_{0.75}\text{MnO}_{2.75}$	c) $\text{LaMn}_{0.75}\text{O}_{2.5}$
MnO_2	MnO_2	
LaO	LaO	LaO
MnO_2	MnO_2	MnO_2
LaO	LaO	LaO
MnO_2	MnO_2	MnO_2
LaO	LaO	LaO
MnO_2	MnO_2	MnO_2
LaO		LaO

planes [90]. Such a slab could be unstable with respect to a reconstruction or defect formation. Alternatively, the dipole moment can be cancelled by the charge redistribution near the surface (to be discussed below).

To get rid of the dipole moment, *symmetrical* slabs (Table 5.1b, c) are often used. Such slabs have an odd number of planes (typically 7 in our calculations) and the same terminations on both sides, MnO₂ or LaO. The problem is that each of such slabs is not stoichiometric, but two symmetrical slabs with different terminations as put together contain an integer number of bulk unit cells. In particular, for slabs in Table 5.1b and c $n = 7$.

Based on these considerations, two relations are used for the surface energy.

For stoichiometric slabs

$$E_{surf.} = \frac{1}{2S} \cdot (E_{slab} - n \cdot E_{bulk}), \quad (5.1)$$

where S is unit area of surface, E_{slab} total energy of the slab, n corresponding number of the bulk units, E_{bulk} total energy of the bulk unit. As a reference, the energies of the bulk unit cell of the corresponding structure and magnetic ordering were taken.

For non-stoichiometric slabs

$$E_{surf} = \frac{1}{4S} \cdot (E_{t1} + E_{t2} - n \cdot E_{bulk}), \quad (5.2)$$

where E_{t1} and E_{t2} denote the energies of the slabs with odd number of planes and complementary terminations, $n = 7$ for slabs (b, c) in Table 5.1.

Periodic first-principles calculations of the crystalline surfaces are usually performed considering a crystal as a stack of planes perpendicular to the surface and cutting out a 2D slab of finite thickness but periodic in the xy plane. A large gap of 15.8 Å between slabs periodically repeated along the z axis was used here to prevent interaction through the vacuum region between the two surfaces (see Figure 5.1). In the calculations atoms were allowed to move to the minimum of the total energy, while the parameters of the surface cell were kept constant.

5.1 The (001) surface

The results of calculations on unrelaxed (cleavage) and relaxed surface energy for the (001) slabs of different thicknesses are summarized in Table 5.2. The thickness of the slab was varied from 4 to 13 crystallographic planes. Starting already from the 6-plane slab both unrelaxed as well as relaxed surface energies do not change more than $0.02 \text{ eV}/a_0^2$ on a slab thickness increase. Thus, the 7-8-plane (001) slab can be considered as thick enough to

reproduce properties of the (001) surface. The calculated surface energy is quite low, but comparable with that for SrTiO₃ (001), viz. 1.2 eV [89]. The two different ways of surface energy calculation, using slabs with odd and even number of planes, Eq. (5.1) and (5.2), give similar results.

Table 5.2. Cleavage and relaxed surface energies (in eV/a_0^2) for the (001) slabs in the FM state. For a better comparison, slabs of even and odd number of planes are grouped in two different pairs of columns. The relevant energies were calculated using Equations (5.1) and (5.2), respectively.

N. of planes	cleavage	relaxed	cleavage	relaxed
4	1.64	0.76		
6	1.66	0.82		
7			1.58	1.01
8	1.66	0.82		
9			1.59	0.97
10	1.66	0.83		
11			1.60	0.96
12	1.67	0.84		
13			1.61	0.95

states and $4\mu_B$ for FM per one Mn atom), whereas in other calculations, the magnetic moment was self-consistently optimized.

The 7- and 8- plane slabs were chosen for the further calculations of the surface energy for slabs with different magnetic orderings (Table 5.3) which are similar to those in the bulk Figure 4.6. Calculations on 7-plane slabs were performed with both fixed and optimized total slab magnetic moments as discussed above for the bulk (Ch. 4.1). We studied how the magnetic ordering of a slab affects the results. In some calculations the total magnetic moment was fixed (0 for all AF

Table 5.3. Surface energies of the (001) surface (in eV/a_0^2) for different magnetic configurations.

slab	7-plane				8-plane	
	fixed		optimized		fixed	
	cleavage	relaxed	cleavage	relaxed	cleavage	relaxed
total magnetic moment						
FM	1.60	1.25	1.55	0.97	1.61	0.87
AAF	1.53	0.95	1.53	0.94	1.51	0.77
CAF	1.46	1.01	1.43	0.95	1.46	0.78
GAF	1.34	0.76	1.34	0.75	1.43	0.61
FM*	1.84	1.39	1.77	1.18	1.77	1.13

* orthorhombic slab

As follows from Table 5.3, the effect of magnetic moment optimization is seen only for slabs in the FM state with a relaxed geometry (changed by $0.28 eV/a_0^2$). For antiferromagnetic slabs this effect is negligible (less than $0.06 eV/a_0^2$). The lowest surface energy of 0.61 eV is found for the G-AF magnetic configuration. For a comparison, we calculated also the surface energy for the orthorhombic slab in the FM state. This energy exceed by 0.14-0.21 eV that for a cubic slab in the same magnetic state. Note also that the FM slabs, both cubic and orthorhombic, show a surface energy larger than that for all AFM slabs. A full slab *geometry optimization* was performed in the present calculations. For most slabs, built from cubic unit cells (Figure 4.2), due to the symmetry of their structure, only the z coordinate (Figure 5.1)

was varied. Even though, in the case of the orthorhombic FM slab some minor atomic moves in the planes parallel to the surface took place, but the largest atomic displacements were observed the same as for the cubic slabs along the z axis.

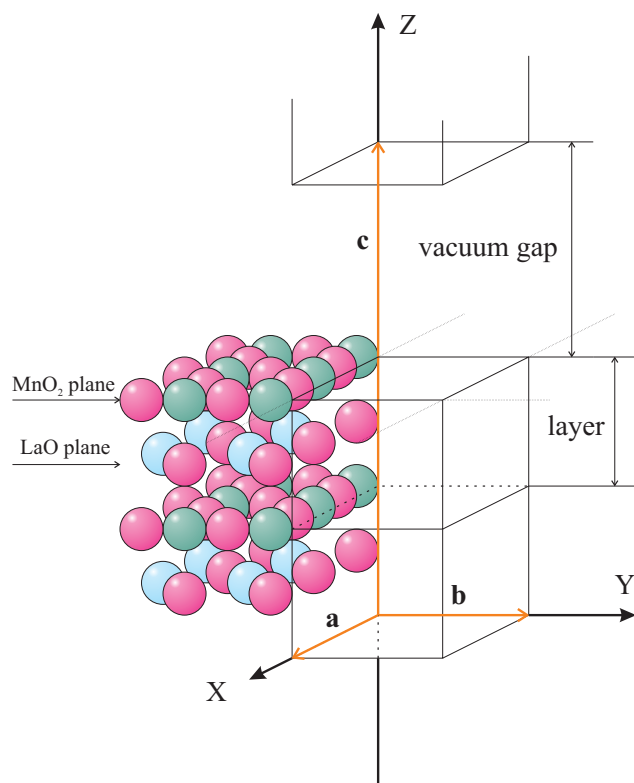


Figure 5.1. Four-plane slab model with indication of supercell parameters (a , b , c) and vacuum gap.

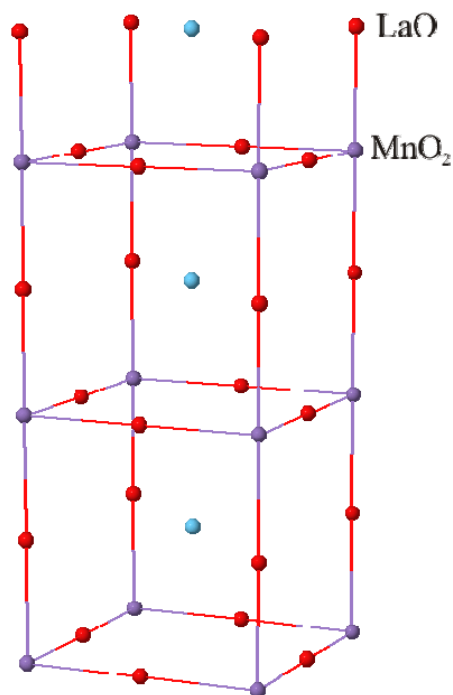


Figure 5.2. Schematic view of the unit cell (001) surface used in 2D slab calculations with even number of planes (no mirror plane). LaO planes alternate with MnO_2 ones along the direction normal to the surface. Primitive cubic unit cells, shown by solid lines, are the same as those in Figure 4.1b).

Changes in the slab geometry caused by its relaxation could be expressed in terms of interplanar and Mn-O relative distances in the MnO_6 octahedra along the $[001]$ direction perpendicular to the surface (Figure 4.4). These interplanar distances calculated for the optimized bulk structures are: LaO- MnO_2 - 1.95 Å, in a cubic cell, and LaO-O 1.66 Å, O-Mn - 0.31 Å, for orthorhombic cells (Figure 4.5) (in the latter case MnO_2 bulk plane is split). The O-Mn distance along the $[001]$ direction in the orthorhombic cell is 1.97 Å. All calculated slabs with different magnetic orderings for the corresponding terminations demonstrate similar atomic displacements. There is a small difference between the relaxation in the odd-plane slabs near the mirror plane and that in the central planes of the even-layer slabs, caused by symmetry of the slabs.

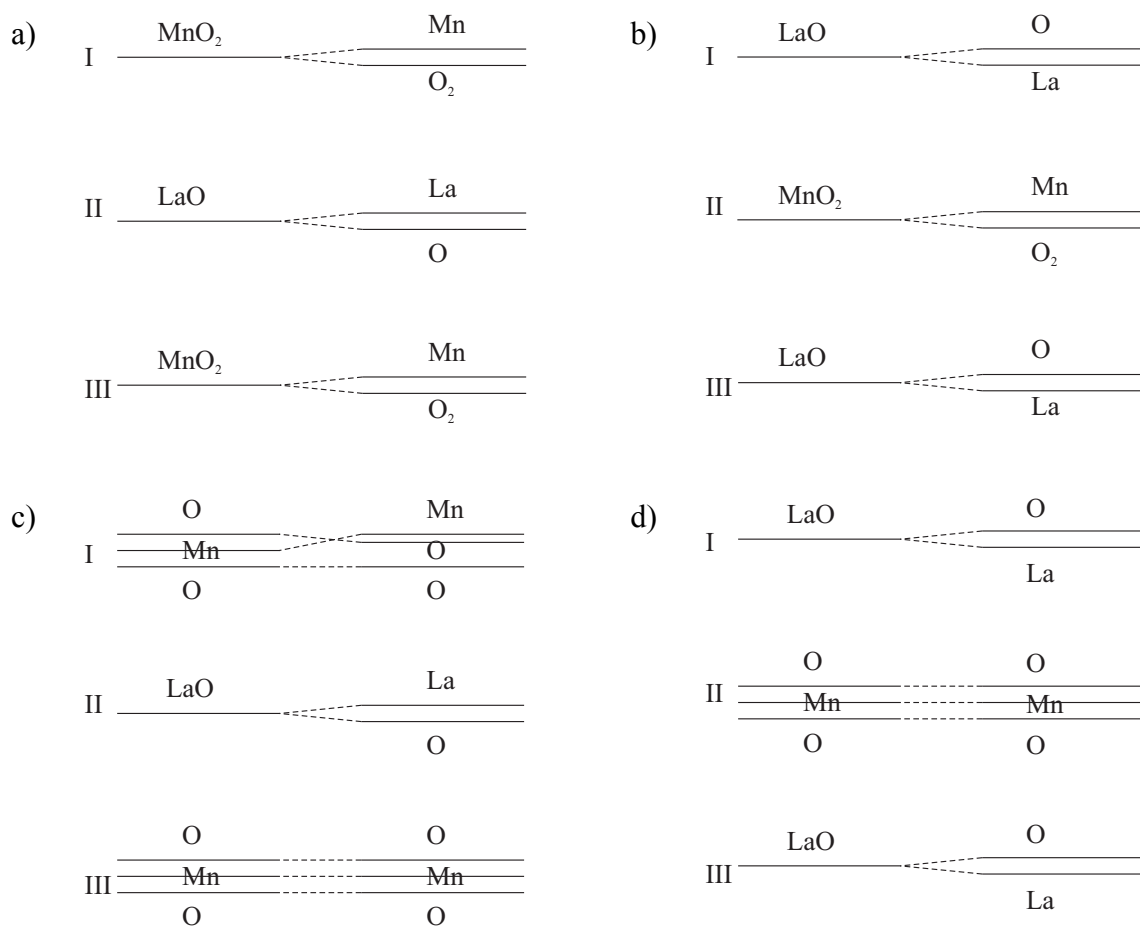


Figure 5.3. Plane rumpling and splitting in the (001) plane with respect to the bulk (left side) in cubic (a), (b), and orthorhombic (c), (d) slabs for MnO₂- (a), (c) and LaO-termination (b), (d).

There are four different (interplanar) distances in the relaxed cubic slabs: Mn-O₂ plane splitting, O₂-La distance, La-O splitting, and O-Mn (Figure 5.3a, b). These distances vary, depending on the proximity to the surface or particular termination, what can be easily identified in the 8-plane slabs (Table 5.6). The Mn-O₂ plane splitting and Mn-O interplanar separation distance constantly decreases and increases, respectively, when going along the [001] direction from the MnO₂ - towards the LaO-termination. La-O plane splitting is more pronounced in the surface planes for both terminations, whereas the O₂-La distance grows from the surface towards the slab centre.

Rumpling of the MnO₂ and LaO surface planes in the cubic slabs is about 0.19 Å and 0.44 Å, respectively (Table 5.4-Table 5.6). In the orthorhombic slabs due to the tilting of the MnO₆ octahedra (Figure 4.4) the MnO₂ plane splits into three subplanes (Figure 5.3c, d). As observed in Table 5.4 and Table 5.5, the sequence of the subplanes is the same as in the bulk (O-Mn-O), except for the terminating MnO₂ plane. This Mn-subplane moves up, leaving an O subplane below (Table 5.4 and Figure 5.3c). The move up of Mn ions from the the MnO₂

plane on the MnO₂-terminated surfaces was also observed for the cubic slabs. Instead, for the LaO-termination, La atoms are covered by oxygen subplane. This is true for all (001) slabs.

Table 5.4. The interplanar distance (in Å) in a relaxed 7-plane MnO₂-terminated slab.

plane	subplane	FM	AAF	CAF	GAF	plane	subplane	FM*
I	Mn-O ₂ **	0.19	0.19	0.15	0.16	I	Mn-O*	0.07
I-II	O ₂ -La	1.62	1.59	1.61	1.60	I-II	O-O*	0.17
II	La-O**	0.29	0.34	0.34	0.35	II	O-La	1.49
II-III	O-Mn	1.88	1.85	1.87	1.85	II-III	La-O*	0.34
III	Mn-O ₂ **	0.08	0.09	0.08	0.07	II-III	O-O	1.66
						III	O-Mn*	0.18
III-IV	O ₂ -LaO	1.88	1.85	1.86	1.85	III	Mn-O	0.29
						III-IV	O-LaO	1.65

* orthorhombic slab

** splitting of the bulk planes

Table 5.5. The interplanar distances (in Å) in a relaxed 7-plane LaO-terminated slab.

plane	subplane	FM	AAF	CAF	GAF	plane	subplane	FM*
I	O-La**	0.45	0.43	0.45	0.44	I	O-La*	0.39
I-II	La-O ₂	1.64	1.62	1.65	1.64	I-II	La-O	1.45
II	O ₂ -Mn**	0.00	0.00	0.04	0.06	II	O-Mn*	0.34
						II	Mn-O*	0.25
II-III	Mn-O	2.02	2.00	2.03	2.00	II-III	O-O	1.80
III	O-La**	0.11	0.09	0.08	0.08	III	O-La*	0.02
III-IV	La-MnO ₂	1.89	1.86	1.90	1.86	III-IV	La-O	1.63
						IV	O-Mn*	0.33

* orthorhombic slab

** splitting of the bulk planes

Table 5.6. The interplanar distances (in Å) in a relaxed 8-plane slab.

plane	subplane	FM	AAF	CAF	GAF	plane	subplane	FM*
I	Mn-O ₂ **	0.19	0.19	0.16	0.16	I	Mn-O	0.08
I-II	O ₂ -La	1.54	1.55	1.53	1.54	I	O-O	0.17
II	La-O**	0.39	0.39	0.42	0.43	I-II	O-La	1.47
II-III	O-Mn	1.88	1.88	1.87	1.87	II	La-O	0.37
III	Mn-O ₂ **	0.15	0.15	0.16	0.16	II-III	O-O	1.68
						III	O-Mn	0.16
III-IV	O ₂ -La	1.63	1.64	1.62	1.62	III	Mn-O	0.34
IV	La-O**	0.22	0.23	0.23	0.24	III-IV	O-La	1.53
IV-V	O-Mn	1.94	1.90	1.95	1.89	IV	La-O	0.13
V	Mn-O ₂ **	0.11	0.08	0.14	0.10	IV-V	O-O	1.70
						V	O-Mn	0.23
V-VI	O ₂ -La	1.67	1.67	1.64	1.69	V	Mn-O	0.36
VI	La-O**	0.26	0.21	0.28	0.17	V-VI	O-La	1.54
VI-VII	O-Mn	1.99	1.99	1.93	2.03	VI	La-O	0.10
VII	Mn-O ₂ **	0.06	0.04	0.09	0.06	VI-VII	O-O	1.79
						VII	O-Mn	0.23
VII-VIII	O ₂ -La	1.59	1.59	1.57	1.62	VII	Mn-O	0.33
VIII	La-O**	0.44	0.43	0.43	0.45	VII-VIII	O-La	1.44
						VIII	La-O	0.38

* orthorhombic slab

** splitting of the bulk planes

Lastly, Table 5.7 summarizes the Mn-O distance variation in MnO₆ octahedra along the *z* axis. As one can see, the upper side of the MnO₆ octahedra is regularly expanded, but the lower part compressed as compared to a perfect bulk octahedron.

Table 5.7. The relative Mn-O distances (in Å) along the [001] direction for 8- (a) and 7-plane (b) slabs, and their differences for these two slabs.

MnO ₂ termination														
8-plane					7-plane					8-plane minus 7-plane				
FM	AAF	CAF	GAF	FM*	FM	AAF	CAF	GAF	FM*	FM	AAF	CAF	GAF	FM*
2.12	2.12	2.12	2.13	2.09	2.10	2.12	2.11	2.12	2.07	0.02	0.00	0.01	0.01	0.02
1.88	1.88	1.87	1.87	1.85	1.88	1.85	1.87	1.85	1.84	-0.01	0.03	0.00	0.02	0.00
2.00	2.01	2.00	2.02	2.00	1.95	1.94	1.94	1.93	1.95	0.05	0.08	0.06	0.10	0.05
1.94	1.90	1.95	1.89	1.93	mirror plane									
2.03	1.96	2.07	1.95	1.99	2.00	1.95	1.98	1.94	1.97	0.04	0.01	0.08	0.00	0.02
1.99	1.99	1.93	2.03	2.01	2.02	2.00	2.03	2.03	2.05	-0.04	-0.01	-0.11	0.00	-0.04
2.10	2.06	2.09	2.13	2.15	2.09	2.05	2.15	2.14	2.18	0.01	0.01	-0.06	-0.01	-0.03

LaO termination

* orthorhombic slab

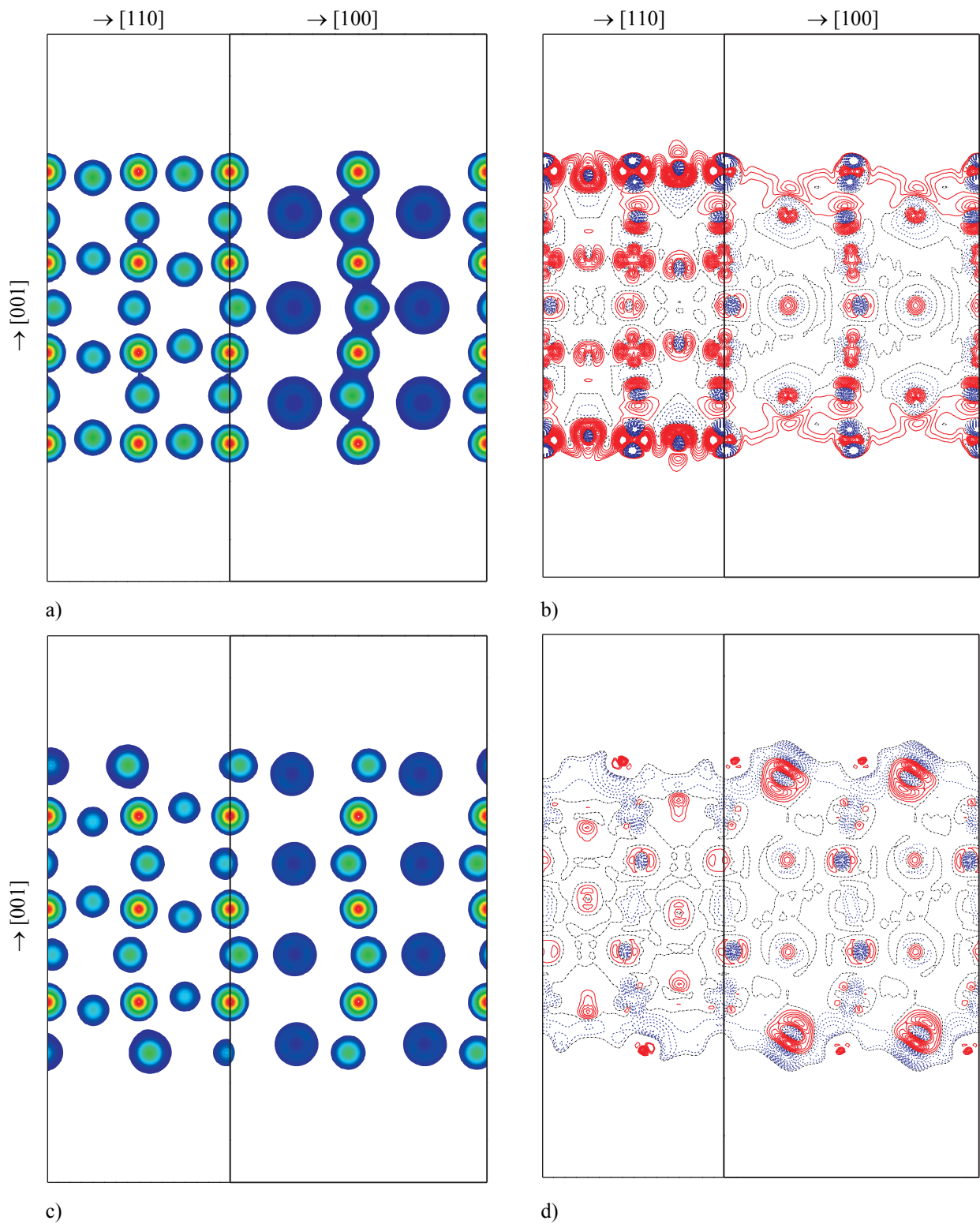


Figure 5.4. Total (a, c) and difference (b, d) electron density maps for 7-plane MnO_2 - (a, b) and LaO - (c, d) terminated slabs, respectively. Solid red and dash blue lines represent deficiency and excess of the electron charge, respectively. Density increment is $0.005 e/\text{\AA}^3$. Dash-dot black line is the zero level. See Figure 4.12 for ions identification.

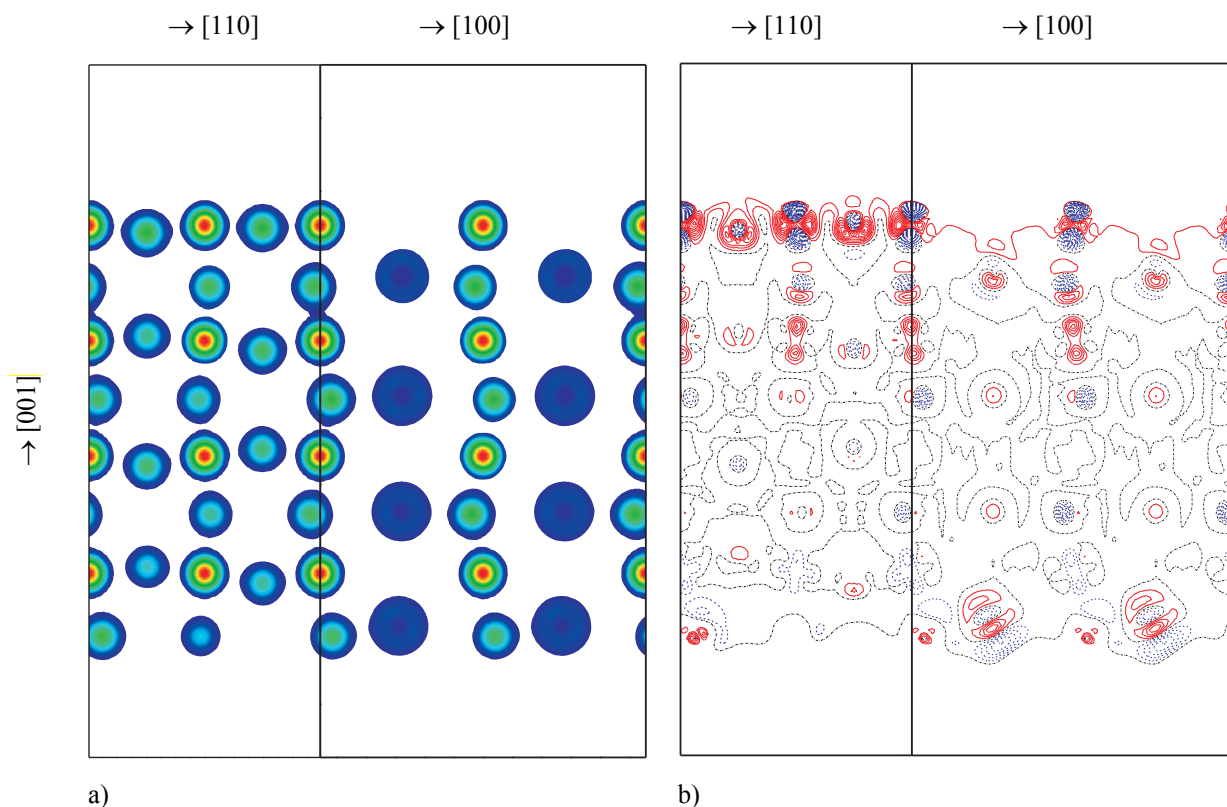


Figure 5.5. Total (a) and difference (b) electron density maps for 8-plane slab. Solid red and dash blue lines represent deficiency and excess of the electron charge, respectively. Density increment is $0.0125 e/\text{\AA}^3$. Dash-dot black line is the zero level. See Figure 4.12 for ions identification.

In order to illustrate the *charge density redistribution* in the symmetric and asymmetric slabs, the difference density maps with respect to the bulk were plotted in Figure 5.4 and Figure 5.5 for the 7- and 8-plane orthorhombic slabs. The total density maps clearly show the zig-zag-type wavy orthorhombic structure of slabs. The difference maps demonstrate, in its turn, that only near-surface metal atoms are visibly perturbed (Mn atoms considerably polarised). In spite of the different stoichiometry of the 7- and 8-plane slabs, this perturbation is very similar for the corresponding terminations of both slabs. Such a character of the charge redistribution is determined mostly by broken chemical bonds rather than by the stoichiometry of the slab.

To shed more light on the electronic density redistribution, the Bader effective charges were calculated for 7- and 8- plane slabs in different magnetic states. The perturbation in the cubic slabs with respect to the bulk values is mostly localized in the first plane for the MnO_2 termination (Table 5.8b) and the first two planes for the LaO termination (Table 5.9b), metal atoms are more affected than O atoms.

Table 5.8 and Table 5.9 presents the charge analysis for two nonstoichiometric slabs (MnO_2 and LaO termination from both sides), also used for the surface energy calculations. In this case, deviations of the total slab charge from zero are equal, but have different signs. This

reflects the fact that these two slabs are complementary and represent seven bulk units when combined together. The atomic charges for 8-plane slabs (Table 5.10), regardless of their magnetic state, are very similar. For the LaO-terminated slab (Table 5.9), the charge of the first two planes is reduced, as for the 8-plane stoichiometric slab (Table 5.10), whereas central planes are almost unperturbed. In the MnO₂-terminated slab (Table 5.8) perturbation is not restricted to the first plane and remains large even in the plane third from the surface – in line with the results for the stoichiometric slab and previous HF calculations [35, 36]. The general conclusion could be drawn that the effective atomic charges depend weakly on the surface relaxation.

A similar analysis was performed for stoichiometric slabs (Table 5.10). The charge of LaO surface is reduced compared to the bulk, which tends to reduce the dipole moment of the slab, according to electrostatic arguments [90]. On the other hand, the charge of the MnO₂ surface practically does not change; moreover, larger perturbations are observed in the deeper, third layer from the surface plane. In general, metal ions (La and Mn) show larger charge changes than O atoms. The calculated charges depend weakly on the slab magnetic states.

Table 5.8. The effective atomic charges and plane charges (in e) for different magnetic states of 7-plane MnO₂-terminated (001) slab (a, c) and their deviations (b, d) from the bulk (Table 4.8 and Table 4.10).

a)												
plane	atom	FM	AAF	CAF	GAF	FM*	atom	FM	AAF	CAF	GAF	FM*
I	Mn	1.67	1.61	1.64	1.63	1.68	O	-1.17	-1.19	-1.18	-1.19	-1.19
II	La	2.09	2.09	2.09	2.09	2.08	O	-1.24	-1.14	-1.19	-1.15	-1.19
III	Mn	1.87	1.87	1.87	1.85	1.79	O	-1.22	-1.22	-1.22	-1.22	-1.21
IV	La	2.15	2.14	2.14	2.14	2.07	O	-1.33	-1.34	-1.35	-1.34	-1.21

b)												
plane	atom	FM	AAF	CAF	GAF	FM*	atom	FM	AAF	CAF	GAF	FM*
I	Mn	-0.18	-0.23	-0.21	-0.22	0.00	O	0.15	0.13	0.14	0.14	0.05
II	La	-0.04	-0.04	-0.04	-0.04	0.01	O	0.09	0.18	0.13	0.17	0.06
III	Mn	0.02	0.02	0.02	0.01	0.11	O	0.10	0.10	0.11	0.11	0.05
IV	La	0.02	0.01	0.01	0.01	0.00	O	-0.01	-0.01	-0.02	-0.02	0.04

c)							d)						
plane		FM	AAF	CAF	GAF	FM*	plane		FM	AAF	CAF	GAF	FM*
I	MnO ₂	-0.68	-0.78	-0.73	-0.75	-0.71	I	MnO ₂	0.12	0.03	0.08	0.05	0.11
II	LaO	0.85	0.95	0.90	0.94	0.89	II	LaO	0.05	0.14	0.09	0.13	0.07
III	MnO ₂	-0.58	-0.57	-0.57	-0.58	-0.61	III	MnO ₂	0.22	0.23	0.24	0.22	0.21
IV	LaO	0.82	0.80	0.80	0.79	0.86	IV	LaO	0.02	0.00	-0.01	-0.01	0.04

* orthorhombic slab

Table 5.9. The same as Table 5.8 for LaO-termination.

a)												
plane	atom	FM	AAF	CAF	GAF	FM*	atom	FM	AAF	CAF	GAF	FM*
I	La	1.98	1.96	1.99	1.99	1.96	O	-1.33	-1.36	-1.36	-1.32	-1.33
II	Mn	1.63	1.71	1.64	1.55	1.56	O	-1.31	-1.31	-1.30	-1.25	-1.27
III	La	2.09	2.09	2.09	2.08	2.06	O	-1.32	-1.37	-1.36	-1.37	-1.28
IV	Mn	1.76	1.79	1.79	1.70	1.64	O	-1.31	-1.31	-1.30	-1.27	-1.26

b)												
plane	atom	FM	AAF	CAF	GAF	FM*	atom	FM	AAF	CAF	GAF	FM*
I	La	-0.15	-0.17	-0.14	-0.14	-0.11	O	-0.01	-0.03	-0.04	0.00	-0.08
II	Mn	-0.21	-0.13	-0.21	-0.30	-0.11	O	0.02	0.01	0.02	0.07	-0.03
III	La	-0.04	-0.04	-0.04	-0.05	-0.01	O	0.01	-0.04	-0.03	-0.05	-0.03
IV	Mn	-0.09	-0.06	-0.05	-0.15	-0.04	O	0.02	0.02	0.03	0.05	-0.01

c)							d)						
plane	FM	AAF	CAF	GAF	FM*	plane	FM	AAF	CAF	GAF	FM*		
I	LaO	0.64	0.60	0.63	0.67	0.64	I	LaO	-0.16	-0.21	-0.17	-0.13	-0.18
II	MnO ₂	-0.99	-0.91	-0.97	-0.95	-0.99	II	MnO ₂	-0.18	-0.10	-0.16	-0.15	-0.16
III	LaO	0.77	0.72	0.73	0.71	0.79	III	LaO	-0.03	-0.08	-0.07	-0.10	-0.03
IV	MnO ₂	-0.85	-0.82	-0.80	-0.85	-0.88	IV	MnO ₂	-0.05	-0.02	0.01	-0.04	-0.05

* orthorhombic slab

Table 5.10. The effective atomic charges (in e) for the stoichiometric 8-plane (001) slab per atom a) and per plane c). Charge deviations from the bulk values (Table 4.8 and Table 4.10) are given in b) and d), respectively.

a)													
	atom	FM	AAF	CAF	GAF	FM*	atom	FM	AAF	CAF	GAF	FM*	
	I	La	2.01	1.99	2.02	2.01	1.97	O	-1.31	-1.35	-1.36	-1.36	-1.32
	II	Mn	1.65	1.74	1.66	1.73	1.59	O	-1.28	-1.29	-1.26	-1.29	-1.26
	III	La	2.08	2.07	2.07	2.08	2.06	O	-1.23	-1.31	-1.18	-1.32	-1.25
	IV	Mn	1.75	1.80	1.71	1.78	1.68	O	-1.26	-1.27	-1.25	-1.25	-1.24
	V	La	2.08	2.07	2.07	2.07	2.07	O	-1.32	-1.29	-1.32	-1.30	-1.24
	VI	Mn	1.77	1.82	1.77	1.80	1.74	O	-1.23	-1.24	-1.23	-1.23	-1.22
	VII	La	2.09	2.07	2.07	2.08	2.09	O	-1.23	-1.26	-1.24	-1.26	-1.19
	VIII	Mn	1.62	1.62	1.61	1.62	1.67	O	-1.21	-1.19	-1.20	-1.21	-1.20

b)													
	atom	FM	AAF	CAF	GAF	FM*	atom	FM	AAF	CAF	GAF	FM*	
	I	La	-0.12	-0.14	-0.12	-0.11	-0.10	O	0.02	-0.03	-0.04	-0.03	-0.07
	II	Mn	-0.20	-0.11	-0.19	-0.12	-0.08	O	0.04	0.04	0.07	0.03	-0.01
	III	La	-0.05	-0.06	-0.06	-0.05	-0.01	O	0.10	0.02	0.14	0.01	0.00
	IV	Mn	-0.10	-0.05	-0.14	-0.06	0.01	O	0.07	0.06	0.07	0.08	0.01
	V	La	-0.05	-0.05	-0.06	-0.06	-0.01	O	0.01	0.03	0.01	0.03	0.01
	VI	Mn	-0.08	-0.03	-0.07	-0.04	0.06	O	0.09	0.09	0.10	0.10	0.03
	VII	La	-0.04	-0.06	-0.06	-0.05	0.02	O	0.10	0.06	0.09	0.06	0.06
	VIII	Mn	-0.23	-0.22	-0.24	-0.22	-0.01	O	0.12	0.13	0.13	0.12	0.04

c)							d)							
	plane	FM	AAF	CAF	GAF	FM*		plane	FM	AAF	CAF	GAF	FM*	
	I	LaO	0.70	0.64	0.65	0.65	0.64	I	LaO	-0.10	-0.17	-0.15	-0.15	-0.18
	II	MnO ₂	-0.92	-0.84	-0.86	-0.86	-0.93	II	MnO ₂	-0.12	-0.03	-0.05	-0.06	-0.11
	III	LaO	0.85	0.76	0.89	0.76	0.81	III	LaO	0.05	-0.04	0.09	-0.04	-0.02
	IV	MnO ₂	-0.77	-0.73	-0.80	-0.71	-0.80	IV	MnO ₂	0.04	0.07	0.01	0.10	0.03
	V	LaO	0.76	0.78	0.75	0.78	0.83	V	LaO	-0.04	-0.02	-0.06	-0.03	0.01
	VI	MnO ₂	-0.69	-0.66	-0.69	-0.65	-0.71	VI	MnO ₂	0.11	0.14	0.12	0.15	0.11
	VII	LaO	0.86	0.81	0.83	0.81	0.90	VII	LaO	0.06	0.01	0.03	0.01	0.08
	VIII	MnO ₂	-0.80	-0.76	-0.79	-0.79	-0.74	VIII	MnO ₂	0.00	0.04	0.02	0.02	0.08

* orthorhombic slab

5.2 The (110) surface

The atomic and electronic structure of the polar (110) LaMnO_3 surface was calculated for the FM configuration. Similarly, both the 8-plane stoichiometric asymmetrical slabs $\text{O}_2/\text{LaMnO}/\dots/\text{LaMnO}$ and two types of 7-plane nonstoichiometric but symmetrical slabs without dipole moments ($\text{O}_2/\text{LaMnO}\dots\text{O}_2$ and $\text{LaMnO}/\text{O}_2\dots/\text{LaMnO}$) were modelled as shown in Table 5.11 and Figure 5.6 and Figure 5.7.

Table 5.11. The plane sequence for the (110) surface modelled using 8-plane (a), 7-plane LaMnO - (b), O_2 - (c), and O - (d) terminated slabs.

a)	b)	c)	d)
LaMnO	LaMnO		
O_2	O_2	O_2	O
LaMnO	LaMnO	LaMnO	LaMnO
O_2	O_2	O_2	O_2
LaMnO	LaMnO	LaMnO	LaMnO
O_2	O_2	O_2	O_2
LaMnO	LaMnO	LaMnO	LaMnO
O_2		O_2	O

half of O ions from nearest surface cells in the zig-zag way, in order to give the surface more degrees of freedom for a further relaxation [86]. In calculations of the surface energy Eq. (5.1) and (5.2) were used.

As follows from Table 5.12, in all three cases, the (110) surface energy is larger than that for the above discussed (001) surface. The same conclusion was drawn in the HF calculations [35]. Second, the *VASP*-calculated cleavage energies for 7- and 8-plane slabs practically coincide. This shows that the dipole moments of slabs play no essential role in the present calculations. Very important is that the surface energy with vacancies is considerably lower than the defectless surface. In other words: the introduction of surface vacancies into the polar (110) surface has a strong *stabilizing effect*. A similar conclusion was drawn earlier for the SrTiO_3 (110) surface [35, 86].

The (110) O_2 -terminated 7-plane slab could be made stoichiometric by removing from both surfaces $\frac{1}{2}$ of oxygen ion, i.e. leaving one O ion instead of the two in the surface unit cell. This procedure is widely used for stabilisation of the polar (110) oxide surfaces, e.g. for SrTiO_3 (110) [91, 92]. In our study, we used 2×1 extended surface unit cell and thus removed

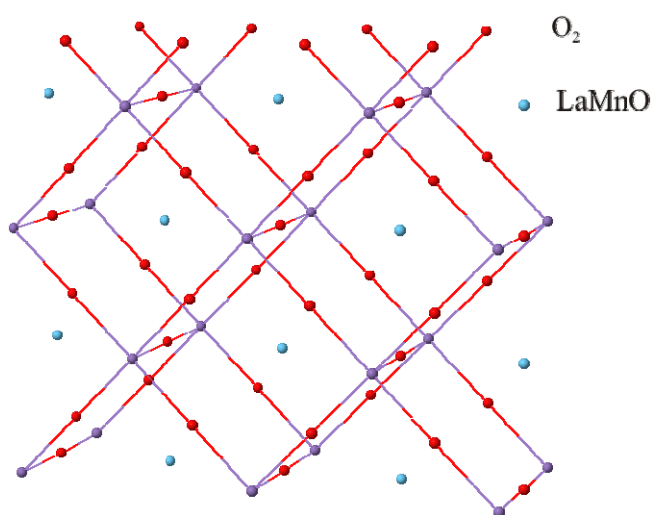


Figure 5.6. Schematic view of the (110) slab with even number of planes (no mirror plane). O_2 planes alternate with LaMnO ones along the direction normal to the surface. Primitive cubic unit cells are the same as those on Figure 4.1b.

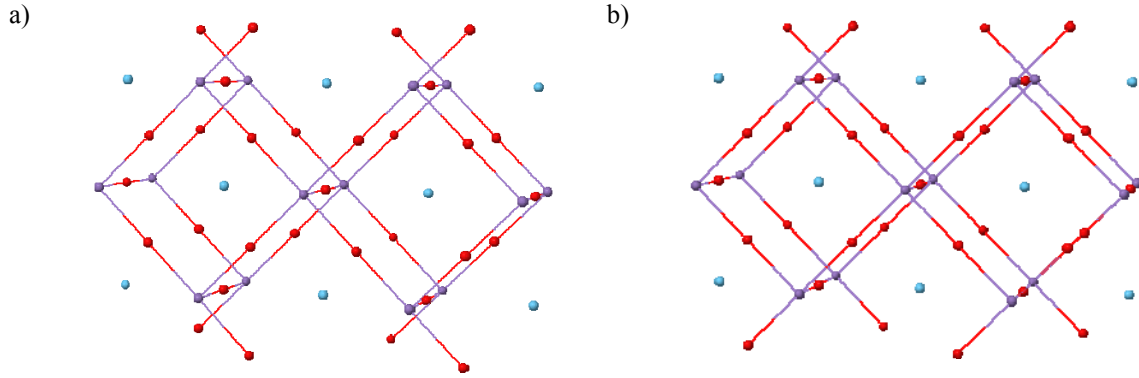


Figure 5.7. The 7-plane (110) O-terminated slab with half-filled surface oxygen planes. Terminating surfaces are symmetric a) and antisymmetric with respect to the mirror LaMnO plane.

Table 5.12. Surface energies of the FM (110) surface (in eV/a_0^2).

slab	cubic		orthorhombic	
	cleavage	relaxed	cleavage	relaxed
7-plane defectless	2.60	1.69	2.70	1.75
7-plane O-vac. symmetric	1.59	0.75	1.68	0.96
7-plane O-vac. antisymmetric	1.60	0.49	1.68	0.76
8-plane defectless	2.59	1.29	2.69	1.80

We have compared the relevant atomic relaxations in Table 5.13 and Table 5.14. Unlike the (001) surface, atoms in O_2 -planes now experience in-plane displacements along the y axis. Additionally, the 8-plane slabs show large surface La displacements inwards the slab center (6-7 % of a_0), whereas Mn and O ions move in the opposite direction. As a result, we predict that this surface has to exhibit very large rumpling. Table 5.13 and Table 5.14 show that atomic displacements are large even in the slab centre. Thus the modelling of the (110) surfaces needs much thicker slabs than those used for (001).

Table 5.13. Atomic displacements (in % of $a_0\sqrt{2}$) along the y and z axes for the defectless 7- and 8-plane slabs. Positive (negative) sign means displacement outwards (inwards) the slab center.

slab		7-plane				8-plane	
termination		LaMnO		O ₂			
atom		Δy	Δz	Δy	Δz	Δy	Δz
La		0.00	-6.43			0.00	-6.10
Mn		0.00	3.36			0.00	3.40
O		0.00	1.98	termination plane		0.00	6.61
O ₂		-0.34	0.25	1.02	-4.98	-1.45	3.26
La		0.00	-0.47	0.00	2.56	0.00	-4.77
Mn		0.00	-0.43	-0.01	2.15	0.00	-0.17
O		0.00	-0.31	0.00	-3.49	0.00	1.13
O ₂		0.00	0.00	0.22	-1.50	-1.23	1.67
La		mirror plane		0.00	0.00	0.00	-5.20
Mn				0.01	0.00	0.00	-1.62
O				0.00	0.00	0.00	1.56
O ₂				mirror plane		-1.53	1.64
La						0.00	-11.17
Mn						0.00	-3.31
O						0.00	1.55
O ₂						-1.32	2.48

Table 5.14. Atomic displacements (in % of $a_0\sqrt{2}$) along the y and z axes for the 7-plane O-terminated slabs with oxygen vacancies placed in symmetrical and antisymmetrical positions (Figure 5.7).

plane	atom	symmetric		antisymmetric	
		Δy	Δz	Δy	Δz
I	O	9.98	-10.26	9.09	-9.32
	O	-9.98	-10.26	-9.08	-9.33
II	La	0.00	0.61	0.00	-0.72
	La	0.00	0.61	0.00	-0.72
	Mn	3.21	1.36	3.50	2.62
	Mn	-3.22	1.36	-3.50	2.62
	O	0.00	-0.59	0.00	1.18
	O	0.00	-0.59	0.00	1.18
III	O	-5.51	10.57	-0.96	3.87
	O	6.20	-9.77	1.55	-4.00
	O	-6.21	-9.76	-1.55	-4.00
	O	5.51	10.57	0.96	3.87
IV	La	0.00	0.00	0.00	0.00
	La	0.00	0.00	0.00	0.00
	Mn	0.01	-0.01	-0.19	0.00
	Mn	0.01	0.01	0.19	0.00
	O	0.00	0.00	0.00	0.00
	O	0.00	0.00	0.00	0.00

Table 5.15 and Table 5.16 demonstrate that the LaMnO-terminated surface is strongly negatively charged with respect to the bulk. The second plane is already close to the bulk. The complementary O₂-terminated surface is positively charged, and deeper perturbed. This effect is observed in both stoichiometric and nonstoichiometric slabs and is thus independent of the surface polarization.

Table 5.15. The effective charges (in e) for the 7-plane (110) slab a) and their deviation from the bulk b).

	LaMnO-terminated				O ₂ -terminated			
	La	Mn	O	plane	La	Mn	O	plane
I	1.72	1.04	-1.25	1.51			-0.93	-1.86
II			-1.30	-2.60	2.15	1.77	-1.11	2.80
III	2.06	1.57	-1.27	2.35			-1.16	-2.32
IV			-1.26	-2.53	2.13	1.79	-1.19	2.73
b)								
I	-0.41	-0.80	0.07	-1.14			0.40	0.79
II			0.02	0.05	0.02	-0.08	0.21	0.15
III	-0.07	-0.28	0.05	-0.30			0.17	0.33
IV			0.06	0.12	0.00	-0.06	0.14	0.08

Table 5.16. Atomic and planar charges (in e) for the 8- a) and 7-plane with oxygen vacancies b), c) and their respective deviations from the bulk values d), e), f).

a)	ideal surface				b)				c)			
	La	Mn	O	plane	La	Mn	O	plane	La	Mn	O	plane
I	1.87	1.25	-1.30	1.83								
II			-1.30	-2.60			-1.21	-1.21			-1.21	-1.21
III	2.01	1.65	-1.22	2.44	2.07	1.58	-1.27	2.38	2.07	1.62	-1.27	2.42
IV			-1.25	-2.50			-1.22	-2.45			-1.23	-2.46
V	2.02	1.72	-1.17	2.56	2.09	1.80	-1.35	2.54	2.06	1.78	-1.33	2.51
VI			-1.20	-2.39			-1.22	-2.44			-1.22	-2.45
VII	2.14	1.78	-1.10	2.82	2.07	1.58	-1.27	2.39	2.07	1.62	-1.27	2.41
VIII			-1.07	-2.15			-1.21	-1.21			-1.21	-1.21
d)												
	ideal surface				e)				f)			
	La	Mn	O	plane	La	Mn	O	plane	La	Mn	O	plane
I	-0.25	-0.59	0.03	-0.82								
II			0.02	0.05			0.12	0.12			0.11	0.11
III	-0.12	-0.20	0.11	-0.22	-0.06	-0.26	0.05	-0.27	-0.06	-0.22	0.05	-0.23
IV			0.08	0.15			0.10	0.20			0.09	0.19
V	-0.11	-0.13	0.15	-0.09	-0.04	-0.04	-0.02	-0.11	-0.07	-0.07	0.00	-0.14
VI			0.13	0.26			0.10	0.21			0.10	0.20
VII	0.01	-0.06	0.22	0.17	-0.06	-0.26	0.06	-0.26	-0.06	-0.23	0.05	-0.24
VIII			0.25	0.51			0.12	0.12			0.11	0.11

6 Oxygen Adsorption on the LaMnO_3 (001) MnO_2 -terminated Surface and Oxygen Vacancy

In the SOFC oxygen gets adsorbed on the LaMnO_3 cathode surface and then moves towards the electrolyte (Figure 1.2). In this Chapter we study the possibility of *molecular* as well as *dissociative* oxygen adsorption on SOFC cathode. The most energetically favourable position for the atomic O adsorption is found and used for the calculation of the molecular adsorption. Adsorbed oxygen atom can migrate towards the electrolyte either along the cathode surface, or can penetrate through the cathode. There are two possible diffusion paths on the MnO_2 -terminated surface: along [100] or [110] directions. For the purpose of finding out which one is more preferable, we estimate below the energy barriers between the different adsorption sites. The final step of oxygen interaction with the SOFC cathode is the penetration of the adsorbed O atoms into the electrode, when they encounter oxygen vacancies. In order to understand how adsorbed O migration and surface vacancies control this process, we calculated the migration energy for surface and bulk oxygen vacancies.

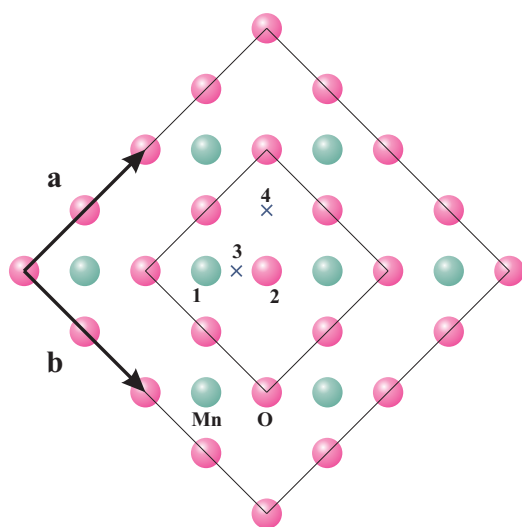


Figure 6.1. $2a \times 2b$ surface cell used for the adsorption modelling. Possible adsorption sites at the MnO_2 -terminated (001) surface: 1 - atop Mn atom, 2 - atop O atom, 3 - “bridge” position, 4 - “hollow” position.

Surface modelling was performed by placing a defect (O adsorbate or vacancy) on both sides of the MnO -terminated 7-plane nonstoichiometric ($\text{La}_{0.75}\text{Mn}_2\text{O}_{2.75}$) symmetrical slab (Table 5.1b). The surface unit cell has extensions of $2a \times 2b$ (Figure 6.1), so the surface defect concentration is 12.5 %. Since our calculations correspond to 0 K, we used the relevant low-temperature *orthorhombic* unit cell with on-plane lattice constants $a = 5.56 \text{ \AA}$, $b = 5.61 \text{ \AA}$ optimized for the bulk (Table 4.6).

6.1 Oxygen adsorption

The most preferable O adsorption sites are usually atop the surface atoms. Sometimes it could be also an unoccupied high-symmetry point at the surface. In the present study the possible adsorption sites were chosen similarly to the study in Ref.[30], where oxygen adsorption was modelled on the isostructural SrTiO_3 surface. Namely, these adsorption sites are associated with the Mn and O ions and with the so-called “hollow position” - the most

distant one to any of the surface atoms (Figure 6.1). In all cases the adatom was placed atop the corresponding atom/point on the surface and then all atoms were allowed to relax to the energetically most favourable positions in the vicinity of the initial point. The actual adsorption positions will be shown below along with other details.

6.1.1 Atomic O adsorption

The oxygen atom adsorption energies $E_{\text{ads}}^{(\text{at})}$ were calculated with respect to free oxygen atoms:

$$E_{\text{ads}}^{(\text{at})}(\text{O}) = -\frac{1}{2} [E_{\text{slab}}^{(\text{ads})}(\text{O}) - E_{\text{slab}} - 2 E^{(\text{O})}], \quad (6.1)$$

and with respect to free oxygen molecule:

$$E_{\text{ads}}^{(\text{m})}(\text{O}) = -\frac{1}{2} [E_{\text{slab}}^{(\text{ads})}(\text{O}) - E_{\text{slab}} - E^{(\text{O}_2)}], \quad (6.2)$$

where $E_{\text{slab}}^{(\text{ads})}$ is the total energy of a fully relaxed slab with two-sided adsorbate (O or O₂), E_{slab} is the same for a pure slab, $E^{(\text{O})}$ is the energy of isolated oxygen atom in the ground triplet state, and $E^{(\text{O}_2)}$ is the total energy of isolated oxygen molecule in the triplet state. The prefactors $\frac{1}{2}$ before brackets and 2 before $E^{(\text{O})}$ appear since the interface is modeled by a

Table 6.1. O atom adsorption energies (in eV).

Energy, eV	Adsorption site		
	Mn	O	h.p.
$E_{\text{ads}}^{(\text{a})}$	-4.02	-2.41	-0.59
$E_{\text{ads}}^{(\text{m})}$	-1.07	0.54	2.36

substrate slab with two equivalent surfaces and both O_{ads} atoms and (O₂)_{ads} molecule symmetrically positioned on both sides of the slab. The molecular adsorption energy was calculated in a similar way. The difference of $E_{\text{ads}}^{(\text{at})}(\text{O})$ and $E_{\text{ads}}^{(\text{m})}(\text{O})$ equals

to the O₂ molecule binding energy.

6.1.1.1 Atop Mn atom

Table 6.1 shows a strong preference for O atom adsorption over the *surface Mn* ion, unlike the *bridge position* between Ti and O ions found for the isostructural SrTiO₃ (Figure 1.4a). The difference between LaMnO₃ and SrTiO₃ is in line with the pronounced oxidizability of Mn³⁺ (in contrast to Ti⁴⁺); note that the top of the valence band in LaMnO₃ is largely due to Mn *d*-orbitals (Figure 4.7) whereas the O *p*-orbitals generate the valence band top in SrTiO₃. The electron charge of 0.62 *e* is transferred to the adsorbed O atom from nearest surface ions (0.18 *e* from the nearest Mn, 0.16 *e* from four nearest O ions and the rest 0.28 *e* from next-nearest ions). As a result of O adsorption, the spin momentum of Mn ion is strongly reduced. The test calculations performed for the high-temperature *cubic* phase (*T* > 750 K) give qualitatively similar results. In particular, the adsorption energy atop the Mn ion is 4.14 eV, about 3% larger than in the orthorhombic phase. Due to the symmetry lowering of the slab during geometry relaxation, adsorption energies for other sites are incomparable with

those for orthorhombic phase. The comparison of nonstoichiometric 7-plane and stoichiometric 8-plane slabs shows small adsorption energy difference (6%).

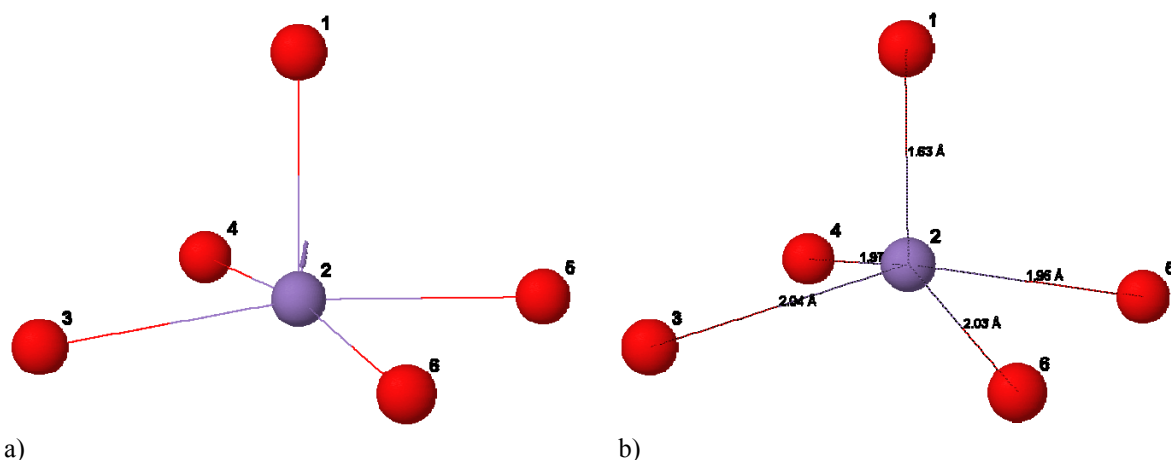


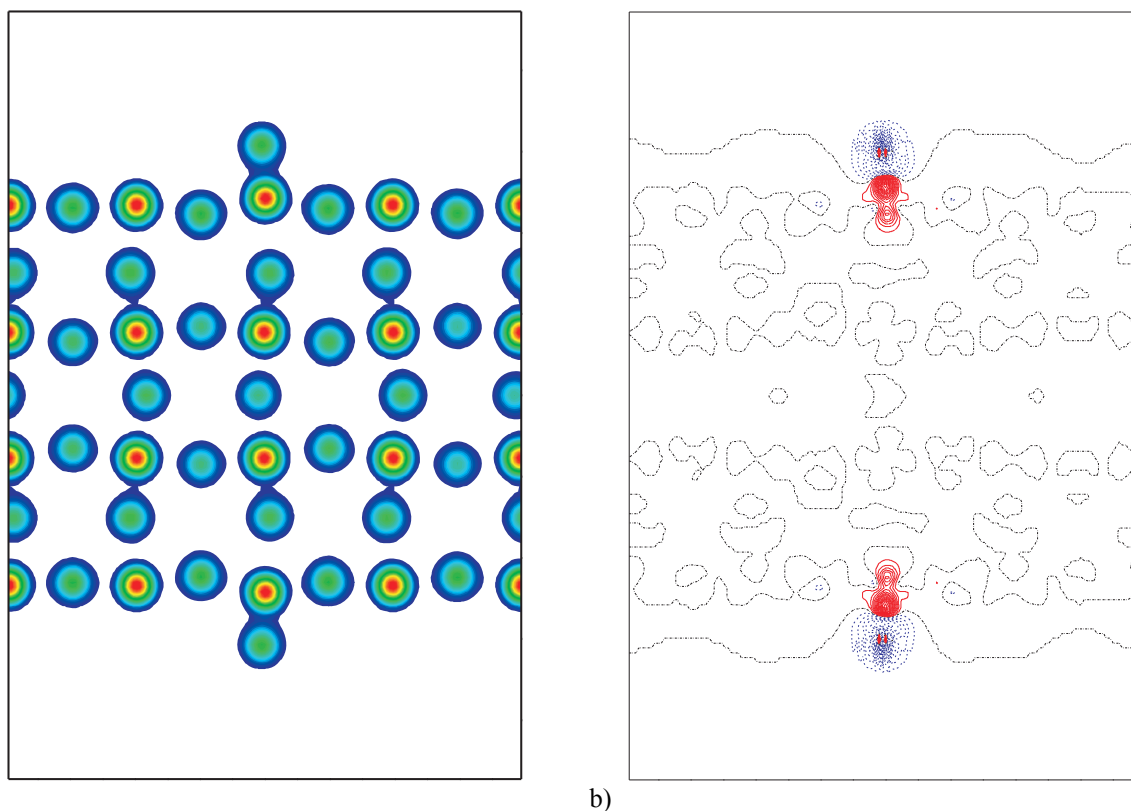
Figure 6.2. Atomic oxygen adsorption on Mn atom a) Arrows show displacements of the surface atoms from the regular positions under the influence of the adsorbed oxygen atom, b) relaxed geometry. Numbering of atoms is according to Table 6.2.

Mn ion is strongly pulled by the adatom out of the surface by 0.22 Å (Figure 6.2a) whereas surface oxygen atoms are slightly (0.03-0.06 Å) pushed down into the slab.

Table 6.2. O atom atop Mn. Atomic displacements d (in Å), effective charges q (in e), charges deviation from the bare surface Δq (in e), magnetic moments M (in μ_B).

N	type	d	q	Δq	M
1	O	NA	-0.62		0.14
2	Mn	0.22	1.85	0.17	2.20
3	O	0.03	-1.14	0.06	0.03
4	O	0.06	-1.12	0.08	0.06
5	O	0.05	-1.11	0.09	0.06
6	O	0.03	-1.15	0.04	0.03

The analysis of the electron density redistribution (Figure 6.3b) confirms that the charge transfer from the surface Mn ion to the O atom is quite localised.



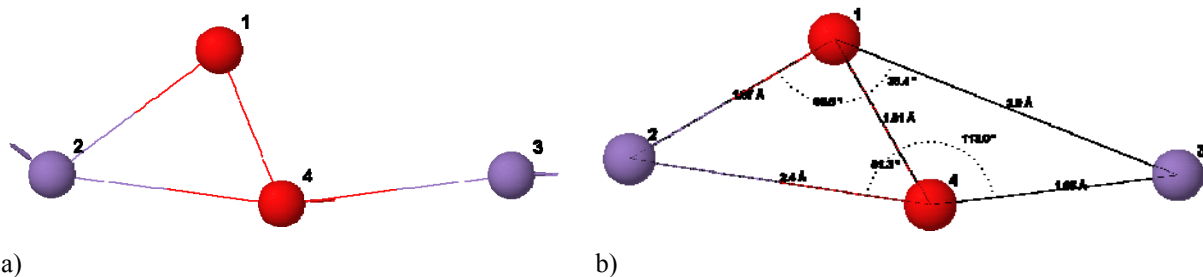
a) b)
 Figure 6.3. Total (a) and difference (b) electron density maps of O atom atop Mn, on both sides of the slab. The difference map (b) was obtained by subtracting the sum of the densities of the adsorbent and the adsorbate from the total density (a). Mn ions have a red spot at the center on the total density map. Solid (red in colour) and dashed (blue in colour) lines correspond to the deficiency and excess in electronic density, respectively. Dash-dot black line is the zero level. Density increment $0.02 e/\text{\AA}^3$.

6.1.1.2 “Bridge” position

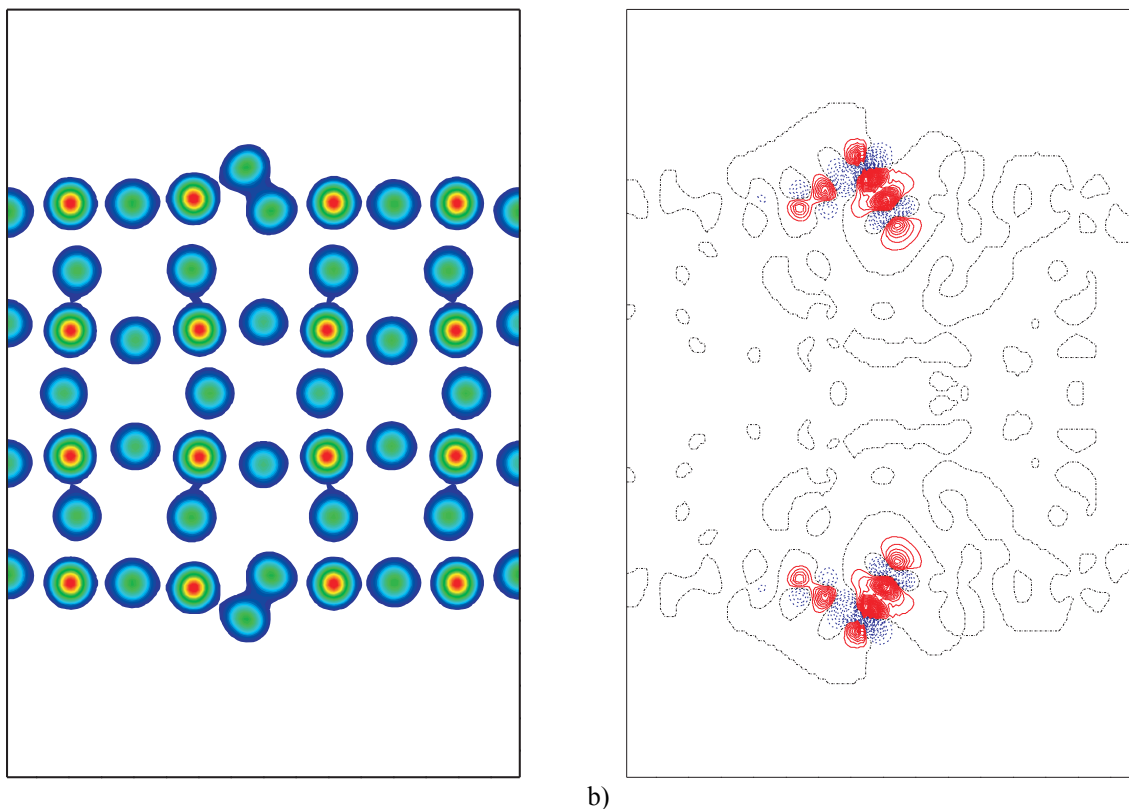
The adsorption position right atop the surface oxygen ion appears to be unstable. The O adatom creates a *tilted* O_2 *quasi-molecule* with the regular oxygen atom on the surface (Figure 6.5), sharing with it the space between two Mn ions, what results in the strong atomic displacements shown in Figure 6.4a. The stable adsorption position near the surface O ion is shown in Figure 6.4b. This is identical to the position found to be energetically most favourable for the SrTiO_3 (001) surface [30]. For LaMnO_3 , this configuration turns out to be energetically less favourable. In this case the adsorbed O atom receives $0.48 e$ from the nearest surface O ion. Keeping in mind that the effective charges in LMO bulk and on the surface are considerably reduced due to the covalent component in the Mn-O chemical bonding as compared to the nominal charges (Table 5.8), this configuration could be treated as formation of a kind of O_2^{2-} *peroxo-molecule* [37] tilted by $\sim 50^\circ$ towards nearest Mn ion (Figure 6.4b).

Table 6.3. Adsorbed O atom atop O surface ion. Atomic displacements d (in Å), effective charges q (in e), charges deviation Δq (in e), magnetic moments M (in μ_B).

N	type	d	q	Δq	M
1	O	NA	-0.48	0.06	
2	Mn	0.22	1.65	-0.02	3.61
3	Mn	0.19	1.66	-0.02	3.73
4	O	0.23	-0.71	0.48	0.04



a) b)
Figure 6.4. The same as in Figure 6.2 for O atom atop surface O atom. Numbering of atoms according to Table 6.3.



a) b)
Figure 6.5. The same as in Figure 6.3 for O atom adsorbed atop surface O atom.

6.1.1.3 “Hollow” position

This stable position shows a very weak bonding between the adsorbate and the adsorbent. The adatom is at least 3.1 Å away from the nearest surface oxygen atoms. There is no chemical bonding between the adsorbent and the adsorbate.

Table 6.4. O atom adsorption atop the hollow position. Atomic displacements d (in Å), effective charges q (in e), charges deviation Δq (in e), magnetic moments M (in μ_B).

N	type	d	q	Δq	M
1	O	NA	-0.32		1.67
2	O	0.03	-1.17	0.03	0.07
3	O	0.04	-1.16	0.03	0.10
4	O	0.04	-1.15	0.04	0.10
5	O	0.04	-1.17	0.02	0.06

The calculated O adsorption energies with respect to an O atom and a free molecule, $E_{\text{ads}}^{(m)}$, Eq. (6.2), are collected in Table 6.1. The negative value is obtained only for O atom atop the Mn ion, where the energy gain due to adsorption of two O atoms is larger than the O₂ molecule dissociation energy. (Despite the fact that our calculations overestimate the dissociation energy of an O₂ molecule -5.9 eV vs experimental 5.12 eV [93] – this does not affect our conclusions.) Based on these results, the adsorbed O atom migration could occur along the [110] direction with the saddle point atop the O surface ion and the activation energy of at least 1.6 eV.

For the test calculation we checked how the results depend on the oxygen PAW potential (Table 3.1). For the standard oxygen potential with the plane wave basis set cutoff energy of 400 eV the adsorption energy has changed by less than 0.2 meV.

6.1.2 Molecular O adsorption

The position atop the Mn ion, chosen as the most energetically favourable (Table 6.5) during the *mapping process*, was used for adsorption study of a neutral oxygen *molecule* on the surface. The geometry optimization was performed in two steps: first, the molecule was oriented in two different ways - either perpendicular or parallel to the surface and allowed to relax and tilt (a), then the positions of the surface atoms were optimized too (b).

Table 6.5. Adsorption energies E_{ads} (in eV) for oxygen molecule.

orientation	tilted	horizontal	
atop	Mn	Mn	O
E_{ads}	-1.13	-0.89	-0.29

6.1.2.1 Tilted orientation

The molecule binding energy for a tilted adsorption is 1.13 eV, by 0.24 eV larger than for horizontal orientation. The total charge on the adsorbed molecule is -0.42 e , with a bond length of 1.36 Å. (The bond length 1.3 Å for a free O₂ molecule calculated for the cutoff energy and other parameters used in this study are slightly larger than experimental value of 1.21 Å [94]. The adsorbed molecule could be considered as a kind of the *superoxo-radical* O₂⁻ [37].

In a comparison with atomic O adsorption, the Mn-O distance is slightly (0.2 Å) larger (Table 6.2 and Table 6.6). The geometry of the surface remains practically unperturbed (Figure 6.6a). The molecule got tilted by ~60° from the perpendicular to the surface (Figure

6.6a). The same process was modelled on the stoichiometric 8-plane slab (Figure 6.8). The adsorption energy in the latter case is larger by 0.1 eV. As one can see in the electron density map, there is no visible difference between the molecules adsorbed on the 7- and 8-plane slabs. Moreover, the effective charge analysis confirms that for the 7-plane LMO slab stoichiometry has a little to none influence on the surface phenomena, what is in line with the conclusions made in Chapter 5.1 (7- vs. 8-plane slab).

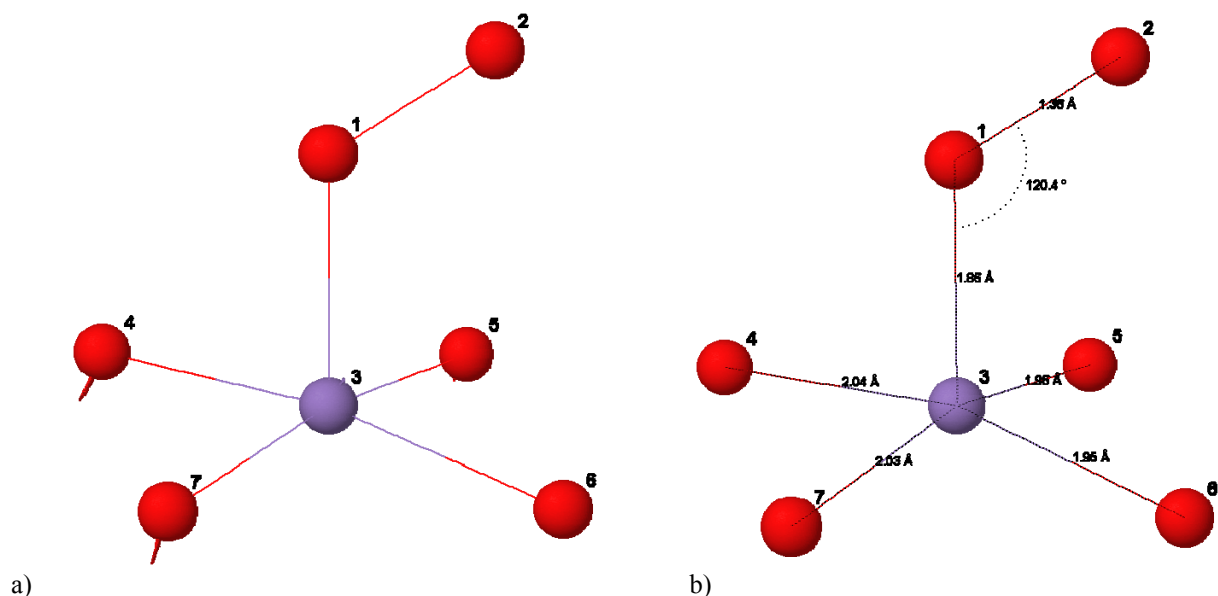
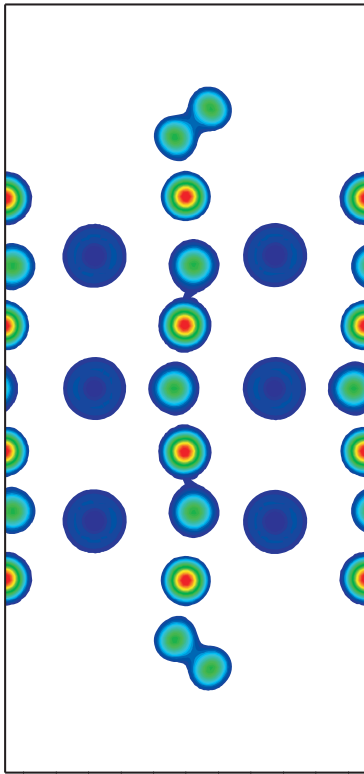


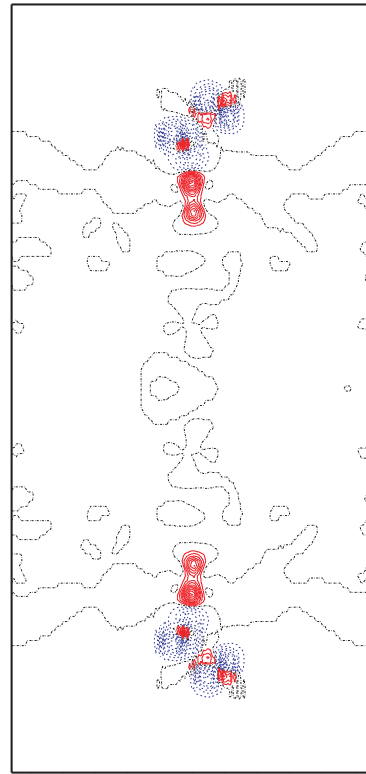
Figure 6.6. Tilted oxygen molecule atop of Mn ion. Displacements (a) and geometry after the relaxation (b). Numbering of atoms according to Table 6.6.

Table 6.6. Vertically oriented O molecule atop Mn ion. Atomic displacements d (in Å), effective charges q (in e), charges deviation Δq (in e), magnetic moments M (in μ_B). Values for the 8-plane slab are given in brackets.

N	type	d	q	Δq	M
1	O	NA	-0.29 (-0.33)		-0.42
2	O	NA	-0.13 (-0.14)		-0.66
3	Mn	0.05	1.78 (1.78)	0.11	3.12
4	O	0.08	-1.17	0.02	0.06
5	O	0.04	-1.13	0.06	0.10
6	O	0.04	-1.13	0.07	0.11
7	O	0.07	-1.18	0.01	0.05

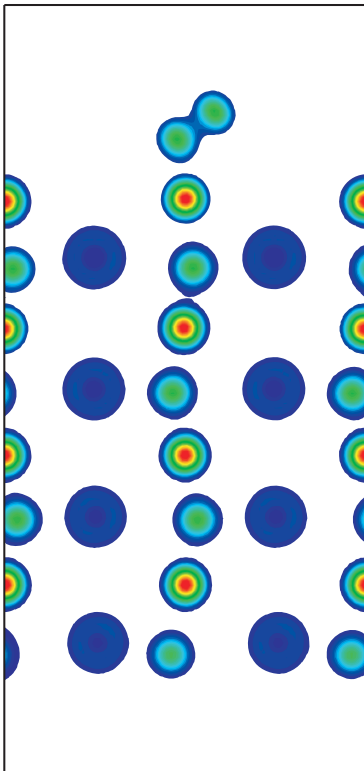


a)

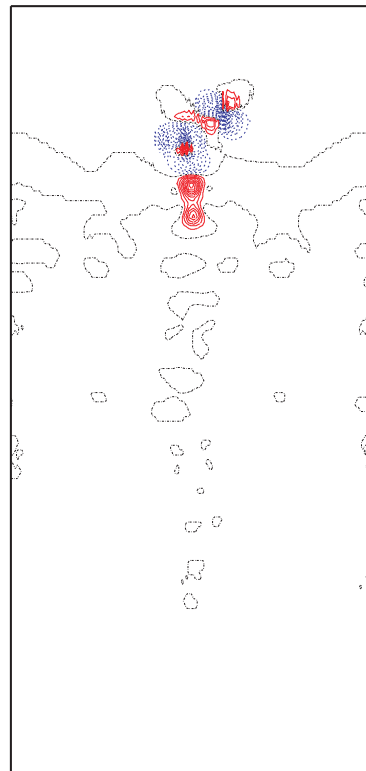


b)

Figure 6.7. Total (a) and difference (b) electron density maps of the tilted oxygen molecule on 7-plane slab.



a)



b)

Figure 6.8. The same as in Figure 6.7 for the 8-plane slab.

6.1.2.2 Horizontal orientation

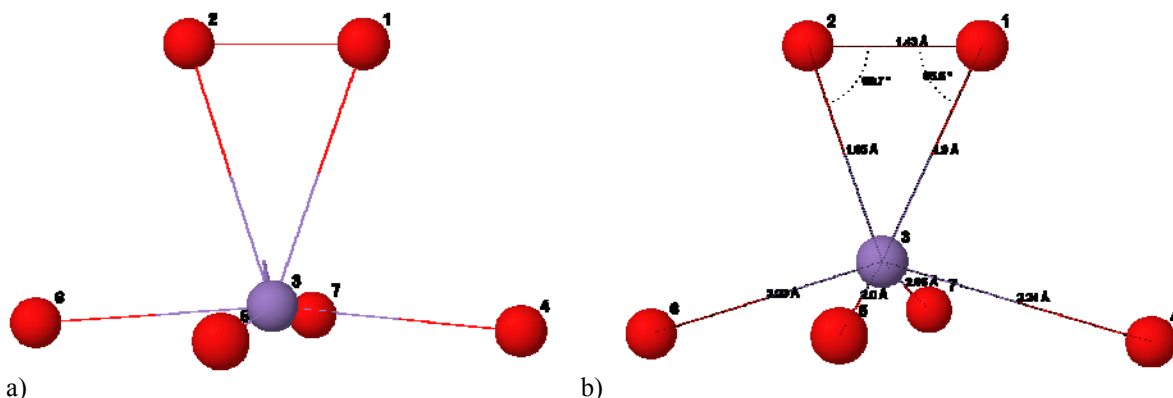


Figure 6.9. The same as in Figure 6.6 for horizontally oriented oxygen molecule.

In the relaxed state adsorbed molecule is almost perfectly oriented along the [110] direction (Figure 6.9). The Mn O distance is about 1.9 Å, what coincides with that for tilted molecule. However, the total charge of the molecule is larger, $-0.6 e$, the bond length increases up to 1.42 Å and it is closer to that of the peroxy-radical O_2^{2-} .

Table 6.7. Horizontally oriented O molecule atop of Mn ion. Atomic displacements d (in Å), effective charges q (in e), charges deviation Δq (in e), magnetic moments M (in μ_B). Values for the 8-plane slab are given in brackets.

N	type	d	q	Δq	M
1	O	NA	-0.30		-0.17
2	O	NA	-0.30		-0.18
3	Mn	0.37	1.77	0.10	3.05
4	O	0.12	-1.15	0.04	0.06
5	O	0.05	-1.14	0.05	0.07
6	O	0.09	-1.13	0.06	0.08
7	O	0.07	-1.17	0.03	0.04

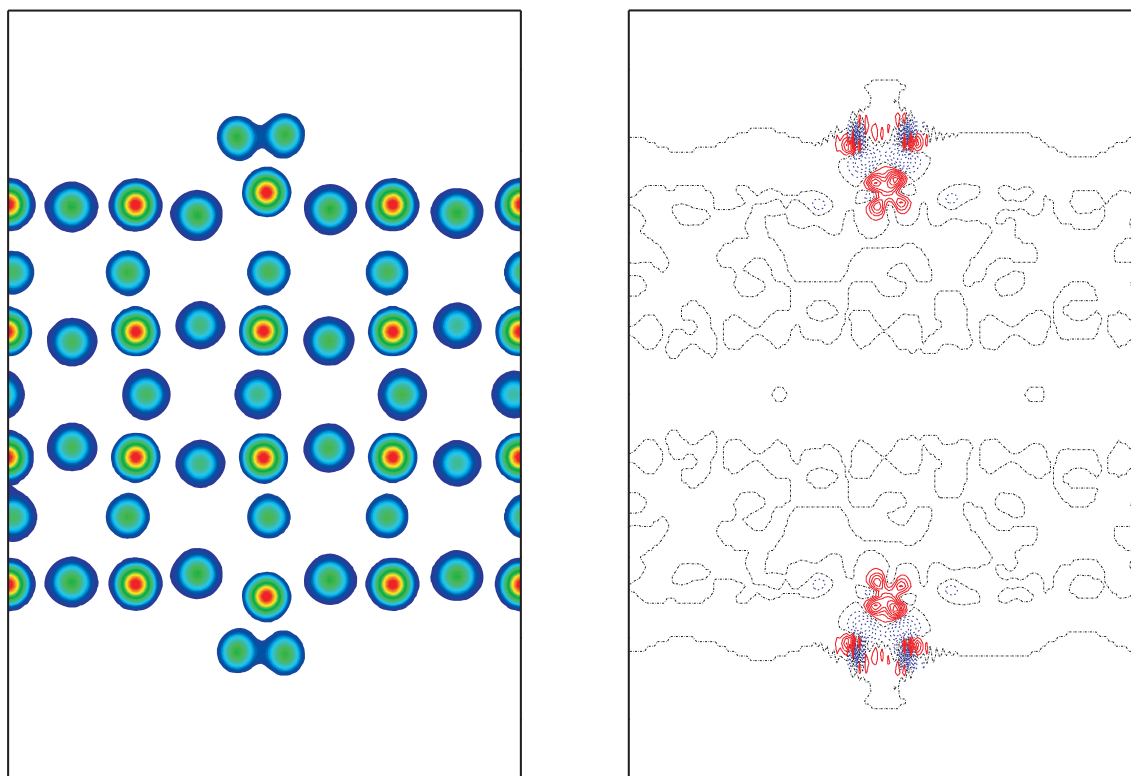


Figure 6.10. Total (a) and difference (b) electron density maps of horizontally oriented oxygen molecule.

In both cases (tilted and horizontal) we observe chemisorption (unlike a weak physical adsorption of O₂ on SrTiO₃ (001) surface [30]). A comparison of atomic and molecular adsorption energies indicates that $2E_{\text{ads}}^{(m)}(\text{O}) > E_{\text{ads}}^{(m)}(\text{O}_2)$ for the most favourable adsorption site atop the Mn ion. This means that the *dissociative* molecular adsorption is favourable even on the defectless LaMnO₃ surface – in contrast to SrTiO₃ [30].

Assuming that the adsorbed oxygen molecule could diffuse on the surface, an additional configuration was tested – horizontal, atop the O surface ion (Figure 6.11). Unlike the tilted state, the horizontally oriented molecule is very weakly bonded to the surface, what can significantly ease the diffusion. Since the calculated configuration is energetically stable, the diffusion reaction energy is predicted to be ~ 0.6 eV.

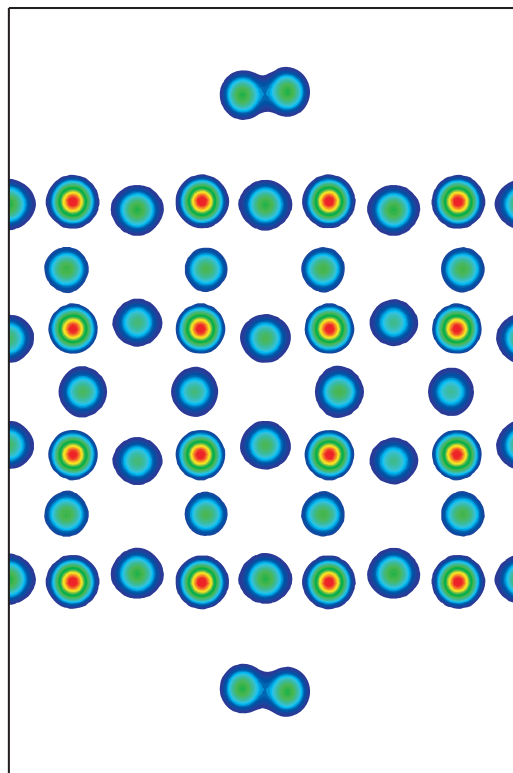


Figure 6.11. Total electron density map of horizontally oriented oxygen molecule atop the surface O atom.

6.2 Oxygen vacancies in the bulk and on the the MnO₂-terminated surface

Since the adsorbed oxygen atoms turned out to be strongly bound to the surface Mn ions (1.6 eV) and thus are quite immobile, penetration of these O atoms into the first plane of a fuel cell cathode can occur predominantly upon their encounter with the mobile surface oxygen vacancies. To this end, we calculated equilibrium and saddle points for oxygen vacancies in the bulk and on the MnO₂-terminated surface.

6.2.1 Surface vacancy

Two pairs of nearest Mn and La ions are strongly displaced from the vacancy (ca. 0.2 Å) whereas the two nearest O ions towards the vacancy (0.32 Å) Figure 6.12 and Table 6.9. The negative charge of the missing O ions is spread over the nearest ions, mostly Mn (Figure 6.13b, Table 6.9). The calculated surface vacancy migration energy is 0.67 eV (Table 6.8). The key point is

Table 6.8. Oxygen vacancy on the surface: unrelaxed and relaxed formation energies as well as diffusion barrier (in eV).

E_{urx}	E_{rx}	E_{diff}
7.33	6.23	0.67

that the predicted vacancy mobility is much higher than that of the adsorbed O atoms and comparable with that of the adsorbed O₂ molecule. Thus vacancy migration along the cathode surface can play an essential role in fast O transport to the electrolyte.

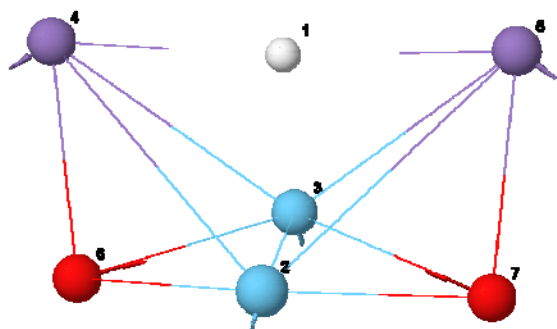
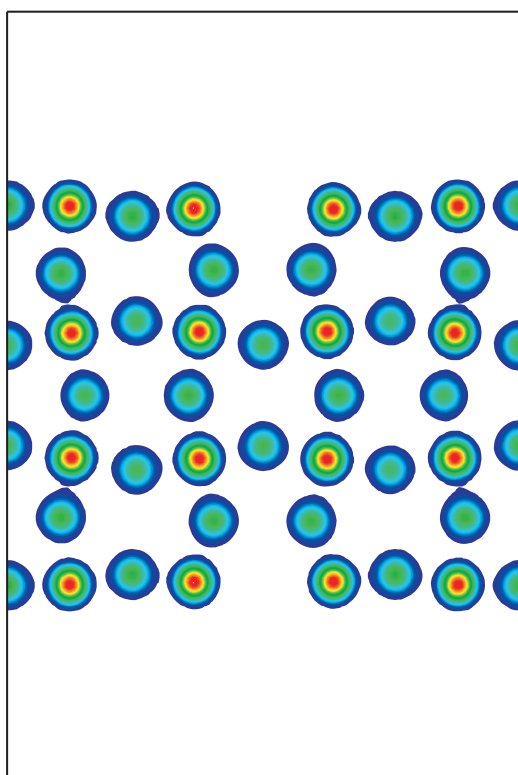


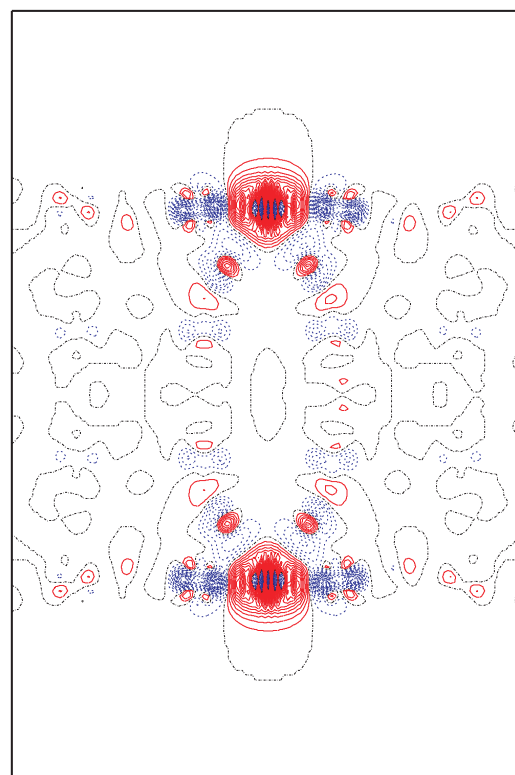
Figure 6.12. Atomic displacements around the oxygen vacancy on the (001) surface. Mn atoms 4, 5 lie in the surface plane. Numbering according to Table 6.9.

Table 6.9. Oxygen vacancy on the surface: atomic displacements d (in Å) and charge deviations Δq (in e).

No.	atom	d	Δq
1	V _O ^x		
2	La	0.17	-0.01
3	La	0.22	0.00
4	Mn	0.22	-0.21
5	Mn	0.19	-0.20
6	O	0.32	-0.03
7	O	0.32	-0.02



a)



b)

Figure 6.13. Total (a) and difference (b) electron density maps. The difference map (b) was obtained by subtracting the density of the perfect slab and adding the density of an isolated atom (at the vacancy site) from the total density (a). See Figure 6.3 for ions identification.

6.2.2 Bulk O vacancy

There are two sets of symmetrically non-equivalent oxygen atoms in the LaMnO_3 bulk: O1 in the LaO (001) plane and O2 in the MnO_2 (001) plane (Figure 6.14). The two corresponding types of oxygen vacancies were compared in this study. Their formation and relaxation energies are practically the same (Table 6.10), thus the electronic properties (Table 6.11) are discussed below only for the O2 vacancy. The oxygen atom can diffuse between two equivalent and two non-equivalent positions along the [100] and [111] direction, respectively (Figure 6.14). These diffusion energies differ by 0.15 eV (Table 6.10). These energies are close to the value that is experimentally observed in SrTiO_3 (0.86 eV [95]) and exceed considerably that for the surface diffusion (0.67 eV) discussed above. The reduction of the surface migration energy compared to that of the bulk was predicted by us also for SrTiO_3 [94].

In contrast to the surface vacancy (Table 6.9), atomic displacements around the vacancy in the bulk are much smaller (Table 6.11). Also the direction of the displacement of the two nearest Mn ions is opposite, hence it is directed inwards. The electron charge redistribution is qualitatively the same as on the surface: the negative charge of the missing O ion is mostly divided between the nearest Mn ions (Table 6.11, Figure 6.16).

Table 6.10. Unrelaxed and relaxed oxygen vacancy formation energies (in eV). Diffusion barriers along the [100] and [111] directions.

vacancy type	E_{urx}	E_{rx}	E_{diff}	diffusion type
O1	7.91	7.64	1.10	(O1→O2)
O2	7.93	7.64	0.95	(O2→O2)

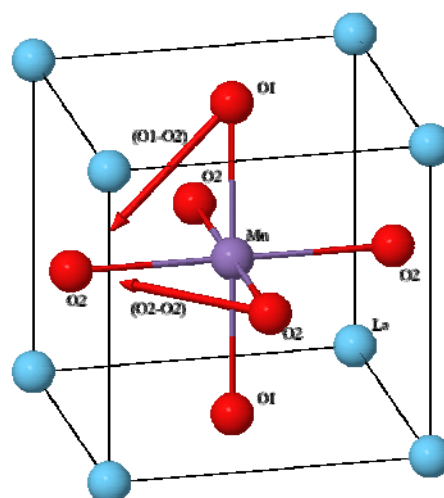


Figure 6.14. Two sets of symmetrically non-equivalent oxygen atoms: polar (O1) in the LaO (001) plane and equatorial (O2) in the MnO_2 (001) plane in the orthorhombic LaMnO_3 bulk. Oxygen vacancy migration can occur along two directions (shown by arrows).

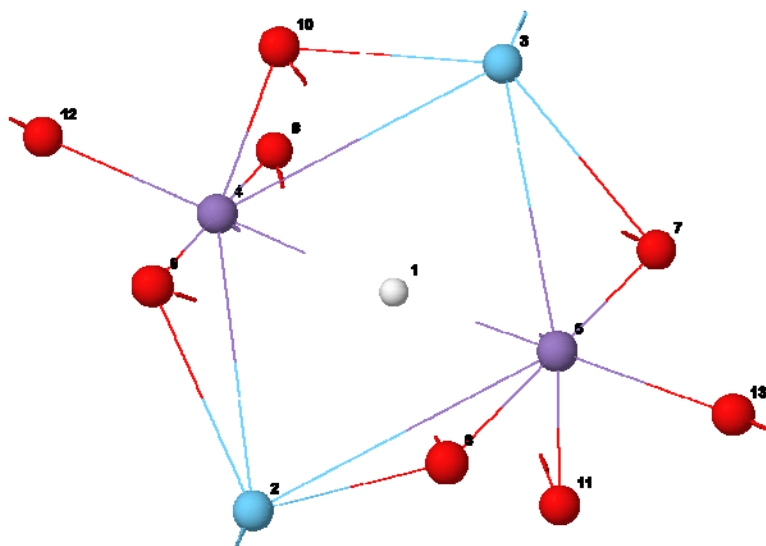


Table 6.11. Oxygen vacancy in the bulk: atomic displacements d (in Å) and charges deviation Δq (in e).

No.	atom	d , Å	Δq , e
1	V_O^x		
2	La	0.08	-0.05
3	La	0.12	-0.05
4	Mn	0.06	-0.29
5	Mn	0.05	-0.36
6	O2	0.10	-0.04
7	O2	0.09	-0.02
8	O2	0.09	-0.01
9	O2	0.09	0.00
10	O1	0.10	-0.05
11	O1	0.12	-0.01
12	O2	0.08	0.00
13	O2	0.09	0.02

Figure 6.15. Displacements of atoms from their regular positions, around the oxygen vacancy of type O2 in the bulk. Numbering according to Table 6.11.

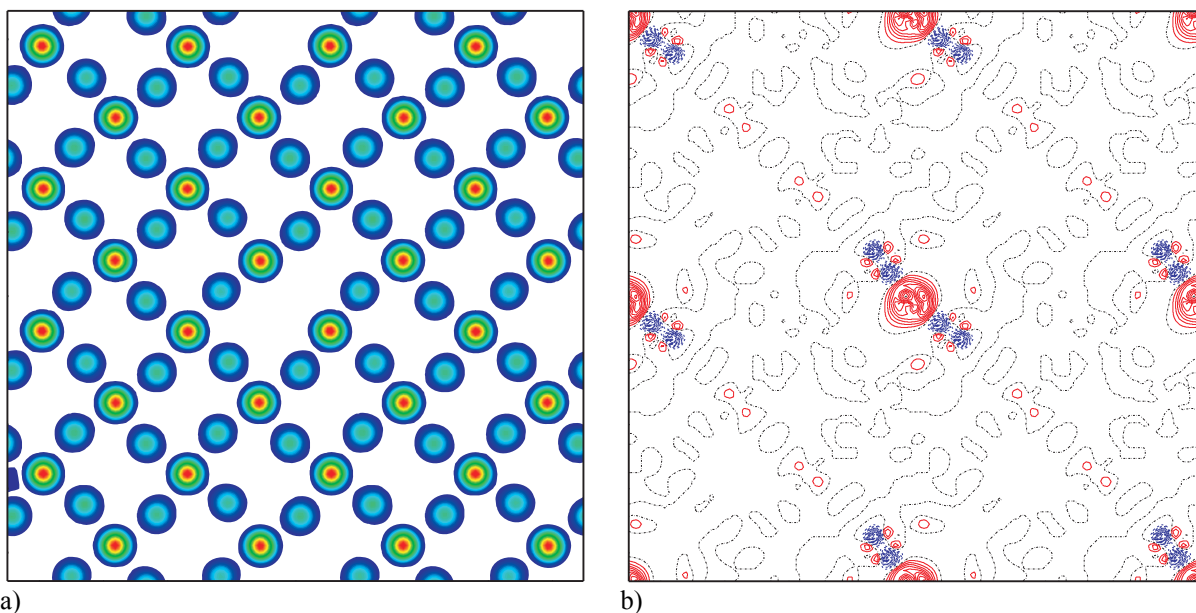


Figure 6.16. Total (a) and difference (b) electron density maps of the oxygen vacancy of O2 type in the bulk. See Figure 6.3 for ions identification.

The vacancy formation energy in the bulk is larger by 1.4 eV than on the surface (Table 6.8 and Table 6.10). This means that strong vacancy segregation towards the surface is expected. This is caused, in particular, by large difference in the relaxation energies in the bulk and on the surface (1.1 eV vs. 0.3 eV).

7 Conclusions

In order to model the elementary *processes* at the Solid Oxide Fuel Cell (SOFC) cathodes on the atomic level we have chosen the Generalised Gradient Approximation (GGA) method within the Density Functional Theory (DFT) as implemented into the *VASP* computer code. One of the main reasons to choose this code is its powerful structure optimization algorithm. As we have demonstrated here, despite certain flaws of the DFT method, it is possible to obtain reasonable structural and energetic parameters for such strongly correlated materials as LaMnO_3 (e.g. surface relaxation, adsorption, defect formation, migration energies).

As a further step, we checked the reliability of this computational method. A series of calculations was performed on the *bulk* as well as on the *bare surfaces* of different orientations. For the Projector-augmented wave (PAW) Perdew-Wang 91 and Perdew-Burke-Ernzerhof GGA potentials (Table 3.1) the standard deviation (RMSD) of the optimized *lattice constants* with respect to the experimental values (Table 3.2) does not exceed 0.08 \AA , unless the “hard” oxygen potential is used. In the latter case the deviation is slightly larger ($0.11\text{-}0.14 \text{ \AA}$). In contrast to the just mentioned PAW potentials, the ultra-soft Vanderbilt (US) Ceperley-Alder pseudopotentials reproduce the lattice constants less accurately (RMSD = $0.23\text{-}0.44 \text{ \AA}$).

We carefully studied, how the calculated *cohesive energy* and lattice parameters depend on the LaMnO_3 *magnetic ordering* – ferromagnetic (FM), three antiferromagnetic (A-, C-, GAF) and non-spin-polarised configurations (NM). We found that the neglect of spin polarisation leads to large errors in both properties as compared to experimental data. When the experimental orthorhombic geometry is used, the AAF configuration becomes energetically the most favourable, in agreement with the experimental data. However, further optimization (Table 4.10) of the structure makes the FM state more favourable (Table 4.5) by 0.03 eV (0.1%), what is at the limit of the accuracy of the method.

The calculated *cohesive energy* of 31 eV is close to the experimental value (30.3 eV) [78]. In fact, the difference in cohesive energies between the most- (FM) and the least-favourable (GAF) magnetic configuration is only about 0.1 eV (0.3%) (Table 4.5), whereas for the non spin-polarised calculation the energy is higher by $\sim 1 \text{ eV}$. As expected, for LMO in the cubic phase, the cohesive energies of the corresponding magnetic states are higher by about 1% than those for orthorhombic phase (Table 4.10).

There are two types of distortions that distinguish the *orthorhombic* structure from the cubic perovskite LMO: the *Jahn – Teller distortion* of six O ions around Mn ions, and mutual *tilting* and *rotation* of the neighbouring MnO_6 octahedra (Figure 4.4). In many cases, when the effects under study are associated with energies greater than a few tenth of eV , fine

magnetic effects and the distortion of the structure could be neglected. Particularly, in such cases the specific magnetic ordering is not as important as the account of spin polarization itself. Although it is possible to perform calculations based on the cubic structure, as it was done for the bare surface, it is better to retain tilting and rotation of the MnO_6 octahedra, since this distortion facilitates a more efficient space filling. For example, a point defect on the surface of the slab built up of the cubic unit cells can cause a complete reconstruction of such a slab, and as a consequence - the formation energy of the defect becomes meaningless.

Two differently oriented *bare surfaces* were considered: (001) and (110), both being polar. Since the former (LaO- or MnO_2 -terminated) surface has a formal plane charge of $\pm 1 e$, its electrostatic stability [91] is provided by a charge redistribution within the slab. In order to stabilise an alternative, much more polar (110) surface, which has alternating LaMnO and $\text{O}_2 \pm 4e$ charged planes, half of the oxygen atoms has to be removed from the O_2 -terminating plane [92].

The atomic/electronic properties of the (001) surface demonstrate a weak dependence on the magnetic ordering. A more pronounced difference in *surface energies* was observed, however, between the cubic and orthorhombic slabs. Since there is a larger stress in the cubic structure, the cubic slab has a larger *relaxation energy*. Based on layer-convergence tests, symmetric nonstoichiometric 7- and asymmetric stoichiometric 8-plane slabs were chosen for further, more detailed calculations (Table 5.2). At the MnO_2 -terminated surface of the orthorhombic slab, Mn ions of the terminating plane are displaced by 0.07 \AA out from the next oxygen plane (Table 5.4). There is also a 0.17 \AA splitting off between the oxygen atoms in this O_2 plane. Though in the cubic slab plane the decomposition is different, the Mn subplane terminates the surface also in this case. Unlike MnO_2 termination, in the case of LaO termination La ions are displaced *beneath* the oxygen surface plane (Figure 5.3b).

The electron density analysis (Table 5.8, Figure 5.4 and Figure 5.5) has shown that the *charge redistribution* on the surface and in subsurface planes is determined mostly by the specific (MnO_2 - or LaO-) termination rather than by the *stoichiometry* of the slab (7- or 8-plane). This fact allows us to use nonstoichiometric 7-plane slabs, which have a compensated dipole moment along the [001] direction perpendicular to the surface, for the modelling processes on the (001) surface without defect-induced charge compensation (e.g. introduction of vacancies).

When stabilised by surface oxygen vacancies, as described above, the (110) surface shows similar surface energies ($\sim 1 \text{ eV}$) to those for the (001) surface (Table 5.12). Our prediction of the *surface reconstruction* could be checked by means of the LEED experiments.

Molecular O₂ as well as *dissociative oxygen adsorption* and *diffusion* were modelled in detail on the MnO₂-terminated (001) surface. As most favourable adsorption sites for atomic oxygen are found: atop Mn atom and “bridge” position (Figure 6.1), with adsorption energies of 4 eV and 2.4 eV, respectively. The adsorbed O atom could migrate from one to another Mn atom along the (110) direction with a high activation energy (> 1.6 eV).

Two energetically stable *oxygen molecule* orientations atop Mn ion were found: one with a molecular bond tilted by ~60° with respect to the surface normal (Figure 6.6b), another with a molecular bond parallel to the surface. The respective adsorption energies are 1.1 eV and 0.9 eV. For both configurations a *strong chemisorption* was observed. There is another stable configuration for a horizontally oriented molecule, with an adsorption energy of 0.3 eV– atop a surface oxygen atom. We predict that the adsorbed O₂ molecule could migrate as a whole on the (001) surface with an activation energy of ≥ 0.6 eV.

Due to a strong bonding between the adsorbate and the adsorbent, *penetration* of the adsorbed oxygen into the surface of the cathode can occur predominantly upon oxygen encounter with the mobile surface oxygen vacancies. Thus, the formation and diffusion energies were calculated for the O vacancy on the surface as well as in the bulk.

The *diffusion energy* on the surface (0.67 eV) is smaller than that in the bulk (0.95 eV). The latter value is typical for ABO₃ perovskites [95] whereas the reduced energy on the surface is also in line with the trend in our calculations found for oxygen vacancies in SrTiO₃ [94]. Thus, the surface O *vacancy mobility* is much higher than that of the adsorbed O atoms, and it is vacancy migration along the cathode surface what should fast O transport to the electrolyte. The reduced formation energy at the surface should stimulate O *vacancy segregation* and *space charge effects*.

Thus, as a result of this study, we demonstrated that the standard DFT-GGA approach permits reproducing basic properties of LaMnO₃, suggesting new experiments, and shedding some new light on the problem of surface reactivity.

Of great interest are further studies on:

- LaO-terminated surfaces,
- barrier for the penetration of the adsorbed O atom into the nearby O vacancy,
- Sr-doped LMO and LaCoO₃, (La,Sr), (Mn,Co) O₃ used in real fuel cells.

The oncoming version of the *VASP* code with *hybrid exchange-correlation functionals* promises more accuracy in fine electronic property calculations.

References

1. V. Dusastre and J. A. Kilner, *Solid State Ionics* **126**, 163 (1999).
2. J. Fleig, K. D. Kreuer and J. Maier, *Ceramic Fuel Cells, in Handbook of Advanced Ceramics. Volume II: Processing and Their Applications*, edited by S. Somiya et al., pages 59–105 (Elsevier Academic Press, Amsterdam, 2003).
3. T. Horita, K. Yamaji, M. Ishikawa, N. Sakai, H. Yokokawa, T. Kawada and T. Kato, *J. Electrochem. Soc.* **145**, 3196 (1998).
4. J. Fleig, *Annu. Rev. Mater. Res.* **33**, 361 (2003).
5. F. Baumann, *Oxygen reduction kinetics on mixed conducting SOFC model cathodes*, Ph.D. thesis, Stuttgart, (2006).
6. J. Fleig, F. S. Baumann, V. Brichzin, H.-R. Kim, J. Jamnik, G. Cristiani, H.-U. Habermeier, J. Maier, *Fuel Cells*, **6**, 284-292, (2006).
7. H. Tagawa et al., Oxygen nonstoichiometry in perovskite-type oxide, undoped and Sr-doped LaMnO₃, in *Proceedings of the 5th International Solid Oxide Fuel Cells Meeting*, edited by U. Stimming, S. C. Singhal, H. Tagawa and W. Lehnert, volume **97-18**, pages 785–794, The Electrochemical Society, Inc., Pennington, NJ, (1997).
8. T. Horita, M. Ishikawa, N. Sakai, H. Yokokawa, T. Kawada and T. Kato, *Solid State Ionics* **127**, 55 (2000).
9. A. Barbucci, M. Viviani, M. Panizza, M. Delucchi and G. Cerisola, *J. Appl. Electrochem.* **35**, 399 (2005).
10. J. Mizusaki, T. Saito and H. Tagawa, *J. Electrochem. Soc.* **143**, 3065 (1996).
11. A. Hammouche, A. Caneiro, E. Siebert, A. Hammou and M. Kleitz, *J. Electrochem. Soc.* **138**, 1212 (1991).
12. H. Lauret and A. Hammou, *J. Eur. Ceram. Soc.* **16**, 447 (1996).
13. J. Divisek, L. G. J. de Haart, P. Holtappels, T. Lennartz, W. Malléner, U. Stimming and K. Wippermann, *J. Power Sources* **49**, 257 (1994).
14. E. Siebert, A. Hammouche and M. Kleitz, *Electrochim. Acta* **40**, 1741 (1995).
15. B. C. H. Steele, *Solid State Ionics* **86-88**, 1223 (1996).
16. A. Endo, M. Ihara, H. Komiyama and K. Yamada, *Solid State Ionics* **86-88**, 1191 (1996).
17. M. Kleitz and F. Petitbon, *Solid State Ionics* **92**, 65 (1996).
18. V. Brichzin, J. Fleig, H. -U. Habermeier, G. Cristiani and J. Maier, *Solid State Ionics* **152-153**, 499 (2002).
19. M. Cherry, M. S. Islam and C. Catlow, *J. Solid State Chem.* **118**, 125 (1995).

20. R. A. de Souza, M. S. Islam and E. Ivers-Tiffée, *J. Mater. Chem.* **9**, 1621 (1999).
21. N. N. Kovaleva, J. L. Gavartin, A. L. Shluger, A. V. Boris and A. M. Stoneham, *J. Exp. Theor. Phys.* **94**, 178 (2002).
22. L. Kantorovich and M. Gillan, *Surf. Sci.* **374**, 373 (1997).
23. L. N. Kantorovich, M. J. Gillan and J.A. White, *J. Chem. Soc. Faraday Trans. II* **92** 2075 (1996).
24. M. Menetrey, A. Markovich, C. Minot, G. Paccioni, *J. Phys. Chem. B* **108**, 12858 (2004).
25. M. P.de Lara-Castells, J. L. Krause, *Chem. Phys. Lett.*, **354**, 483 (2002).
26. Y. Yamaguchi, Y. Nagasawa, K. Tabata, E. Suzuki, *J. Phys. Chem. A* **106**, 411 (2002)
27. Y. Wang, D. Pillay, G. S. Hwang, *Phys. Rev. B* **70**, 193410 (2004).
28. J. Oviedo and M. J. Gillan, *Surf. Sci.* **490**, 221 (2001).
29. K. Reuter and M. Scheffler, *Phys. Rev. B* **65**, 35406 (2001).
30. S. Piskunov, Yu. Zhukovskii, E. A. Kotomin, E. Heifets, D. Ellis, *Mat. Res. Symp. Proc. Vol. 894*, p.LL08-05 (2006).
31. S. Piskunov, E. Heifets, R. I. Eglitis and G. Borstel, *Comp. Mat. Sci.* **29**, 165 (2004).
32. G. Kresse, J. Furthmüller, *VASP the Guide* (University of Vienna, Austria, 2003).
33. G. Kresse, J. Hafner, *Phys. Rev. B* **48**, 13115 (1993); **49**, 14251 (1994).
34. G. Kresse, J. Furthmüller, *Comput. Mater. Sci.* **6**, 15-50, (1996); *Phys. Rev. B* **54**, 11169 (1996).
35. R. A. Evarestov, E. A. Kotomin, D. Fuks, J. Felsteiner and J. Maier, *Appl. Surf. Sci.* **238**, 457 (2004).
36. R. A. Evarestov, E. A. Kotomin, E. Heifets, J. Maier and G. Borstel, *Solid State Commun.* **127**, 367 (2003).
37. Y. M. Choi, D. S. Mebane, M. C. Lin, M. Liu, *Chem. Mater.* **19**, 1690-1699 (2007)
38. L. Wang, R. Merkle, F. S. Baumann, J. Fleig and J. Maier, *Proc. SOFC-X*, accepted, 2007.
39. R. Merkle and J. Maier, *Angew. Chem.*, accepted, 2007.
40. D. J. Singh, *Planewaves, Pseudopotentials and the LAPW Method* (Kluwer Academic: Norwell, 1994).
41. D. R. Hamann, M. Schlüter, C. Chiang, *Phys. Rev. Lett.* **43**, 1494 (1979).
- G. B. Bachelet, M. Schlüter, C. Chiang, *Phys. Rev. B* **26**, 4199 (1982).
42. D. Vanderbilt, *Phys. Rev. B* **41**, 7892-7895 (1990).

43. P. E. Blöchl, Phys Rev B **50**, 17953 (1994).
44. G. Kresse, D. Joubert, Phys. Rev. B **59**, 1758 (1999).
45. P. E. Blöchl, Phys. Rev. B **50**, 17953-17979 (1994).
46. G. Kresse, J. Joubert, Phys. Rev. B **59**, 1758 (1999).
47. V. R. Saunders, R. Dovesi, C. Roetti, R. Orlando, C. M. Zicovich-Wilson, N. M. Harrison, K. Doll, B. Civalleri, I. J. Bush, Ph. D'Arco and M. Llunell *CRYSTAL-2003 User Manual* (University of Turin, Italy, 2003).
48. R. M. Martin, *Electronic structure: Basic Theory and Practical Methods* (Cambridge University Press, 2004).
49. J. P. Perdew, A. Ruzsinszky, J. Tao, V. N. Staroverov, G. E. Scuseria, G. I. Csonka, J. Chem. Phys. **123**, 062201 (2005), R. O. Jones and O. Gunnarsson, Rev. Mod. Phys. **61**, 689 (1989).
50. W. Kohn and L. J. Sham, Phys. Rev. **140**, A1133 (1965)
51. D. M. Ceperley, B. J. Alder, Phys. Rev. Lett. **45**, 566 - 569 (1980).
52. F. Herman, J. P. Van Dyke and I. B. Ortenburger, Phys. Rev. Lett. **22**, 807 (1967).
53. P. S. Svendsen and U. von Barth, Phys. Rev. B **54**, 17402 (1996).
54. J. P. Perdew, K. Burke, Int. J. Quant. Chem. **57**, 309 (1996).
55. A. D. Becke, Phys. Rev. A **38**, 3098 (1988).
56. J. P. Perdew and Y. Wang, Phys. Rev. B **45**, 13 244 (1992).
57. J. P. Perdew, K. Burke and M. Ernzerhof, Phys. Rev. Lett. **77**, 3865 (1996).
58. V. Fock, Z. Phys. 61-126 (1930).
59. A. Svane and O. Gunnarsson, Phys. Rev. Lett. **65**, 1148 (1990).
60. W. M. Temmerman, Z. Szotek and H. Winter, Phys. Rev. B **47**, 11533 (1993).
61. A. Svane, Z. Szotek, W. M. Temmerman, J. Lægsgaard and H. Winter, J. Phys.: Condens. Matter **10**, 5309 (1998).
62. V. I. Anisimov, F. Aryasetiawan and A. I. Lichtenstein, J. Phys.: Condens. Matter **9**, 767, (1997).
63. V. I. Anisimov, J. Zaanen and O. K. Andersen Phys. Rev. B **44**, 943, (1991).
64. A. D. Becke, J. Chem. Phys. **98**, 5648, (1993).
65. S. Piskunov, E. A. Kotomin, E. Heifets, J. Maier, R. I. Eglitis and G. Borstel, Surf. Sci., **575**, 75 (2005); X. Feng, Phys. Rev B **69**, 155107 (2004).

66. F. Cora, M. Alfredsson, G. Mallia, D. Middeniss, W.C. Mackrodt, R. Dovesi and R. Orlando, *Structure and Bonding*, **113**, 171 (2004).
67. J. Rodríguez-Carvajal, M. Hennion, F. Moussa and A. H. Moudden, *Phys. Rev.*, B **57**, R3190 (1998).
68. H. J. Monkhorst, J. D. Pack, *Phys. Rev. B* **13**, 5188 (1976).
69. R. A. Evarestov, V. P. Smirnov, *Phys. Rev. B* **13**, 233101 (2004).
70. Y.-S. Su, T. A. Kaplan, S. D. Mahanti, J. F. Harrison, *Phys. Rev B* **61**, 1324 (2000).
71. M. Nicastro, C. H. Patterson, *Phys. Rev. B* **65**, 205111 (2002).
72. H. Sawada, Y. Morikawa, K. Terakura, N. Hamada, *Phys. Rev B* **56**, 12154 (1997).
73. P. Pavindra, A. Kjekshus, H. Fjellvag, A. Delin, O. Eriksson, *Phys. Rev B* **65**, 064445 (2002)
74. H. A. Jahn, E. Teller, *Proc. R. Soc. London A* **161**, 220 (1937)
75. R. Bader, *Atoms in Molecules: A Quantum Theory* (Oxford University Press, New York (1990)).
76. G. Henkelman, A. Arnaldsson and H. Jónsson, *Comput. Mater. Sci.* **36**, 254-360 (2006).
77. F. Moussa, M. Hennion, J. Rodriguez-Carvajal, H. Moudden, L. Pinsard and A. Revcolevschi, *Phys. Rev. B* **54**, 15149 (1996).
78. E. A. Kotomin, R. A. Evarestov, Yu. A. Mastrikov, J. Maier, *PCCP*, **7**, 23460-2350 (2005).
79. R. A. Evarestov, E. A. Kotomin, Yu. A. Mastrikov, D. Gryaznov, E. Heifets and J. Maier, *Phys. Rev. B* **72**, 214411 (2005).
80. N. N. Kovaleva, A. V. Boris, C. Bernhard, A. Kulakov, A. Pimenov, A. M. Balbashov, G. Khaliullin and B. Keimer, *Phys. Rev. Lett.* **93**, 147204 (2004).
81. Y. Murakami, J. P. Hill, D. Gibbs, M. Blume, *Phys. Rev. Lett.* **81**, 582 (1998).
82. T. Hotta, S. Yunoki, M. Mayr and E. Dagotto, *Phys. Rev. B*, **60**, R15009 (1999).
83. G. Banach and W. M. Temmerman, *Phys. Rev. B* **69**, 054427 (2004),
H. Zenia, G. A. Gehring, G. Banach and W. M. Temmerman, *Phys. Rev. B* **71**, 024416 (2005).
84. A. Filipetti and W. E. Pickett, *Phys. Rev. Lett.*, **83**, 4184 (1999); *Phys. Rev. B* **62**, 11571 (2000).
85. E. A. Kotomin, E. Heifets, J. Maier and W. A. Goddard III, *PCCP* **5**, 4180 (2003).
86. E. Heifets, R. A. Evarestov, E. A. Kotomin, S. Dorfman and J. Maier, *Sensors and Actuators B* **100**, 81 (2004).

87. E. A. Kotomin, E. Heifets, S. Dorfman, D. Fuks, A. Gordon and J. Maier, *Surf. Sci.* **566**, 231 (2004).
88. E. A. Kotomin, R. A. Evarestov, Yu. A. Mastrikov and J. Maier, *Phys. Chem. Chem. Phys.* **7**, 2346 (2005).
89. E. Heifets, R. I. Eglitis, E. A. Kotomin, J. Maier and G. Borstel, *Phys. Rev B* **64**, 235417 (2001).
90. P. W. Tasker, *J. Phys. C: Solid State Phys.*, **12**, 4977 (1979).
91. C. Noguera, *Physics of Oxide Surfaces* (Cambridge Univ. Press., NY, 1996).
92. E. Heifets, W. A. Goddard III, E. A. Kotomin, R. I. Eglitis, G. Borstel, *Phys. Rev. B* **69**, 035408 (2004).
93. D. R. Lide (ed.), *CRC Handbook of Chemistry and Physics* (CRC Press, Boca Raton, 1993).
94. J. Carrasco, F. Illas, N. Lopez, et al., *Phys. Rev. B* **73** (2006).
95. I. Denk, W. Munch and J. Maier, *Journal of the American Ceramic Society* **78**, 3265 (1995).

Acknowledgements

I am most grateful to my supervisor Prof. Dr. Joachim Maier for an exceptional opportunity to carry out this work in his department at Max Planck Institute for Solid State Research and introducing me into an exciting field of fuel cell research.

I wish to express my gratitude to the official referees of the dissertation Prof. Dr. Hermann Stoll and Prof. Dr. Emil Roduner for their consent to take this role.

I am greatly indebted to my adviser Prof. Dr. Eugene Kotomin who patiently guided me through my PhD for his invaluable contribution to this project. I would like to thank Rotraut Merkle for helping to gain a deeper understanding of the topic under study. Special thanks to Uwe Traub and Armin Schuhmacher for perfectly organized computational environment and responsive support in all computer related issues. I would like to thank Olga Delmer and Katja Weichert for their help with Zusammenfassung preparation within a record-short time. I am grateful to Vitaly Alexandrov for many stimulating discussions as well as for being a good friend of mine. I also would like to acknowledge my friends Dr. Sergei Piskunov (Riga), Dr. Javier Carrasco (Barcelona) and Linas Vilčiauskas for helping me to find a way through or around in many challenging aspects of computational chemistry. I express my sincere thanks to Prof. Francesc Illas and the members of his group for sharing their deep knowledge in the field of magnetic properties during my stay in Barcelona. I appreciate very much powerful tools for data analysis created by Prof. Lev Kantorovich (London) and Prof. Graeme Henkelman (Austin) and the members of his group. I also would like to thank Prof. Robert Evarestov (St. Petersburg), Dr. Eugene Heifets (Pasadena), Prof. Yuri Zhukovskii (Riga), Dr. Denis Gryaznov (Riga) for their help at various stages of this work.

Many thanks to all of the members of our Department for the pleasant and productive atmosphere I have enjoyed.

My heartfelt thanks to Sofia Weiglein for her kind and careful assistance in all administrative issues and a little bit beyond.

Finally, I would like to thank all of the people who made my stay in Stuttgart so pleasant and productive.

Thank you.

Curriculum Vitae

Family name: Mastrikov
First name: Yuri
E-mail: j.mastrikovs@fkf.mpg.de
Date of Birth: 07 July 1975
Place of Birth: Medvezhyegorsk, Russia

Education

09/2003-04/2008 PhD student at the Max Planck Institute for Solid State Research
in the Department of Prof. Dr. J. Maier
Thesis: First-principles calculations of LaMnO₃ surface reactivity

09/1999 – 05/2001 Master of Science in Electrical Engineering.
Transports and Telecommunication Institute, Riga, Latvia
Thesis: Computer simulation of electric charge collection processes in multielectrode
detectors, based on the wide bandgap semiconductors.

09/1995 – 06/1999 Bachelor of Science in Electrical Engineering.
Riga Aviation University, Riga, Latvia

09/1990 – 06/1993 Lomonosov Polytechnic College, Riga, Latvia

Honors and Awards

2004 “Large scale modeling of point defects in advanced perovskites”-
one of the five best “High Performance Computing-Europa” projects of the year.

Work Experience

2005 – 2000 Research Assistant, Institute for Solid State Physics,
University of Latvia

1998 – 2000 Research Assistant, Baltic Scientific Instruments Ltd.

Computer Skills

Master Certified Novell Engineersm

List of publications relevant to this study

Kotomin E.A., Evarestov R.A., Mastrikov Yu.A., Maier J.
DFT plane wave calculations of the atomic and electronic structure of LaMnO₃(001) surface,

PHYSICAL CHEMISTRY CHEMICAL PHYSICS 7 (11): 2346-2350, 2005

Evarestov R.A., Kotomin E.A., Mastrikov Yu.A., Gryaznov D., Heifets E., Maier J.
Comparative density-functional LCAO and plane-wave calculations of LaMnO₃ surfaces,

PHYSICAL REVIEW B 72 (21): Art. No. 214411, 2005

Kotomin E.A., Zhukovskii Yu.F, Mastrikov Yu.A., and Maier J.

First-Principles Modeling of Oxide Surfaces and Their Reactivity,

LATVIAN JOURNAL of PHYSICS and TECHNICAL SCIENCES 2, 127-140, 2006

Kotomin E.A., Mastrikov Yu.A., Heifets E., Maier J.

Adsorption of Atomic and Molecular Oxygen on the LaMnO₃(001) Surface: *ab initio* Supercell Calculations and Thermodynamics,

PHYSICAL CHEMISTRY CHEMICAL PHYSICS : DOI: 10.1039/b804378g, 2008

Carrasco J., Illas F., Lopez N., Kotomin E.A., Zhukovskii Yu.F., Evarestov R.A., Mastrikov Yu.A., Piskunov S., Maier J.

First-principles calculations of the atomic and electronic structure of F centers in the bulk and on the (001) surface of SrTiO₃,

PHYSICAL REVIEW B 73 (6): Art. No. 064106, 2006

